Doctoral Dissertation

Development of Chitin and Chitosan Monoliths with Hierarchically Porous Morphology for Flow-Based Applications

階層的多孔構造を有する キチン・キトサンモノリスの開発と通液を基盤とした応用

EMIL HAJILI

July 2024

Graduate School of Engineering

Osaka university

Table of Contents

General Introduction ..... **- 1 -**

Monolith ..... - 1 -

Chitin and chitosan ..... - 3 -

Thermally-induced phase separation ..... - 5 -

Outline of this dissertation ..... - 7 -

References ..... - 10 -

Chapter 1 ..... **- 14 -**

Development of Chitin Monoliths with Controllable Morphology by Thermally Induced Phase Separation

1.1 Introduction ..... - 14 -

1.2 Experimental section ..... - 15 -

1.3 Results and discussion ..... - 18 -

1.4 Conclusions ..... - 25 -

References ..... - 26 -

Chapter 2 ..... **- 28 -**

Development of Hierarchically Porous Chitosan Monoliths

2.1 Introduction ..... - 28 -

2.2 Experimental section ..... - 29 -

2.3 Results and discussion ..... - 32 -

2.4 Conclusions ..... - 47 -

References ..... - 48 -

Chapter 3 ..... **- 50 -**

Enzyme Immobilization Utilizing Hierarchically Porous Chitosan Monolith

3.1 Introduction ..... - 50 -

3.2 Experimental section ..... - 52 -

3.3 Results and discussion ..... - 57 -
3.4 Conclusions ..... - 70 -
References ..... - 71 -

Concluding remarks ..... - 74 -

List of publications ..... - 76 -

Acknowledgement ..... - 77 -

General Introduction

Monolith

The monoliths, whose name is derived from ancient Greek as a single piece, are continuous porous materials with three-dimensional structures of interconnected pores. As a result of their small skeletons and large through-pores that can simultaneously reduce diffusion path length and flow resistance, they have been shown to be excellent alternatives to particle-packed columns for separation, ion-exchange, catalysis, and chromatography.[1,2] Recently, the hierarchically porous polymer monoliths have attracted a great deal of attention because they have not only the advantages of hierarchical structure but also excellent properties that belong to polymer monoliths, such as superior biocompatibility, high chemical stability, and facile modifiability.[3] Based on the definition provided by the International Union of Pure and Applied Chemistry (IUPAC), porous materials can be classified into three categories: microporous (<2 nm), mesoporous (2–50 nm), and macroporous (>50 nm) (Figure 1). Hierarchically porous materials exhibit multiple length scales of porosity and structure of macropores in combination with micropores or mesopores. Their unique structure allows molecular flow, such as that occurring in biomolecules, to be facilitated by the macroporous structure, whereas the mesoporous structure, having a larger surface area, leads to greater mass transportation.[4,5] This makes them highly efficient functional materials for a wide range of applications, including highly efficient separation,[6] ion exchange,[7] catalysis,[8] photocatalysis,[9] adsorption,[10] energy conversion and storage,[11] as well as biomedicine.[12]

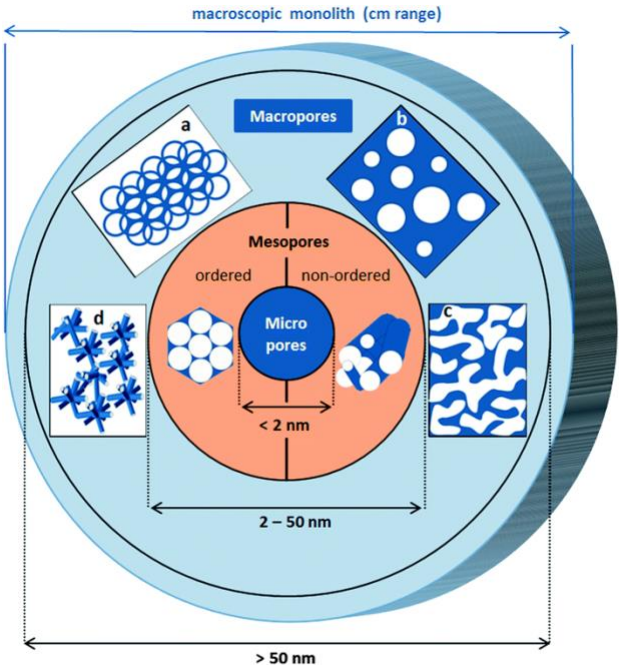

Figure 1. Concept of hierarchy in a porous material: schematics of a hierarchical porous build-up from the micrometer scale (inner blue circle), *via* the mesoscopic regime (orange circle) to the macroscopic porous dimension (light blue circle) within a monolithic material.[5]

Over the past two decades, various types of monolithic materials have been developed and categorized into inorganic monoliths, organic monoliths, and hybrid monoliths.[13,14] Inorganic monoliths, such as silica monoliths, are cheap and show minimal swelling in solvent compared to organic polymer monoliths. However, they have limitations in alkaline conditions due to dissolution and a complex preparation process. The preparation of inorganic monoliths typically involves a sol-gel method, which can be a multi-step process. This complexity increases the fabrication time and may require specialized equipment and expertise.[15] On the other hand, organic polymer monoliths provide processability and structural design flexibility, allowing precise control over the porous structure. They can be fabricated from selective monomers through polymerization in a closed mold, allowing adjustment of the porous structure by controlling polymerization conditions (Figure 2). However, polymer monoliths may suffer from swelling issues in certain organic solvents. Additionally, many reported polymer catalytic systems with metal nanoparticles are non-biodegradable and difficult to recycle, inconsistent with energy-saving and environmental protection requirements.[16] In recent years, organic porous monoliths derived from biomass have emerged as a promising alternative in the field of monolithic materials. These materials offer significant advantages including sustainability, tailorable porous structure, processability, and functionalization potential over both inorganic and organic monoliths. The porous structure of these biomass-derived organic monoliths can be precisely controlled and tuned, much like organic polymer monoliths. Furthermore, these organic porous monoliths can be fabricated using relatively simple and scalable processes, in contrast to the complex multi-step preparation of inorganic monoliths.[17–19] Overall, the unique attributes of these biomass-derived organic porous monoliths position them as an attractive choice for a diverse range of applications. From catalysis and separation technologies to energy storage systems and beyond, these materials offer significant advantages over their inorganic and traditional organic counterparts.[18,20,21]

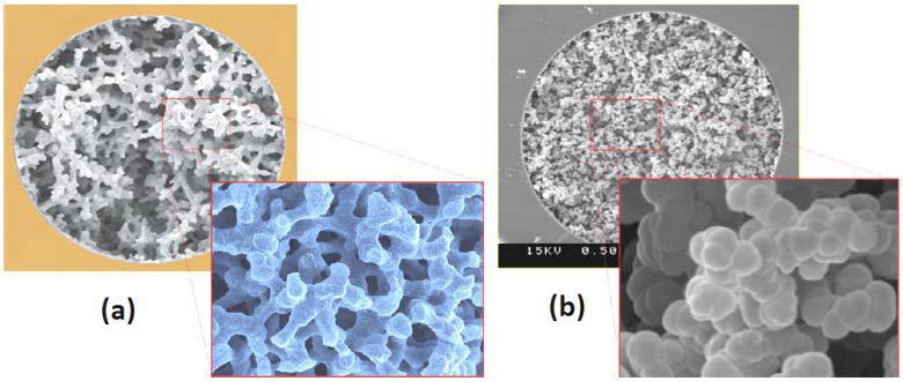

Figure 2. The difference in morphology of (a) silica-based monoliths and (b) organic polymer monoliths.[14]

Chitin and chitosan

Chitin (CT), a linear amino polysaccharide composed of β-1,4-linked *N*-acetyl-D-glucosamine monomers, is the second most abundant biodegradable natural polymer after cellulose. CT was discovered in 1811 by Henri Braconnot.[22] It is now known that CT can be found in the exoskeletons of animals, such as crustaceans (snails, crabs, shrimp, etc.), mollusks, and arthropods, as well as the cuticles of insects, scales of fish, and internal structures of invertebrates and also can be isolated from sponges naturally for pre-design 3D scaffold.[23–25]

Chitosan (CS) is a derivative of CT and is fabricated through deacetylation process.[26] CS attracted the attention of many researchers due to its properties, such as biodegradability, biocompatibility, and non-toxicity.[23,27] CT and CS are distinguished by the degree of deacetylation (DDA%), the percentage of the amino group in the structure of the polysaccharides. DDA% is one of the critical parameters, and it affects both chemical (solubility, tensile strength, etc.) and biological (adsorption, antioxidant, etc.) properties of the polymer in many processes.[28–31] The presence of the amino groups in CS provides distinctive biological functions and allows the polymer to undergo modification reactions easily. Furthermore, CS has an excellent capability for the adsorption of chemical substances, primarily metal ions, due to the amino group in its chemical structure (Figure 3).[28,32–34]

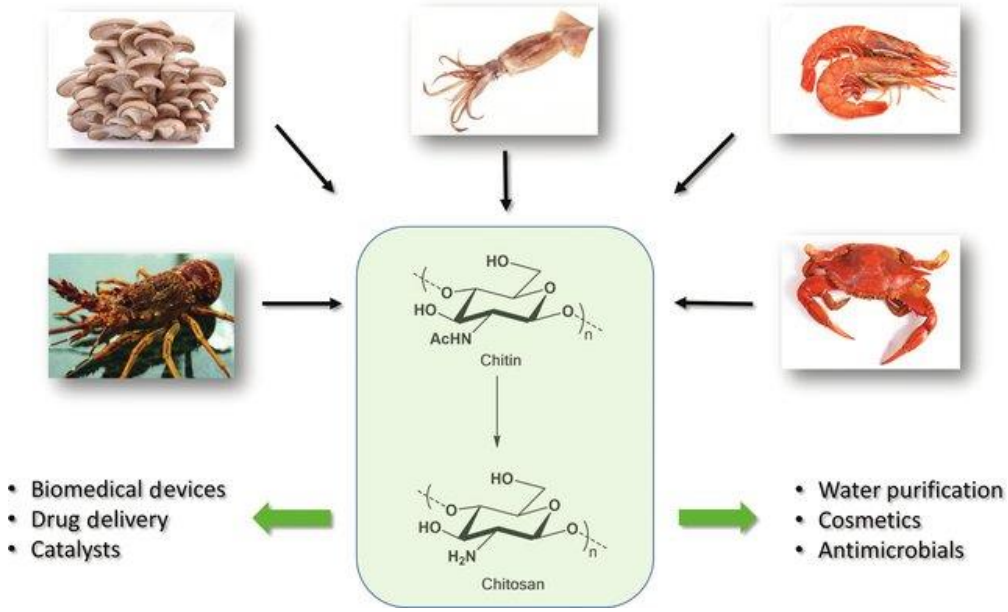

Figure 3. CT and CS sources and reported uses.[34]

Until now, various types of CS-based materials have been explored and reported, including sponges,[35] gels,[36] films,[37] nanoparticles,[38] and nanofibers[39] (Figure 4). However, the materials reported thus far have generally exhibited relatively low surface areas, which can limit their effectiveness in adsorption-based applications. Furthermore, most of the previous studies on porous CS materials have relied on the use of other materials as templates, whereby the CS was integrated or coated onto the surface of these templates.[40] This approach has resulted in the formation of hybrid frameworks rather than pure CS structures. The use of hybrid frameworks can potentially limit the performance and range of applications of the materials, as the presence of the other components may influence the inherent properties and functionalities of the CS. Additionally, the removal of the template molecules from the CS structures in the later stages of material fabrication can be challenging and complex.

To overcome the limitations of previous studies, the development of pure CS monolithic materials with hierarchically porous structures would be a significant advancement in the field. Hierarchically porous structures can provide enhanced surface area, improved mass transport, and enhanced structural integrity. These characteristics are crucial for various applications, such as filtration, adsorption, catalysis, and tissue engineering. By successfully creating pure CS monolithic materials with hierarchically porous structures, researchers could unlock new possibilities and significantly improve the overall performance of these biomass-derived materials. Such materials could exhibit enhanced mechanical properties, increased surface area, and improved mass transport capabilities, making them suitable for a wide range of applications, including but not limited to filtration, adsorption, catalysis, and tissue engineering.

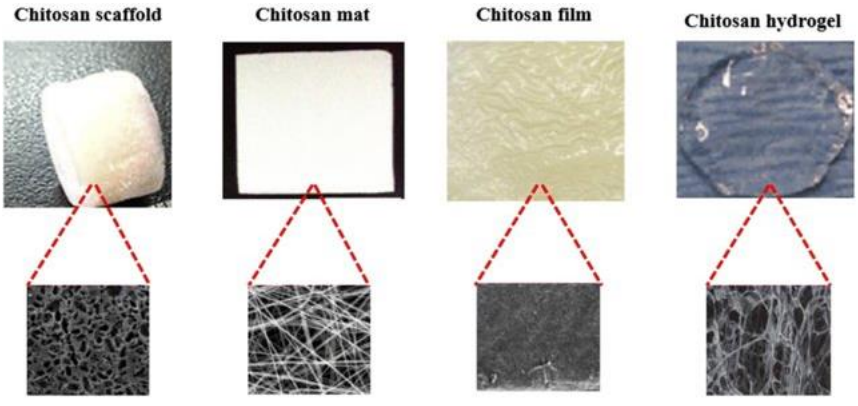

Figure 4. CS materials with various forms.[40]

Thermally-induced phase separation

Porous materials have been widely utilized in various applications, ranging from filtration and adsorption to catalysis and tissue engineering. However, the development of advanced biopolymer-based materials often requires innovative fabrication techniques that can impart desirable properties, such as high surface area, hierarchical porosity, and mechanical robustness. In this regard, the thermally-induced phase separation (TIPS) technique has emerged as a relatively simple and efficient method for the green synthesis of polymeric monoliths.[41] TIPS is a process in which a polymer is dissolved in a solvent at an elevated temperature, and the resulting homogeneous solution is then cast into a desired shape and cooled to induce phase separation. This method has several advantages over traditional polymer fabrication techniques. Firstly, TIPS allows the production of membranes from semi-crystalline polymers, typically not soluble in solvents at ambient temperatures. Secondly, the TIPS process is a binary system, inherently simpler than other techniques, with fewer variables to control. Finally, TIPS has the potential to be a green route for obtaining monolithic polymers in a relatively short timeframe, making it an attractive option for various applications.[42] Unlike other polymer fabrication methods, such as

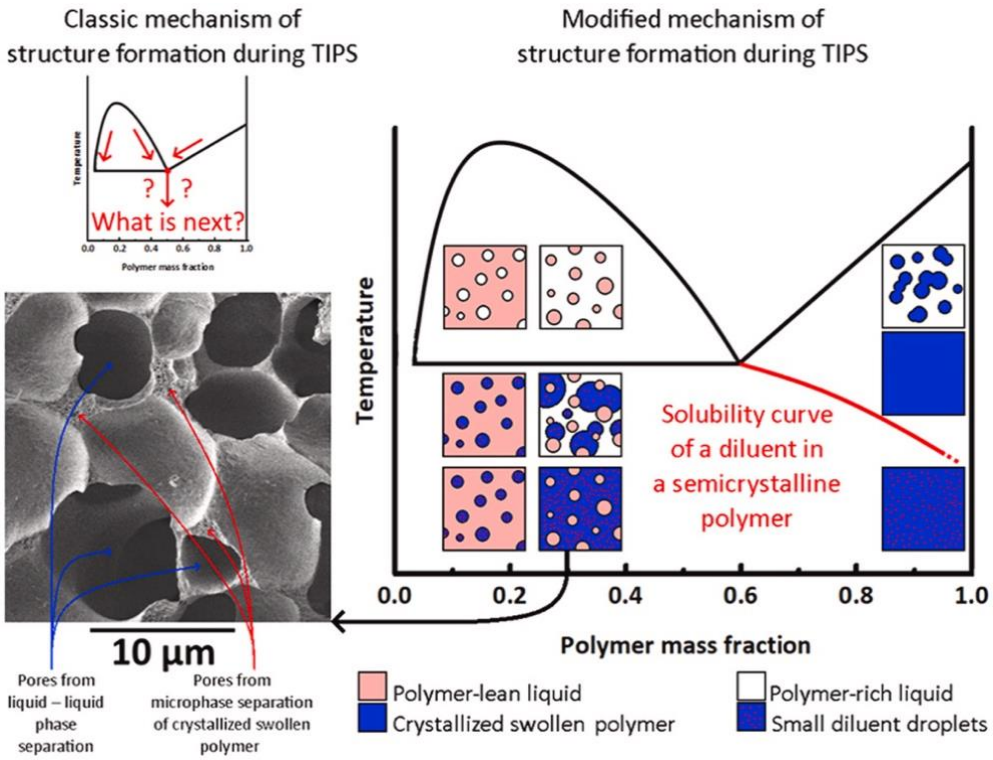

Figure 5. Thermally-induced phase separation in semicrystalline polymer solutions.[48]

crosslinking,[43] free radical polymerization,[44–47] and thin-layer membrane fabrication,[47] TIPS is a relatively straightforward process that can be easily scaled up. These alternative techniques often involve complicated steps and are primarily suitable for small-scale production. In contrast, the TIPS method has been reported to produce mechanically robust polymer membranes with highly porous skin layers, making it a versatile and desirable approach (Figure 5).[41,48]

Despite the advantages of TIPS, its direct application to CT and CS has been challenging. Acetyl, amino, and hydroxy groups in CT and CS lead to inter- and intramolecular hydrogen bonds, resulting in a highly aggregated and crystalline structure (Figure 6).[49,50] This, in turn, leads to poor solubility in most common organic solvents, limiting the direct use of TIPS for these biopolymers. There are solvents in which CT is soluble, such as concentrated acids (HCl, H_2SO_4, and H_3PO_4)[51] and amide/LiCl systems (*N*,*N*-dimethylacetamide/LiCl and *N*-methyl-2-pyrrolidone/LiCl).[52] For CS, it can be dissolved in an acidic environment.[53] However, these solvents cause inherent problems such as chain degradation due to hydrolysis, difficult removal of residual solvents, and toxicity. To overcome the solubility issues of CT and CS, researchers have explored various strategies, including chemical modifications,[54,55] the use of ionic liquids,[56] and the identification of new solvents.[57] Chemical modification of the hydroxy groups has been one of the effective methods to improve the solubility of CT and CS, enabling the application of TIPS to these biopolymers and their derivatives. Using soluble derivatives of CT and CS makes it possible to employ the TIPS technique to fabricate porous polymer monoliths with desirable properties.

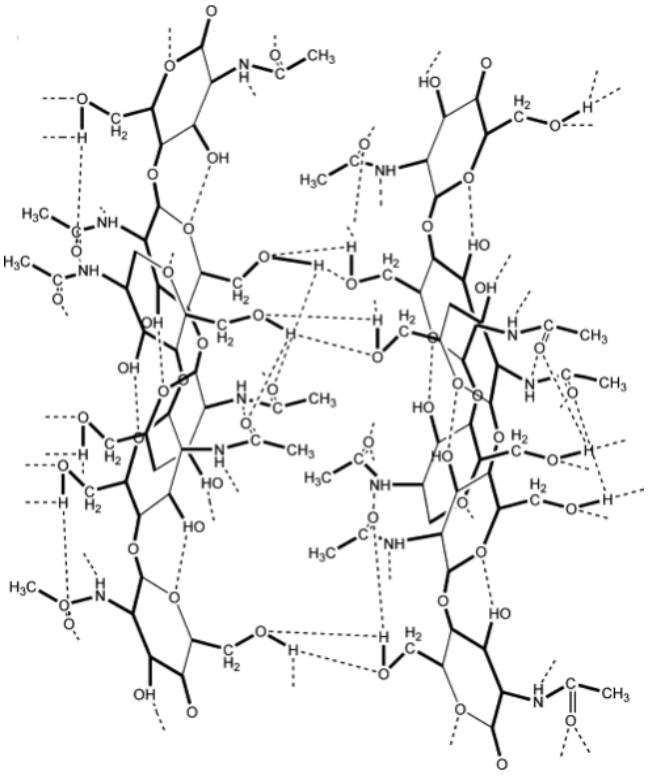

Figure 6. Molecular structure and hydrogen bonding in CT.[50]

Outline of this dissertation

This thesis focuses on the fabrication and characterization of CT and CS based monoliths with tailored porous structures for various flow-based applications. Through the employment of TIPS technique, the author aimed to develop CT and CS monoliths with controllable morphology and enhanced performance in flow-based systems. The thesis is divided into three main chapters, each addressing a specific aspect of this research endeavor.

Chapter 1 - Development of Chitin Monoliths with Controllable Morphology by Thermally Induced Phase Separation

In this chapter, the author presents the successful preparation of CT monoliths with continuous porous structures suitable for flow-based applications. By leveraging the TIPS method, the morphology of the porous structures could be tailored by adjusting the phase separation conditions. The water flow applicability of the resulting CT monoliths was also assessed, highlighting their potential for use in various flow-based systems. The presence of amide bonds and hydroxy groups in the CT monoliths broadens their direct applications and provides opportunities for further modifications.

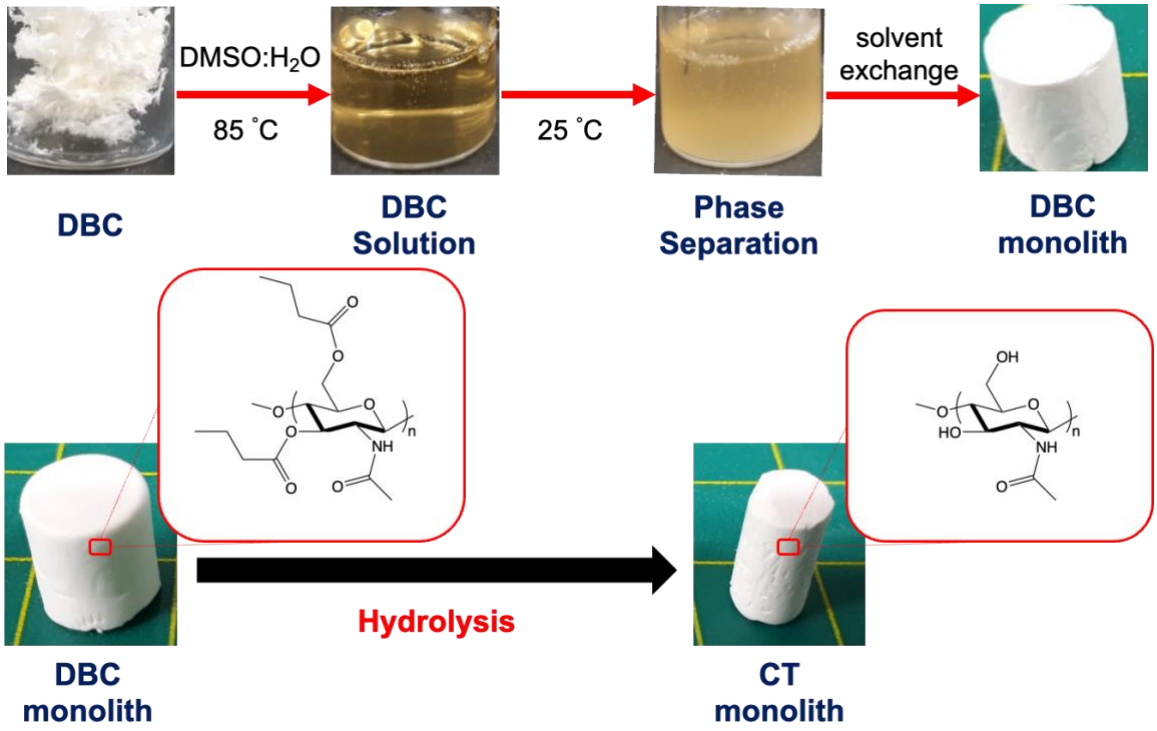

Scheme 1. Fabrication of DBC and CT monoliths.

Chapter 2 - Development of Hierarchically Porous Chitosan Monoliths

Building upon the insights gained from the previous chapter, this chapter introduces a practical template-free approach for the fabrication of CS monoliths with hierarchically porous structures. The author employed a high-concentration alkali treatment at elevated temperatures to deacetylate the CT monoliths, effectively converting them into CS monoliths. The resulting hierarchically porous CS monoliths were then evaluated for their ability to capture Cu(II) ions in a flow-based system, demonstrating their potential for environmental remediation and water purification applications.

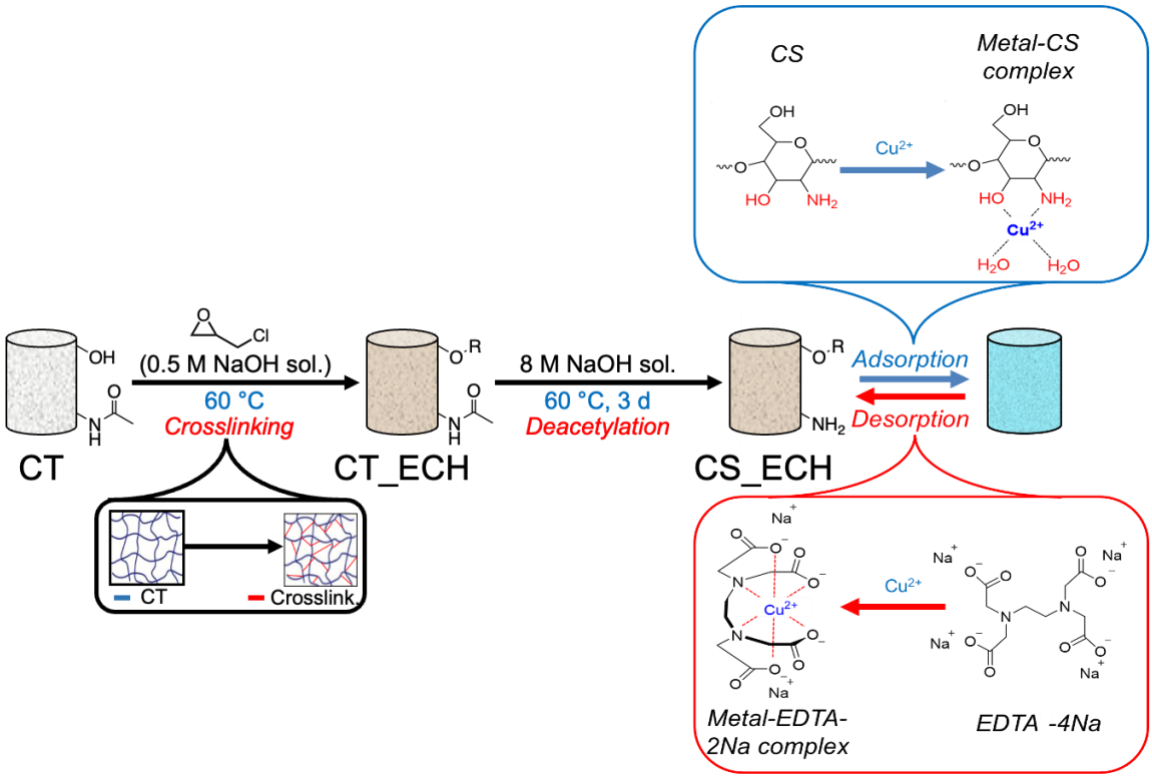

Scheme 2. Fabrication and application of CS monolith.

Chapter 3 - Enzyme Immobilization Utilizing Hierarchically Porous Chitosan Monolith

In the final chapter, the author introduces a novel and practical method for the immobilization of α-amylase on the hierarchically porous CS monoliths developed in the previous chapter. The immobilization technique combines physical adsorption and covalent bonding to enhance the stability of α-amylase at different pH levels and temperatures, compared to its soluble form. The presence of amino and hydroxy groups in CS allows for effective physical binding with the enzyme,

while the epoxy group in the monolith provides additional stability via covalent bonding between the stationary phase and the enzyme.

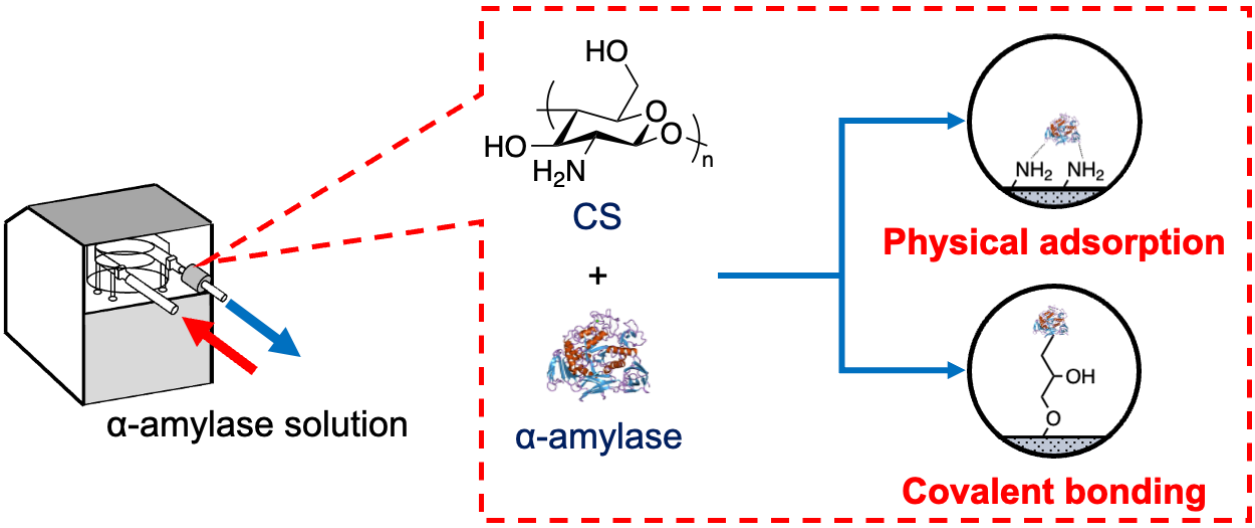

Scheme 3. Immobilization of α-amylase immobilization on CS monolith.

References

[1] F. Maya, B. Paull, *J. Sep. Sci.* **2019**, *42*, 1564.

[2] I. Nischang, T. J. Causon, *Trends Anal. Chem.* **2016**, *75*, 108.

[3] F. Lorignon, A. Gossard, M. Carboni, *Chem. Eng. J.* **2020**, *393*, 124765.

[4] L. Wu, Y. Li, Z. Fu, B. L. Su, *Natl. Sci. Rev.* **2020**, *7*, 1667.

[5] A. Feinle, M. S. Elsaesser, N. Hüsing, *Chem. Soc. Rev.* **2016**, *45*, 3377.

[6] H. Saini, E. Otyepková, O. Otyepková, A. Schneemann, R. Z. Zbořil, M. Otyepka, R. A. Fischer, K. Jayaramulu, *J. Mater. Chem. A* **2022**, *10*, 12.

[7] W. Liu, J. Wang, J. Wang, X. Guo, H. Yang, *J. Alloys Compd.* **2021**, *874*, 159921.

[8] S. Gao, X. Jia, J. Yang, X. Wei, *J. Mater. Chem.* **2012**, *22*, 21733.

[9] H. Zhou, X. Li, T. Fan, F. E. Osterloh, J. Ding, E. M. Sabio, D. Zhang, Q. Guo, *Adv. Mater.* **2010**, *22*, 951.

[10] I. Berezovska, R. A. Sanguramath, M. S. Silverstein, *J. Polym. Sci.* **2022**, *60*, 81.

[11] W. Zhang, Y. Tian, H. He, L. Xu, W. Li, D. Zhao, *Natl. Sci. Rev.* **2020**, *7*, 1.

[12] Z. Meng, F. Wei, R. Wang, M. Xia, Z. Chen, H. Wang, M. Zhu, Z. Q. Meng, M. G. Xia, Z. G. Chen, M. F. Zhu, F. Wei, R. H. Wang, P. Wang, *Adv. Mater.* **2016**, *28*, 245.

[13] J. C. Masini, F. Svec, *Anal. Chim. Acta.* **2017**, *964*, 24.

[14] A. Sabarudin, *Adv. Eng. Res.* **2018**, *171*, 1.

[15] Z. Walsh, B. Paull, M. Macka, *Anal. Chim. Acta.* **2012**, *750*, 28.

[16] F. Svec, *J. Chromatogr. A* **2010**, *1217*, 902.

[17] C. Acquah, C. K. S. Moy, M. K. Danquah, C. M. Ongkudon, *J. Chromatogr. B* **2016**, *1015–1016*, 121.

[18] S. Dutta, A. Bhaumik, K. C-W Wu, *Energy Environ. Sci.* **2014**, *7*, 3445.

[19] M. H. Salim, Z. Kassab, E. houssaine Ablouh, H. Sehaqui, A. Aboulkas, R. Bouhfid, A. E. K. Qaiss, M. El Achaby, *Int. J. Biol. Macromol.* **2022**, *200*, 182.

[20] X. Mi, W. Wang, J. Gao, Y. Long, F. Xing, X. Wang, F. Xu, X. You, S. Li, Y. Liu, *Polym. Adv. Technol.* **2012**, *23*, 38-47.

[21] P. O. Ibeh, F. J. García-Mateos, J. M. Rosas, J. Rodríguez-Mirasol, T. Cordero, *J. Taiwan Inst. Chem. Eng.* **2019**, *97*, 480.

[22] B. K. Park, M. M. Kim, *Int. J. Mol. Sci* **2010**, *11*, 5152.

[23] M. Rinaudo, *Prog. Polym. Sci.* **2006**, *31*, 603.

[24] M. Yadav, P. Goswami, K. Paritosh, M. Kumar, N. Pareek, V. Vivekanand, *Bioresour. Bioprocess* **2019**, *6*.

[25] C. Brigode, P. Hobbi, H. Jafari, F. Verwilghen, E. Baeten, A. Shavandi, *J. Clean Prod.* **2020**, *275*, 122924.

[26] I. Younes, M. Rinaudo, D. Harding, H. Sashiwa, *Mar. Drugs* **2015**, *13*, 1133.

[27] S. Shankar, J. P. Reddy, J. W. Rhim, H. Y. Kim, *Carbohydr. Polym.* **2015**, *117*, 468.

[28] Z. Hu, S. Lu, Y. Cheng, S. Kong, S. Li, C. Li, L. Yang, *Molecules* **2018**, *23*, 3147.

[29] L. Tavares, E. E. Esparza Flores, R. C. Rodrigues, P. F. Hertz, C. P. Z. Noreña, *Food Hydrocoll.* **2020**, *106*, 105876.

[30] S. Bhardwaj, N. K. Bhardwaj, Y. S. Negi, *Cellulose* **2020**, *27*, 5337.

[31] N. A. Qinna, Q. G. Karwi, N. Al-Jbour, M. A. Al-Remawi, T. M. Alhussainy, K. A. Al-So'ud, M. M. H. Al Omari, A. A. Badwan, *Mar. Drugs* **2015**, *13*, 1710.

[32] Z. A. Sutirman, M. M. Sanagi, K. J. Abd Karim, W. A. Wan Ibrahim, B. H. Jume, *Int. J. Biol. Macromol.* **2018**, *116*, 255.

[33] M. A. Abu-Saied, R. Wycisk, M. M. Abbassy, G. A. El-Naim, F. El-Demerdash, M. E. Youssef, H. Bassuony, P. N. Pintauro, *Carbohydr. Polym.* **2017**, *165*, 149.

[34] A. Jardine, S. Sayed, *Pure Appl. Chem.* **2018**, *90*, 293.

[35] K. Takada, H. Yin, T. Matsui, M. Asif Ali, T. Kaneko, *J. Polym. Res.* **2017**, *24*.

[36] S. M. Samani, F. Ahmadi, Z. Oveisi, Z. Amoozgar, *Res. Pharm. Sci.* **2015**, *10*, 1.

[37] A. Takegawa, M. Murakami, Y. Kaneko, J. Kadokawa, *Carbohydr. Polym.* **2010**, *79*, 85.

[38] F. Rossi, E. Mauri, M. O. Taha, R. M. Saeed, I. Dmour, *Front. Bioeng. Biotechnol.* **2020**, *8*.

[39] T. Yoshioka, H. Onomoto, H. Kashiwazaki, N. Inoue, Y. Koyama, K. Takakuda, J. Tanaka, *Mater. Trans.* **2009**, *50*, 1269.

[40] B. Farhadihosseinabadi, A. Zarebkohan, M. Eftekhary, M. Heiat, M. Moosazadeh Moghaddam, M. Gholipourmalekabadi, *Cell. Mol. Life Sci.* **2019**, *76*, 2697.

[41] J. F. Kim, J. H. Kim, Y. M. Lee, E. Drioli, *AIChE Journal* **2015**, *62*, 461.

[42] G. Conoscenti, V. La Carrubba, V. Brucato, *Arch. Chem. Res.* **2017**, *1*.

[43] T. Kubo, N. Kimura, K. Hosoya, K. Kaya, *J. Polym. Sci. A Polym. Chem.* **2007**, *45*, 3811.

[44] Y. Li, H. D. Tolley, M. L. Lee, *J. Chromatogr. A* **2010**, *1217*, 8181.

[45] J. Hasegawa, K. Kanamori, K. Nakanishi, T. Hanada, S. Yamago, *Macromol. Rapid Commun.* **2009**, *30*, 986.

[46] N. Tsujioka, N. Ishizuka, N. Tanaka, T. Kubo, K. Hosoya, *J. Polym. Sci. A Polym. Chem.* **2008**, *46*, 3272.

[47] H. Sai, K. W. Tan, K. Hur, E. Asenath-Smith, R. Hovden, Y. Jiang, M. Riccio, D. A. Muller, V. Elser, L. A. Estroff, S. M. Gruner, U. Wiesner, *Science* **2013**, *341*, 530.

[48] K. V. Pochivalov, A. V. Basko, T. N. Lebedeva, A. N. Ilyasova, M. Y. Yurov, R. Y. Golovanov, V. V. Artemov, V. V. Volkov, A. A. Ezhov, A. V. Volkov, Y. V. Kudryavtsev, *Mater. Today Commun.* **2021**, *28*, 102558.

[49] J. C. Roy, F. Salaün, S. Giraud, A. Ferri, In *Solubility of Polysaccharides* (Ed.: Xu, Z.), IntechOpen, Rijeka, **2017**, p. 110-127.

[50] C. K. S. Pillai, W. Paul, C. P. Sharma, *Prog. Polym. Sci.* **2009**, *34*, 641.

[51] A. Silvana Naiu, S. Berhimpon, R. Iwan Montolalu, N. J. Kawung, P. Suptijah, *Curr. Res. Nutr. Food Sci.* **2020**, *8*, 197.

[52] A. Jardine, *Curr. Res. Green Sustainable Chem.* **2022**, *5*, 100309.

[53] H. El Knidri, A. Laajeb, A. Lahsini, In *Handbook of Chitin and Chitosan*, Elsevier, **2020**, pp. 35-37.

[54] M. M. Islam, R. Islam, S. M. Mahmudul Hassan, M. R. Karim, M. M. Rahman, S. Rahman, M. Nur Hossain, D. Islam, M. Aftab Ali Shaikh, P. E. Georghiou, *Carbohydr. Polym. Technol. Appl.* **2023**, *5*, 100283.

[55] S. Bi, D. Qin, S. Yuan, X. Cheng, X. Chen, *Green Chem.* **2021**, *23*, 9318-9333.

[56] M. Sharma, C. Mukesh, D. Mondal, K. Prasad, *RSC Adv.* **2013**, *3*, 18149.

[57] X. Wang, P. Zhou, X. Lv, Y. Liang, *Mater. Today Commun.* **2021**, *27*, 102374.

Chapter 1

Development of Chitin Monoliths with Controllable Morphology by Thermally Induced Phase Separation

1.1 Introduction

The growing demand for sustainable and eco-friendly materials has driven the scientific community to explore the vast potential of biopolymers as alternatives to traditional organic polymers, with the ability to form advanced functional materials.[1–3] Recently, there have been some researches about fabrication monolith from biopolymers to improve functionality and applicability of material in various fields while focusing on their sustainability and environmental friendliness. For instance, previously, biopolymer-based porous materials have been developed from cellulose, alginate, and polyvinyl alcohol and used for water treatment.[4–6] CT is one of the attractive biopolymer and has distinctive advantage over other biopolymers due to its chemical versatility. The structure of CT is similar to that of cellulose, with the only distinction being the replacement of the hydroxy group at the C2 position of cellulose by an acetamide group in CT. Unlike cellulose, CT contains amino groups from partly present D-glucosamine units that are introduced through deacetylation, allowing for further modification and functionalization. This opens up possibilities for tailored chemical reactions including alkylation, acylation, quaternization, phosphorylation, sulfonation, thiolation etc. These modifications can significantly enhance the material's properties, such as solubility, hydrophobicity, and biocompatibility, making chitin a highly attractive choice for diverse applications.[7–9] Additionally, the presence of amino groups in CT enables it to provide unique biological functions such as antimicrobial, antifungal, and immunostimulatory properties, making it suitable for biomedical applications.[10–12] However, the inherent insolubility of CT poses a challenge in terms of its processability, necessitating the exploration of chemical modification routes to overcome this limitation. One such approach is the development of dibutyrylchitin (DBC), an ester derivative of CT bonding butyryl groups at C3 and C6 positions, which can disrupt of the rigid crystalline structure having intra- and intermolecular hydrogen bonds.[13–16] The advantage of using DBC lies in its ability to maintain the inherent properties of CT, such as biocompatibility and biodegradability, while overcoming the challenges

associated with the insolubility and enhancing processability. Importantly, DBC can be easily converted back to the original CT form, making it a versatile intermediate.[17]

Previous studies have explored the fabrication of cellulose monoliths using the TIPS method.[18,19] For instance, cellulose acetate, a soluble derivative of cellulose, has been successfully transformed into cellulose monoliths through the TIPS process. Inspired by these findings, the focus of this study was shifted towards DBC. By employing the TIPS method, a continuous porous structure was achieved in the form of a DBC monolith, which could subsequently be converted into CT by hydrolysis. The morphology of the resulting CT monoliths could be controlled by adjusting the phase separation conditions. Moreover, the water flow applicability of the CT monoliths could be assessed, making them suitable for flow-based applications. The integration of CT's unique properties, such as its hierarchical porous structure and functional groups, with the flow-based characteristics opens up new routes for its utilization in various fields. In light of the above considerations, this study aims to investigate the fabrication and characterization of CT monoliths with controllable porous structures. Additionally, it aims to evaluate the suitability of these monoliths for flow-based applications and explore their potential for modification and functionalization. By achieving these objectives, this research contributes to expanding the practical applications of CT and furthering the development of environmentally friendly materials.

1.2 Experimental section

1.2.1 Materials

CT was purchased from Sigma-Aldrich, and 70% perchloric acid and butyric anhydride were obtained from FUJIFILM Wako Pure Chemical Corporation. Other reagents were of analytical grade and used without further purification.

1.2.2 Synthesis of DBC

CT (5.0 g) was added to a freshly prepared solution (95.0 mL) of butyric anhydride (2.2 mL) in 70% perchloric acid. The mixture was stirred in a water bath for 3 h at a temperature of approximately 20 °C. The mixture was then subjected to precipitation. The supernatant was removed and the precipitant was poured into deionized water, the pH value of which was adjusted to 7 by adding $NaHCO_3$. The solid raw product, the precipitate, was dried and dissolved in acetone (200 mL) for 2 h. After filtration, the acetone solution of the polymer was separated from any

insoluble material and poured into deionized water (1000 mL).[20] During precipitation, white flocculent pure DBC was formed. After collecting, drying, and weighing, the yield was calculated to be 41.3%. The number average molecular weight (M_n) and the weight average molecular weight (M_w) of DBC were 104,000 and 370,000 g mol^{-1}, respectively.

1.2.3 Fabricating the DBC monolith

The calculated amount of DBC was dissolved completely in dimethyl sulfoxide (DMSO) at 85 °C for 2 h, and deionized water was added (Table 1-1). The resulting mixture was stirred at 85 °C for 3h, followed by controlled cooling at 25 °C overnight. The fabricated monolith was subjected to solvent exchange three times with water at 1 h intervals. For drying, DBC monoliths were put inside vacuum desiccator and pump was used to suck air inside of the desiccator and create the vacuum environment at 25 °C. After vacuum drying, DBC monolith was obtained (Figure 1-1(a)).

Table 1-1. Preparation condition of the DBC monoliths.

Sample name	DBC concentration (g L^{-1})	DMSO/H_2O (v/v)
S1	60	88/12
S2	80	88/12
S3	100	88/12
S4	80	83/17
S5	80	93/7

1.2.4 Hydrolysis of the DBC monolith for CT monolith preparation

The DBC monolith was immersed in 1 mol L^{-1} NaOH aqueous solution under gentle shaking for 5 h and subjected to solution exchange thrice with water, thrice with ethanol, and finally twice with hexane. A CT monolith was obtained after vacuum drying.

1.2.5 Characterization

Fourier transform infrared (FT-IR) measurements of the samples were performed using the Thermo Scientific (U.S.) Nicolet iS5 spectrometer equipped with an iD5 ATR attachment. A Hitachi (Tokyo, Japan) S-3000N scanning electron microscope (SEM), operated at 15 kV, was used to observe the structure of the monolith cross sections. Before the measurements, the

monolith samples were cut into thin sections and pasted onto the stab and put into vacuum chamber of the ion sputter apparatus (E-1010 Hitachi Ltd, Tokyo, Japan) and set the time for 180 s. The monolith samples were sputtered with Au-Pd at 1.0 Torr. The electric current was 15 mA during coating. Macropore diameter of the SEM images were determined by ImageJ software. Before analyzing, the pixel-distance ratio is set based on the known scale bar. Later, the image was binarized to black for pore and background and white as the structure of the polymer. For estimation of the particle size and circularity, the analyzed particle function was used. The average macropore diameter calculated assuming that the pore is circular. For each sample analyses, population was maintained at least 50. The number average molecular weight (M_n) and the weight average molecular weight (M_w) of the DBC were determined using size exclusion chromatography (SEC) (HLC-8020 GPC SYSTEM, TOSOH) on a TSK gel column of 7.8 mm × 300 mm (ID × L) with the flow rate of 1 ml min^{-1} at 40 °C equipped with a refractive index and UV detector. 0.1 mol L^{-1} DMF solution with LiCl was used as a solvent. Low polydispersity polystyrene standard samples were used for calibration. The structure of DBC was characterized by proton nuclear magnetic resonance (^{1}H NMR) spectroscopy using acetone-D6 as a solvent, with JNM-ECS400 (400 MHz, JEOL Ltd., Tokyo, Japan). The scanning time was set to 32 times. The crystalline structure of DBC and CT monolith were characterized by using an X-Pert diffractometer with graphitemonochromatized Cu-Kα radiation (λ = 1.54 Å) at 45 kV and 200 mA. The XRD patterns were recorded over the 2θ range of 4° to 35° at a speed 1° min^{-1}. Nitrogen adsorption/desorption isotherms were recorded using a NOVA 4200e 152 surface area and pore size analyzer (Quantachrome Instruments) at 77 K. Prior to the measurements, the sample was freeze-dried for 1 d and then degassed at 70 °C under vacuum for 6 h. The specific surface area was calculated using the Brunauer–Emmett–Teller (BET) equation. Thermal stability was conducted by thermogravimetric analysis performed with STA 7000 Thermogravimetric Analyzer (Hitachi, Japan) by applying the heating rate of 10 °C in an inert nitrogen atmosphere (from 50 to 600 °C). The mechanical performance of the monolith was evaluated on a universal testing machine (EZ Graph, SHIMADZU) with a compression speed of 1 mm min^{-1} in water at room temperature using a 500 N load cell.

A Fusion 200 two-channel syringe pump (Chemyx Inc.) was used to control the influx and velocity of the influent. Additionally, the permeability of the CT monoliths was calculated using Darcy's law:[21]

$$B_0 = \frac{L \times \mu \times V}{\Delta P} \tag{1-1}$$

where B_0 is permeability coefficient, Darcy (1 Darcy = 1×10^{-8} cm^2), L is length of the monolith (cm), μ is the viscosity of the water (Pa s), V is the velocity of the flow (cm s^{-1}) and ΔP is the pressure drop when influent is flowing through the monoliths (Pa).

1.3 Results and discussion

1.3.1 Fabrication of DBC monolith

The ^{1}H NMR analysis was carried out to evaluate the molecular structure of the DBC. In Figure 1-2, the characteristic proton signals of CT backbone from δ 3.6 to δ 5.4, N-H proton at δ 7.1, and acetamido methyl protons at δ 1.9 were observed. The following signals demonstrated the successful introduction of butyryl group onto CT: the peaks at δ 2.35 and δ 2.51 for -OCOCH$_2$, δ 1.69 and δ 1.80 for –CH$_2$, and δ 1.0 and δ 1.1 for –CH$_3$. The signal δ 3.0 and δ 2.2 shows H$_2$O and acetone which comes from deuterium acetone, respectively. The degree of butyrylation is

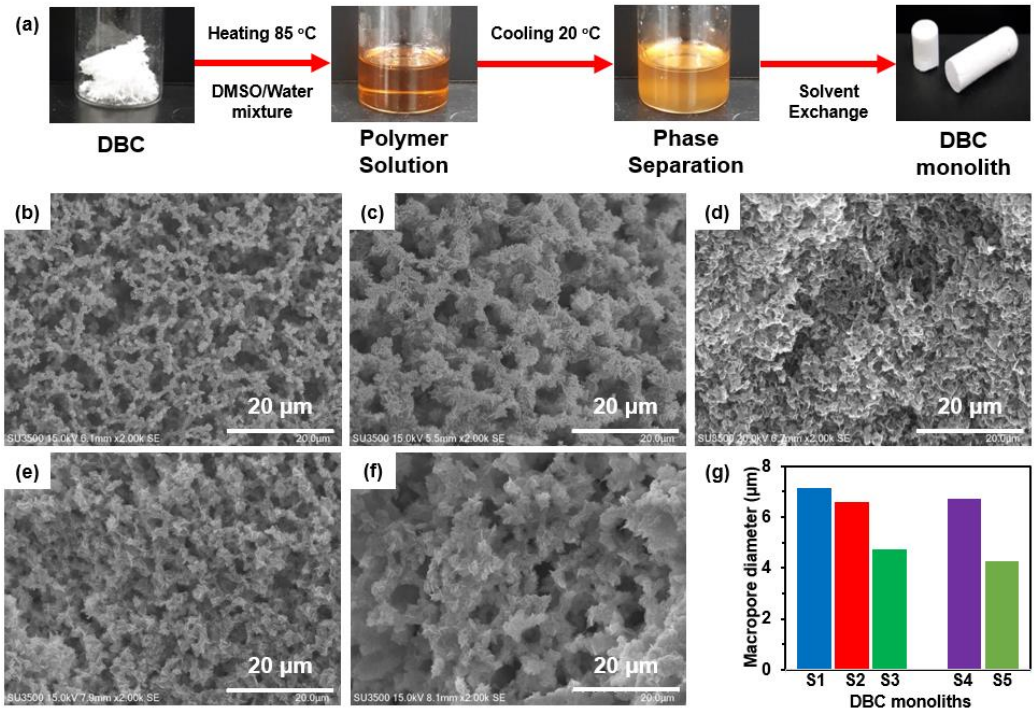

Figure 1-1. (a) Fabrication of DBC monoliths using the TIPS method. (b–d) SEM images of the S1, S2, and S3 DBC monoliths fabricated using different DBC concentrations. (e–f) S4 and S5 DBC monoliths fabricated using different DMSO/H$_2$O ratios. (g) Macropore diameters.

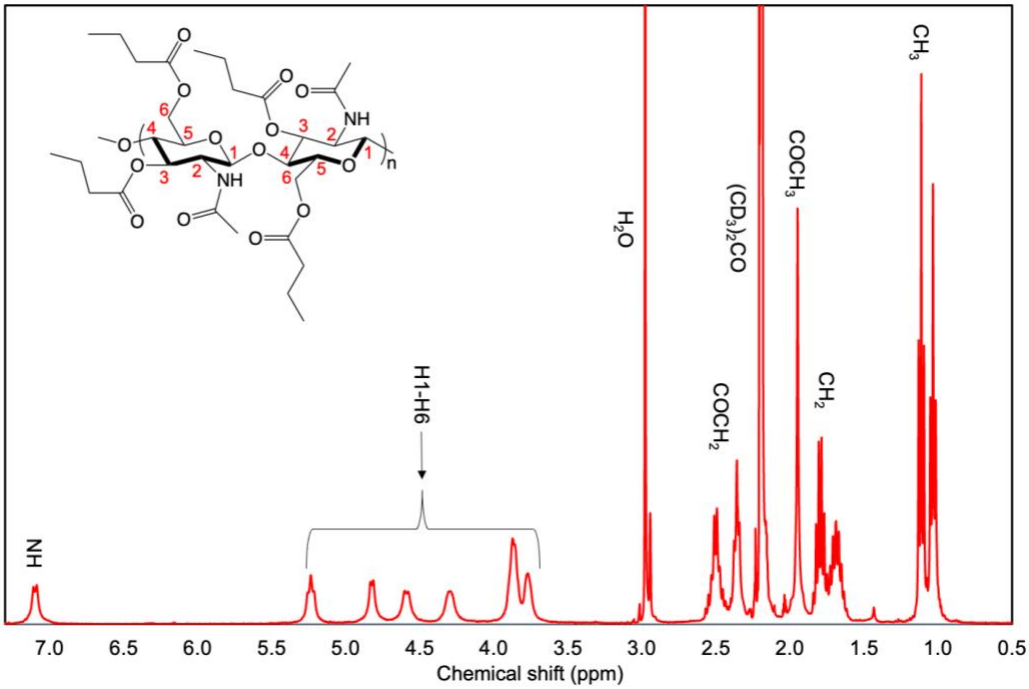

Figure 1-2. ^{1}H NMR spectrum of DBC.

calculated as 1.8 from the integral ratio of the -$OCOCH_2$ and -$COCH_3$. DBC is soluble in most organic solvents like methanol, ethanol, acetone, dimethylformamide (DMF), *N*,*N*-dimethylacetamide, and DMSO; however, CT is insoluble in conventional organic solvents, which restricts its direct fabrication through TIPS method. The selection of the proper solvent is one of the essential factors in fabricating polymer monoliths by TIPS. Regarding with TIPS, methanol, ethanol, and acetone has low boiling temperatures, which restricts the phase separation condition upon heating. On the other hand, DMF, which was used to fabricate cellulose acetate monolith before, completely dissolved DBC at room temperature fast. This could lead to the result that part of DBC could be again dissolved in DMF after phase separation. Thus, DMSO was selected as a good solvent while water was selected as a poor solvent, which is the crucial factor in forming the porous morphology of the DBC monolith and systematically examining the fabrication parameters to tune the porous structure of the monolith.

For the DBC monolith, the effect of the DBC concentration was evaluated. Various DBC monoliths with different pore diameters were prepared when the polymer concentration was changed. As shown in Figure 1-1(b–d), with increased DBC concentration, the macropore diameter of the DBC monolith decreased from 7.1 ± 0.2 μm to 4.7 ± 0.2 μm, but the obtained DBC monoliths maintained a porous structure.

Not only the polymer concentration but also the composition of good and poor solvents affects phase separation, and then the structure of the monolith can be controlled. As the DMSO/H_2O ratio increased, the pore diameter of the resulting monolith became larger with a thicker skeleton. Therefore, it was demonstrated that a DBC monolith with co-continuous macropores could be prepared via the TIPS method using DMSO and water as the solvents, and the pore size of the DBC monolith can be controlled by modulating the polymer concentration and solvent composition.

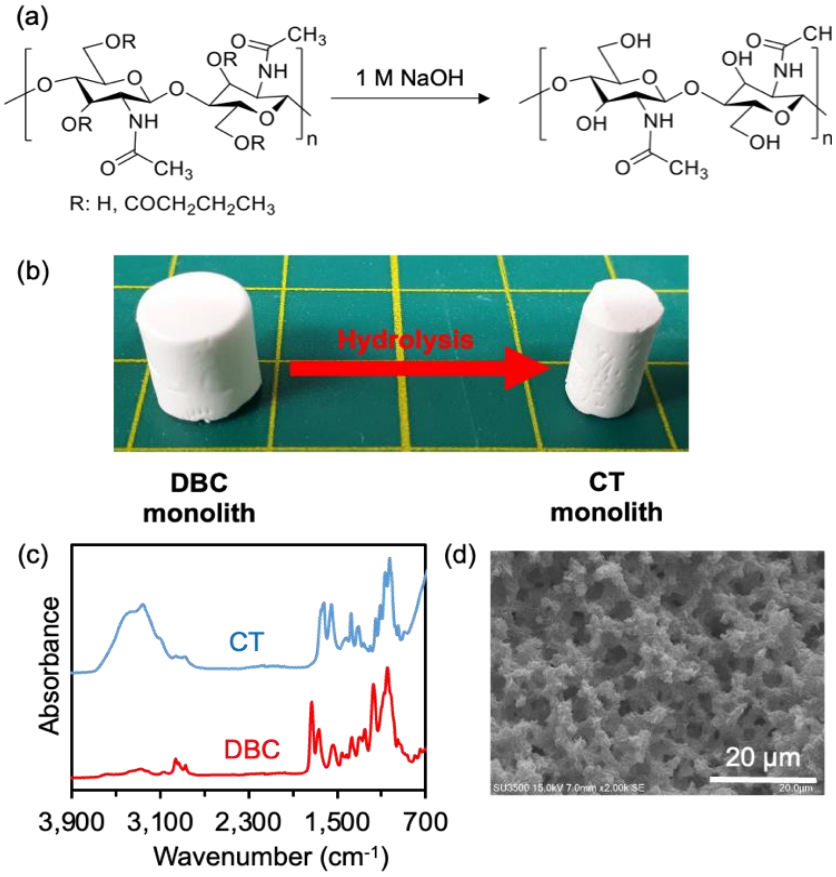

Figure 1-3. (a) Scheme of the hydrolysis reaction of DBC to produce CT monolith and (b) macroscopic images of monoliths. (c) FT-IR spectra of the DBC and CT monoliths. (d) SEM image of CT monolith.

1.3.2 Fabrication of CT monolith

The CT monolith was produced by hydrolyzing the butyl ester of the DBC monolith. The DBC monolith formed using 80 g L^{-1} DBC, and an 88:12 DMSO/H_2O ratio was selected for the CT monolith fabrication process because of its porous structure. The reaction scheme and photo of monoliths were shown in Figure 1-3(a,b). For the concentration of NaOH, 1 mol L^{-1} was determined enough for conversion to CT. The FT-IR spectrum of DBC and CT monolith was examined in Figure 1-3(c). The FT-IR spectra of the CT monolith confirmed the successful hydrolysis of butyryl ester by the disappearance of the peak at 1740 cm^{-1}, which is related to the

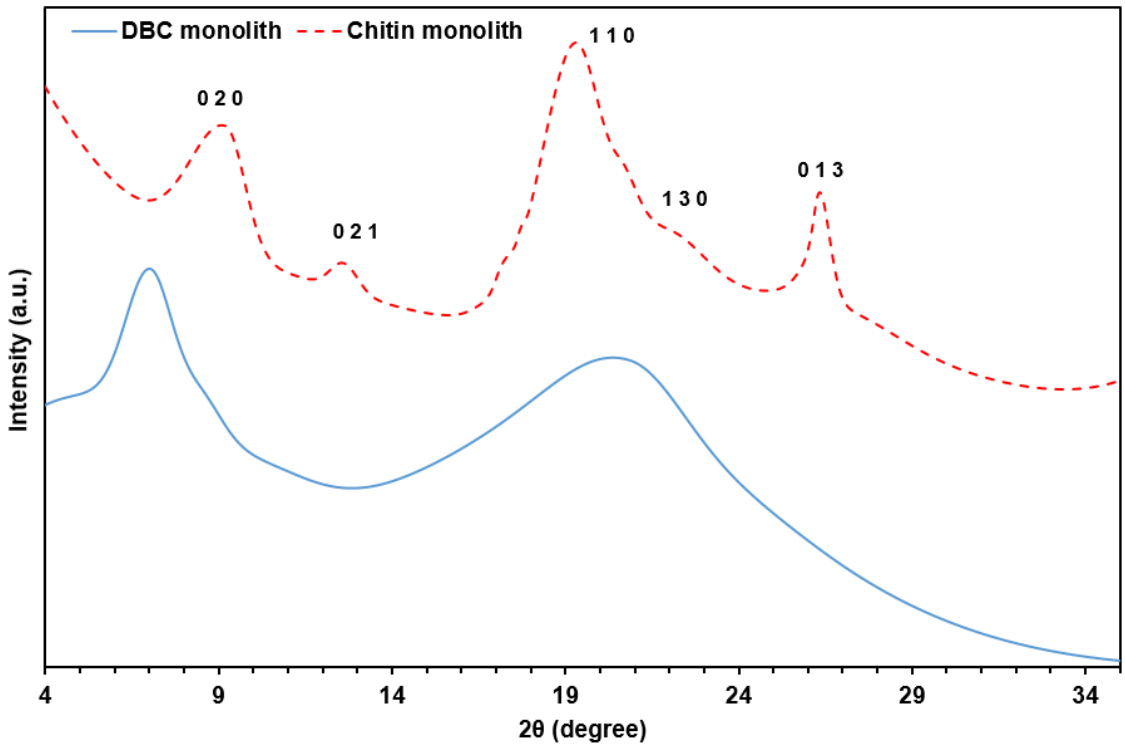

Figure 1-4. XRD patterns of DBC and CT monoliths.

ester moiety of DBC. In addition, the hydroxy groups indicated by a broad band between 3100 and 3600 cm^{-1} were not observed in the DBC monolith. This suggests that 1 mol L^{-1} NaOH is sufficient to convert the DBC monolith into a CT monolith. During the hydrolysis of DBC monolith, although the average diameter of the pore size decreased from 6.6 ± 0.2 μm to 4.2 ± 0.2 μm, the CT monolith maintained its porous structure (Figure 1-3(b,d)).

The XRD profile of the DBC and CT monolith has been shown in Figure 1-4. In the DBC monolith, two distinctive peaks were observed at 7.16° and 20.88°, respectively. On the CT monolith profile, 0 2 0 and 1 1 0 diffraction peaks shift to 9.14° and 19.38°, respectively. Moreover, additional peaks were formed at 12.64° 0 2 1, 22.34° 1 3 0 and 26.40° 0 1 3.[22] There are crystalline peaks at 9.14° and 19.38° due to rigid intra hydrogen bonds, which means that after hydrolysis of the DBC monolith to CT monolith, intra hydrogen bonds reformed.

1.3.3 N_2 adsorption/desorption isotherm

To evaluate the mesoporous features of the DBC and CT monoliths, nitrogen adsorption/desorption analysis was performed. The isotherm and pore size distribution plots are shown in Figure 1-5. As shown in Figure 1-5(a), all curves can be classified as Type IV with

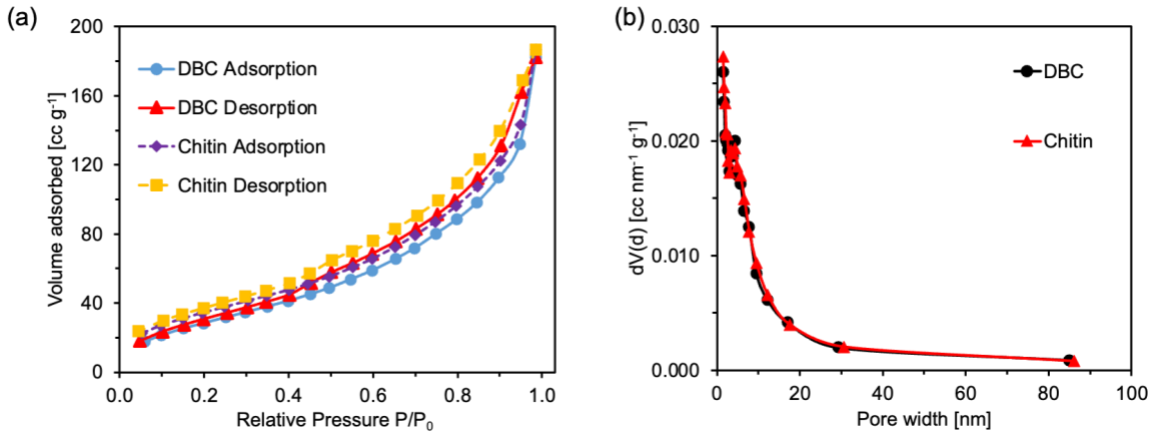

Figure 1-5. (a) Nitrogen adsorption/desorption isotherms and (b) corresponding pore size distribution curves of the DBC and CT monoliths.

adsorption hysteresis loops in terms of IUPAC classification, indicating the presence of mesopores. The average pore sizes of the DBC and CT monoliths were 3.5 and 3.4 nm, respectively (Figure 1-5(b)). This confirms that the monolith maintained its structure during the hydrolysis process. In addition, the surface areas were determined to be 89 $m^2 g^{-1}$ for the DBC monolith and 101 $m^2 g^{-1}$ for the CT monolith. Thus, both monoliths were mesoporous and could be utilized under water flow for catalysis, metal capture from wastewater, dye sorption, and drug delivery systems.

1.3.4 Thermal and mechanical properties

The TGA studies of DBC and CT monolith was shown in Figure 1-6(a). For both DBC and CT monoliths, two main steps of decomposition were observed. The small weight change was firstly observed in the temperature range from 50 to 120 °C, which is attributed to water

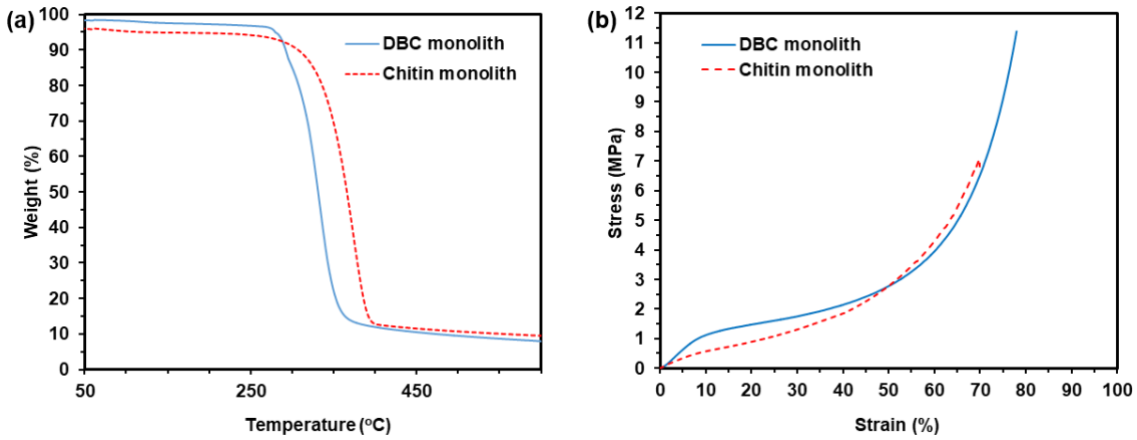

Figure 1-6. (a) TGA profiles and (b) compression stress-strain curves of DBC and CT monoliths.

evaporation. The second occurs in the range of 350-400 °C for CT and 310-360 °C for DBC monolith and could be attributed to the degradation of the polymer structure of the molecule. The TGA profiles of the two monoliths indicate that CT monolith has higher thermal stability than DBC monolith. The temperature difference of 40 °C between two monoliths indicates effects on the intermolecular forces and hydrogen bonding.

For the practical application of the monolith as a flow reactor or filter, good mechanical properties, especially the shape resilience of monolith, are necessary since the damage of monolith in the use process may cause a decrease in monolith performance. Compression deformation tests were performed to evaluate the mechanical strength (Figure 1-6(b)). The DBC monolith showed a maximum strain beyond 75% without breaking. According to the calculations, the compressive modulus is 125.9 ± 0.3 kPa for DBC monolith. On the other hand, the CT monolith exhibits a compression modulus of 67.7 kPa, but it is fractured at a strain of 69.8% with fractured stress of 7.0 ± 0.3 MPa. Both monoliths have shown ductile behavior due to their flexible 3D CT network.

1.3.5 Permeability

For application as a column, liquid permeability for the solvent is required. Additionally, the absolute permeability was calculated in order to determine the intensive properties of the monolith in the flow system. The permeability coefficient in the flow system, B_0, was measured at flow rates of 0.1, 0.2, 0.3, 0.4, and 0.5 mL min^{-1}. The density of DBC and CT monolith used in the flow experiment were 0.25 and 0.22 g cm^{-3}, respectively. As shown in Figure 1-7(a), there was a linear increase in the pressure drop as the flow rate or pump injection time increased. Comparing

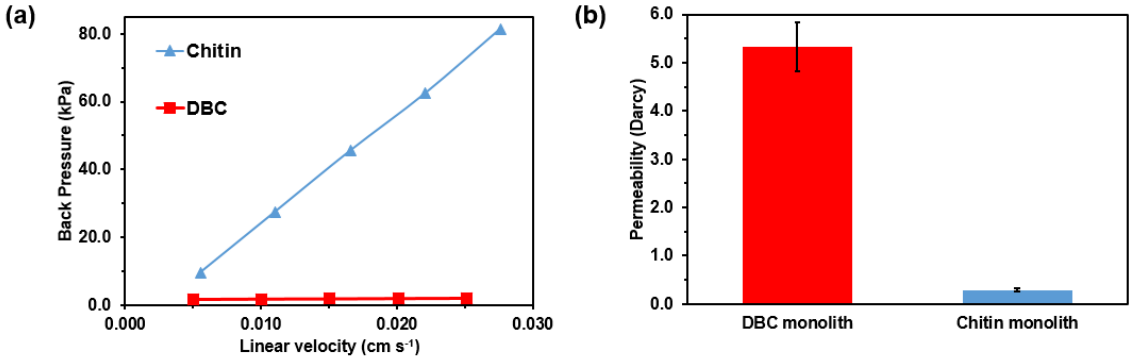

Figure 1-7. (a) The calculated back pressure of DBC and CT monoliths at different linear velocities. (b) Average permeability measurements of DBC and CT monoliths at flow rates of 0.1, 0.2, 0.3, 0.4, and 0.5 mL min^{-1}.

monoliths, DBC had a significantly lower pressure loss than CT. At 0.5 mL min^{-1}, the backpressure of the CT monolith was calculated as 81.4 kPa, while the DBC monolith exhibited a 2.0 kPa pressure loss. A possible reason for this could be the pore diameter differences between monoliths. Since the average pore size diameter of the DBC is larger than CT, it experiences less back pressure than the CT monolith. At the end of the test, the permeability of the DBC and CT monoliths was calculated using the Darcy equation to be 5.34 ± 0.51 and 0.29 ± 0.02 darcys, respectively **(**Figure 1-7(b). Although the CT monolith has lower permeability than the DBC monolith owing to its smaller pore diameters, this value is still sufficiently high to indicate that the CT monolith has the potential to be utilized as a filter or microreactor under flow conditions. For instance, the permeability coefficient for the silica column, which is one of the most used materials for flow application, is between 0.01 and 1.01 darcy.[23,24] For other reactors like carbon reactor, porous gel reactor, and cellulose monolith reactor, it is about 0.01~0.10 darcy.[25]

1.3.6 Adsorption process

After confirming a good permeability of the CT monolith, a preliminary test was set up to analyze the adsorption behavior of the CT monolith. Before the adsorption test, the CT monolith is immersed into the 8 mol g^{-1} NaOH solution and kept at 60 °C for 24 h to deacetylate. Methyl orange was selected as an anionic dye to test whether monoliths will adsorb or not. Then, an adsorption circulation was carried out with a peristaltic pump by conducting 50 mg L^{-1} methyl orange solution to pass through the monolith for 24 h. In Figure 1-8(a), both CT and deacetylated CT monolith are shown after adsorption. As seen from Figure 1-8(a), both monoliths change their color after adsorption, which means they have the potential to remove anionic dyes from the flow. Unlike CT monolith, which has a yellowish color, deacetylated CT monolith becomes completely orange after adsorption results in higher adsorption capacity than CT monolith. Furthermore, Figure 1-8(b)

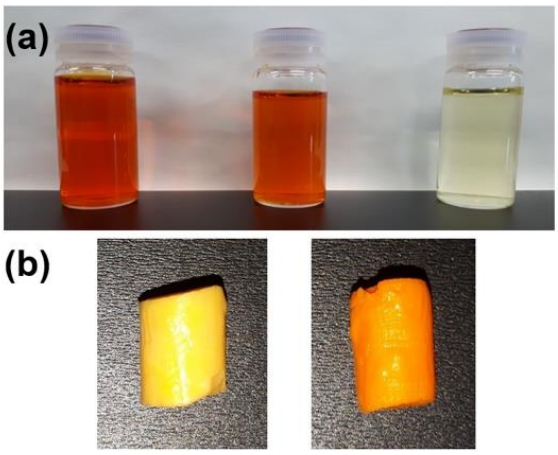

Figure 1-8. (a) Methyl orange solution before adsorption (left) and after adsorption with CT (middle) and deacetylated CT (right) monoliths. (b) CT (left) and deacetylated CT (right) monoliths after adsorption.

shows methyl orange solution before and after adsorption. From Figure 1-8(b), it can be assumed that deacetylated CT monolith almost removed the anionic dye from the solution, which indicates it can remove dyes from the water.

1.4 Conclusions

A hierarchically porous CT monolith was successfully produced by the TIPS method. FT-IR analysis confirmed the successful conversion of a DBC monolith to a CT monolith. The pore morphology of the monolith could be controlled by varying the DBC concentration and DMSO/H_2O ratio. Increasing the DBC concentration decreased the pore size while decreasing the DMSO/H_2O ratio increased the pore diameter. Both DBC and CT monoliths exhibit excellent mechanical properties and thermal stability, and water flow tests confirmed that they had sufficient permeability to be used as a filter or a microreactor under flow conditions. For future, CT monolith can be deacetylated to CS monolith to be used in metal chelating, dye sorption, or protein separation process.

References

[1] A. George, M. R. Sanjay, R. Srisuk, J. Parameswaranpillai, S. Siengchin, *Int. J. Biol. Macromol.* **2020**, *154*, 329.

[2] J. Wang, M. Euring, K. Ostendorf, K. Zhang, *J. Bioresour. Bioprod.* **2022**, *7*, 1.

[3] R. A. Ilyas, S. M. Sapuan, *Curr. Anal. Chem.* **2020**, *16*, 500.

[4] H. G. Park, M. Y. Chae, *J. Appl. Chem. Biotechnol.* **2004**, *79*, 1080.

[5] Z. Karim, A. P. Mathew, V. Kokol, J. Wei, M. Grahn, *RSC Adv.* **2016**, *6*, 20644.

[6] M. S. Thomas, P. K. S. Pillai, M. Faria, N. Cordeiro, L. Kailas, N. Kalarikkal, S. Thomas, L. A. Pothen, *J. Appl. Polym. Sci.* **2020**, *137*, 48993.

[7] M. Z. Elsabee, R. E. Morsi, M. Fathy, In *Encyclopedia of Marine Biotechnology*, **2020**, pp. 885–963.

[8] M. Pakizeh, A. Moradi, T. Ghassemi, *Eur. Polym. J.* **2021**, *159*, 110709.

[9] W. Wang, C. Xue, X. Mao, *Int. J. Biol. Macromol.* **2020**, *164*, 4532.

[10] U. Dave, E. Somanader, P. Baharlouei, L. Pham, M. A. Rahman, *J. Mar. Sci. Eng.* **2021**, *9*, 1173.

[11] S. I. Ahmad, R. Ahmad, M. S. Khan, R. Kant, S. Shahid, L. Gautam, G. M. Hasan, M. I. Hassan, *Int. J. Biol. Macromol.* **2020**, *164*, 526.

[12] M. E. Abd El-Hack, M. T. El-Saadony, M. E. Shafi, N. M. Zabermawi, M. Arif, G. E. Batiha, A. F. Khafaga, Y. M. Abd El-Hakim, A. A. Al-Sagheer, *Int. J. Biol. Macromol.* **2020**, *164*, 2726.

[13] H. Sashiwa, N. Kawasaki, A. Nakayama, E. Muraki, N. Yamamoto, S. I. Aiba, *Biomacromolecules* **2002**, *3*, 1136.

[14] K. Kurita, K. Sugita, N. Kodaira, M. Hirakawa, J. Yang, *Biomacromolecules* **2005**, *6*, 1414.

[15] H. El Knidri, R. Belaabed, A. Addaou, A. Laajeb, A. Lahsini, *Int. J. Biol. Macromol.* **2018**, *120*, 1181.

[16] T. Zhong, M. P. Wolcott, H. Liu, J. Wang, *J. Clean. Prod.* **2020**, *250*, 119458.

[17] T. Jain, S. Kumar, P. K. Dutta, *Int. J. Biol. Macromol.* **2016**, *82*, 1011.

[18] Y. Xin, Q. Xiong, Q. Bai, M. Miyamoto, C. Li, Y. Shen, H. Uyama, *Carbohydr. Polym.* **2017**, *157*, 429.

[19] Z. T. Xie, T. A. Asoh, Y. Uetake, H. Sakurai, H. Uyama, *Carbohydr. Polym.* **2020**, *247*, 116723.

[20] L. Szosland, G. C. East, *J. Appl. Polym. Sci.* **1995**, *58*, 2459.

[21] G. W. Jackson, D. F. James, *Can. J. Chem. Eng.* **1986**, *64*, 364.

[22] O. P. Gbenebor, S. O. Adeosun, G. I. Lawal, S. Jun, S. A. Olaleye, *Eng. Sci. Technol. Int. J.* **2017**, *20*, 1155.

[23] Q. Li, C. Lü, H. Li, Y. Liu, H. Wang, X. Wang, Z. Liu, *J. Chromatogr. A* **2012**, *1256*, 114.

[24] Y. Lyu, T. A. Asoh, H. Uyama, *Polym. Degrad. Stab.* **2020**, *177*, 109164.

[25] Z. Yang, T.-A. Asoh, H. Uyama, *Chem. Commun.* **2020**, *56*, 411.

Chapter 2

Development of Hierarchically Porous Chitosan Monoliths

2.1 Introduction

Water pollution resulting from heavy metal ions has become a pressing environmental concern, given their detrimental effects on ecosystems and human health.[1,2] Addressing this issue necessitates the development of effective and sustainable materials for heavy metal ion removal. CS, a biopolymer derived from CT, has emerged as a promising candidate in this field due to its unique properties and advantages over other natural polymers such as CT and cellulose. CS possesses several advantageous characteristics that make it highly suitable for heavy metal ion adsorption. Its amino groups provide active sites for metal ion binding, and its high surface area facilitates efficient adsorption.[3,4] Furthermore, CS exhibits excellent biocompatibility, biodegradability, and low toxicity, making it an environmentally friendly option for water treatment applications.[5,6] Conventional approaches for heavy metal removal using CS often involve dissolving CS flakes or particles in acidic solutions, followed by an ultrafiltration process to capture the metal ions. However, this typical method faces significant limitations. CS is generally intended for single-use applications, as the recycling and reuse of the material requires complex, multi-step processes. Furthermore, the treatment of industrial effluents using CS can lead to issues with clogging and blockages due to the agglomeration of the CS particles.[7] To address these problems, preconditioning techniques, such as de-agglomeration procedures, are frequently applied. While these pretreatment steps help control the hydrodynamic properties, they often result in increased complexity and a substantial loss of sorption efficiency.[8]

Previous studies have explored the versatility of CS by investigating its adsorption capabilities and interaction mechanisms with metal ions in various forms, including sponges, gels, films, nanoparticles, and nanofibers.[9] However, the current industry landscape has faced limitations in fully leveraging the advantages of CS. One of the primary challenges is the difficulty in producing high-performance monolithic materials composed solely of CS, as opposed to CS-hybrid frameworks. In the past, researchers have attempted to fabricate porous CS materials by using other materials as templates and integrating CS onto their surfaces.[10–12] While these efforts have led to the development of CS-based hybrid frameworks, the decreasing ratio of natural polymers like CS within the template materials has limited the overall performance of the resulting

materials. To address these limitations, the development of monolithic materials composed solely of pure CS, with hierarchically porous structures, holds great promise. Such materials could unlock the full potential of CS's adsorption capabilities, interaction mechanisms, and unique properties. Moreover, the integration of CS monoliths into flow-based systems could further enhance their efficiency and versatility, enabling continuous and high-throughput processing for various applications, such as water treatment, metal recovery, and environmental remediation.

This study offers a new, practical method for creating a CS monolith with hierarchically porous structures through CT monolith. The TIPS method was employed, wherein chemically modified CT was used as the precursor for monolith fabrication. In chapter 1, the fabrication of CT monolith through TIPS was discussed. Herein, high-concentrated alkali treatment at high temperature was used to deacetylate the CT monolith to the CS monolith. Unlike previous approaches, this method eliminates the need for scaffolds, allowing to production of functional monoliths. In this study, a first-time CS monolith was fabricated without any scaffolds, and the capture of Cu(II) ions by the flow system was performed. The presence of amino groups in the CS monoliths enables diverse applications. By exploring the potential of CS monoliths in heavy metal ion removal, this study contributes to the development of sustainable materials for water treatment and environmental remediation.

2.2 Experimental section

2.2.1 Materials

CT from shrimps and ethylenediaminetetraacetic acid (EDTA) were purchased from Sigma-Aldrich. Perchloric acid (70%), butyric anhydride, sodium hydroxide, epichlorohydrin (ECH), and copper(II) chloride (anhydrous) were purchased from FUJIFILM Wako Pure Chemical Corporation. Other reagents were analytical grade and used without further purification.

2.2.2 Preparation of crosslinked CT monoliths

The CT monolith was fabricated by the TIPS method reported in previous chapter. The detailed process was as follows: CT powder was added to a freshly prepared solution of the butyric anhydride in 70% perchloric acid and stirred for three hours at 20 °C. The mixture was poured into deionized water; the pH value was 7. The solid raw product was collected, dried, and dissolved in acetone with stirring. After filtration, the acetone solution of the polymer was separated from any

insoluble material and poured into deionized water for precipitation. The formed white flocculent pure dibutyrylchitin (DBC) was collected and dried. To prepare the monolith, DBC was dissolved completely in dimethyl sulfoxide (DMSO) under 85 °C and deionized water was added to the solution (80 g L^{-1} of DBC with 88/12 (vol./vol.) DMSO/H_2O solution). Subsequently, the solution was stirred at 85 °C for three hours and placed under 25 °C overnight. The CT monolith was obtained after hydrolysis of the DBC monolith by 1.0 mol L^{-1} aqueous NaOH solution.

For crosslinking of CT monolith, 0.1 mol L^{-1} NaOH solution was prepared, and a certain amount of ECH was added and stirred for 5 min. The amount of ECH was calculated based on the molecular weight of repeated monosaccharide unit of CT (MW = 204 g mol^{-1}) (Table 2-1). When ECH was completely mixed with NaOH solution, the CT monoliths were immersed and degassed. The monoliths were left in the solution at 60 °C for 3 d.

2.2.3 Deacetylation of CT monoliths to CS monoliths

For the deacetylation of monoliths, CT monoliths were immersed into concentrated NaOH solution (8.0 mol L^{-1}) and left for 3 d at 60 °C. The solvent exchange process was continued with ethanol and hexane three times at one-hour intervals for each solvent. The CS monoliths were obtained after vacuum drying. The illustration of monolith fabrication was revealed in Figure 2-1(a), and Table 2-1 shows a list of the prepared CS monoliths.

Table 2-1. Composition of the monoliths.

Sample name	CT:ECH (mol:mol)	Deacetylation to CS
CT	1:0	CS
CT_ECH_1	1:1	CS_ECH_1
CT_ECH_2	1:2	CS_ECH_2
CT_ECH_5	1:5	CS_ECH_5

2.2.3 Characterization

The microscopic structure of the monoliths was observed by a Hitachi S-3000N scanning electron microscope (SEM), operated at 15 kV. During the sample preparation, the thin section of

the monoliths was pasted onto a stab and coated with a thin layer of gold using an ion sputter apparatus (E-1010, Hitachi). The ImageJ software was used to calculate the average macropore diameter of monoliths through the SEM images. Before analyzing, the pixel-distance ratio is set based on the known scale bar. Later, the image was binarized to black for pore and background and white as the structure of the polymer. The analyzed particle function was used to estimate the particle size and circularity. The average macropore diameter is calculated assuming that the pore is circular. The molecular structure of CS monoliths was analyzed by proton nuclear magnetic resonance (^{1}H NMR) spectroscopy using 1% deuterium chloride/deuterium oxide mixture as a solvent with JNM-ECS400 (400 MHz, JEOL). X-ray diffractometer with graphitemonochromatized Cu-Kα radiation (λ = 1.54 Å) (SmartLab, RIGAKU) was used to analyze the crystalline structure of monoliths in the range of 4° to 35° at a speed of 1° min^{-1}. The porosity structure of monoliths was analyzed by NOVA 4200e 152 surface area and pore size analyzer (Quantachrome Instruments) at 77 K through the Nitrogen adsorption/desorption isotherms. Before the analysis, the monoliths were freeze-dried overnight and then degassed at 70 °C under vacuum for six hours. The specific surface area and average pore size were calculated

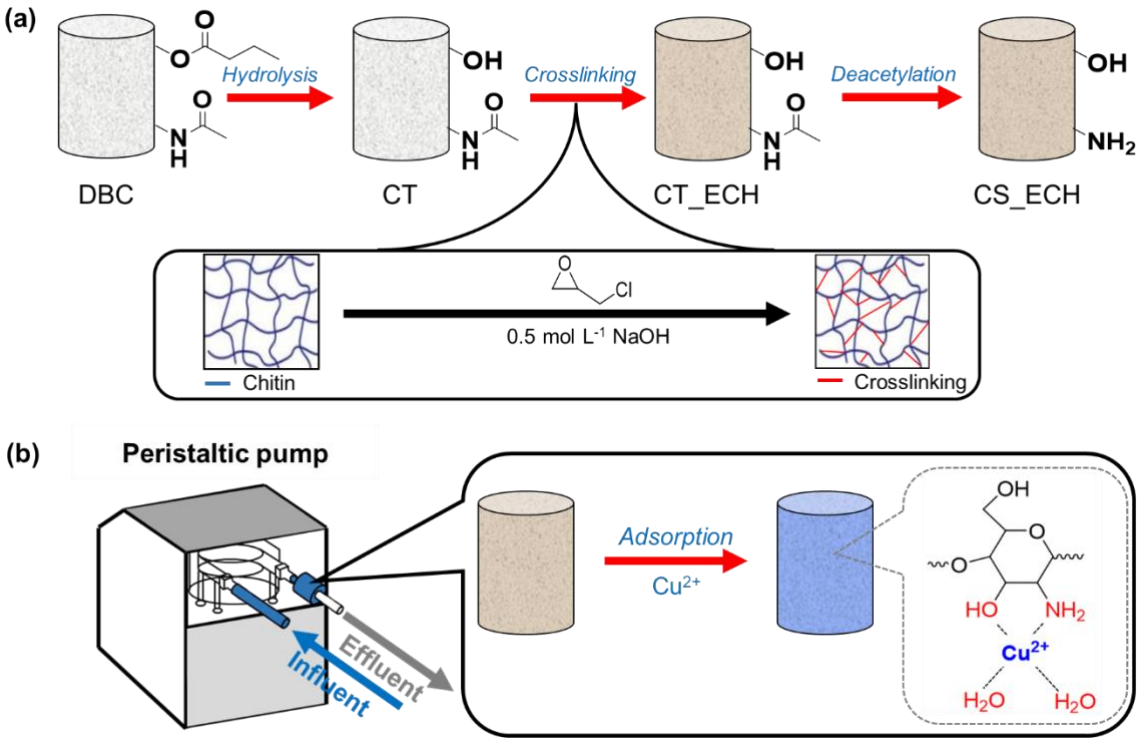

Figure 2-1. (a) Illustration of crosslinked CS monolith fabrication, and (b) schematic diagram of the adsorption process of CS monolith with Cu(II) solution.

using the Brunauer–Emmett–Teller (BET) and density functional theory (DFT) equations. The adsorption experiment was performed using the CS monolith assembled with a peristaltic pump to demonstrate the metal ion removal process (Figure 2-1(b)). The adsorption process was conducted by circulating high-concentration Cu(II) solution through the monolith, and the test was carried out until no changes in the solution concentration were observed. The change in the concentration of Cu(II) ion was determined by UV-visible spectra (V-750, Jasco) at wavelength 805 nm. The adsorption capacity was calculated from the equation as follows:[13]

$$Q = \frac{(C_0 - C_1) \times V}{m} \tag{2-1}$$

where Q is the adsorption capacity, C_0 and C_1 denote the initial and the final Cu(II) concentration, respectively; V is the volume of the Cu(II) solution; m is the monolith weight.

2.3 Results and discussion

2.3.1 Crosslinking CT monolith

The hierarchically porous CT monolith was prepared from DBC using the TIPS method. Before converting CT monolith to CS monolith, it was crosslinked with ECH to make CS monolith stable and maintain its strength in acidic conditions because acid environments cause the partial dissolution of CS. One of the problems related to crosslinking is that most crosslinking agents react with amino groups and reduce the monolith's adsorption capacity. However, the crosslinking reaction of ECH with CS is temperature-dependent. Below 40 °C, ECH is crosslinked with amino groups like other agents. However, above 40 °C, hydroxy groups also participate during crosslinking. This property of ECH makes it unique compared to other crosslinking agents.[14] Moreover, crosslinking reaction was started on CT monolith because amide groups are less reactive than amino groups, which forwards the crosslinking reaction to hydroxy groups. Therefore, large number of available amino groups were produced after deacetylation of the amide groups.

SEM images of CT monoliths were illustrated in Figure 2-2(a-d). From the images, it can be observed that crosslinking reaction did not significantly affect the porosity of the CT monolith. The average macropore diameter of non-crosslinked CT monolith and CT_ECH_1, CT_ECH_2, and CT_ECH_5 monoliths was determined as 4.5 ± 0.2 μm.

X-ray diffractometer was used to analyze the XRD profile of the CT monoliths and see the effect of ECH on their crystallinity (Figure 2-2(e)). In the non-crosslinked CT monolith, five distinctive peaks were observed at 9.14°, 12.64°, 19.38°, 22.34° and 26.40°, which correspond to 0 2 0, 0 2 1, 1 1 0, 1 3 0 and 0 1 3 diffraction peaks.[15,16] There was no significant change on the profile when looking at the crosslinked CT monoliths for CT_ECH_1 and CT_ECH_2. The crystalline peaks of the CT_ECH_5 was slightly shifted to 9.22°, 12.78°, 19.42°, 22.37° and 26.46°, respectively. This phenomenon could be attributed to modification in the arrangement of molecules in the crystal lattice. Crosslinking of CS with ECH might inhabit ECH the interstitial sites and reduce lattice spacing. Apart from this, the apparent similarities in diffraction patterns observed in all monoliths suggest that they retained the crystallinity derived from the CT monolith after crosslinking.

Compression deformation tests were performed to see the effect of crosslinking on the mechanical properties of CT monolith (Figure 2-3(a)). The result reveals that the non-crosslinking CT monolith showed a maximum strain beyond 80% without breaking. On the other hand, maximum strain of crosslinked CT monoliths is between 50-60%. Although flexibility at crosslinked monoliths decreased, they showed higher mechanical strength than non-crosslinked CT monolith, which confirmed the successful crosslinking reaction.

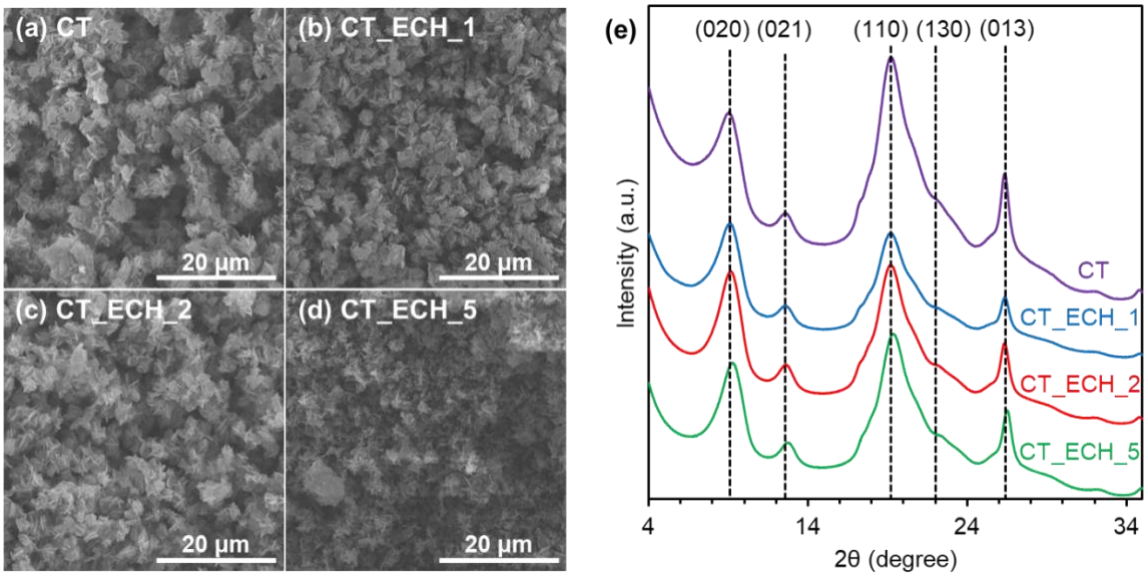

Figure 2-2. (a-d) SEM images of (a) CT, (b) CT_ECH_1, (c) CT_ECH_2, and (d) CT_ECH_5 monoliths. (e) XRD patterns of CT monoliths.

Other than mechanical properties, the thermal properties of monoliths were also analyzed in the range between 50 °C and 500 °C (Figure 2-3(b)). For all samples, two main steps of decomposition were observed. The first stage was seen around in the temperature range from 70 to 110 °C, attributed to water evaporation. The second main decomposition happened in the range at 288-402 °C for non-crosslinked CT, 281–400 °C for CT_ECH_1, 264–392 °C for CT_ECH_2, and 253–388 °C for CT_ECH_5 monolith, respectively. From the results, the degradation temperature decreases along with the increasing ECH ratio. The decline in the crosslinked samples can be explained by the large amount of ECH molecules, which weaken in intra- and intermolecular interactions of the hydrogen bonds present in the CT. The TGA characterization results also support ECH crosslinking with CT monoliths.

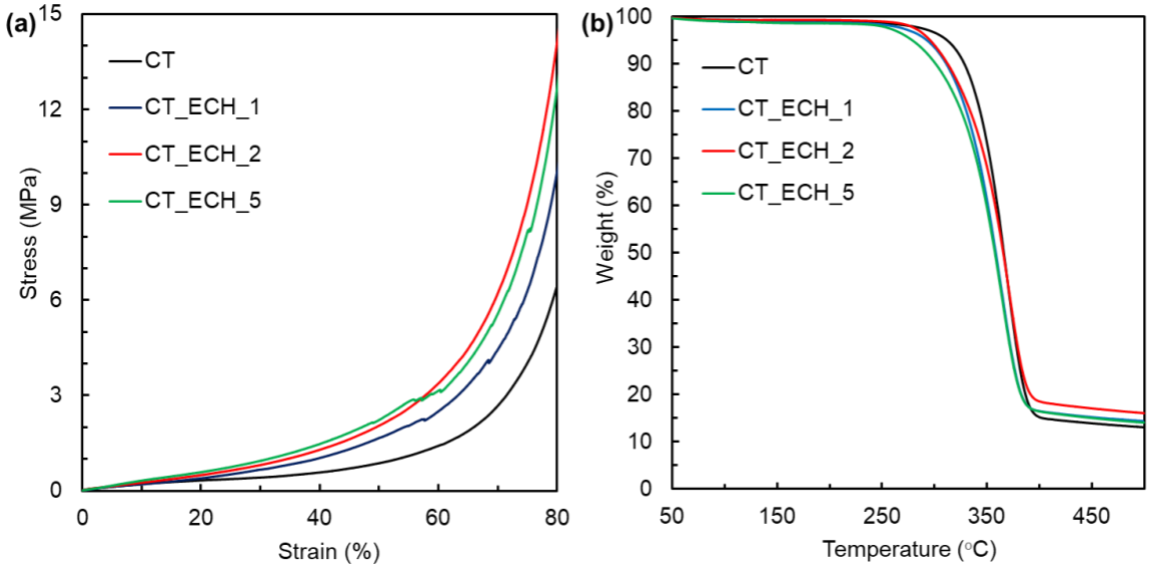

Figure 2-3. (a) Compression stress-strain curves and (b) TGA profiles of CT monoliths.

2.3.2 Deacetylation of CT monoliths to CS monoliths.

The deacetylation process refers to converting acetyl groups to reactive amino groups, whose amount is determined by the degree of the deacetylation percentage (DDA%). The boundary between CT and CS is 50% amino group; in other words, when DDA% is lower than 50%, it is CT, and when DDA% is higher than 50%, the polymer is considered CS.[17]

The determination of DDA% plays a crucial part in understanding whether the monolith is CS or still CT. In Figure 2-4, ^{1}H NMR profiles of the commercial CS powder and CS monolith treated with 8.0 mol L^{-1} NaOH were given. Several signals in the δ 3.5 – δ 4.0 ppm correspond to

the non-anomeric hydrogens H_3– H_6 from the ring and one at δ 3.1 ppm attributed to the hydrogen H_2 connected to the anomeric carbon C_2. In the region, δ 5.1 - δ 5.5 ppm, anomeric protons in H_1 of GlcNAc and GlcN units were observed. A strong band of intensity occurs at δ 4.6 - δ 5.0 ppm associated with HDO (solvent). The peak at δ 2.0 ppm indicates the methyl group of acetamide. A negligible amount of butylamide (observed around δ 2.1- δ 2.4 ppm), which was possibly formed in the synthesis of DBC from CT (inherently with free amino group), was remained after deacetylation process. The rest of the minor peaks correspond to impurities, which suggests that even after the solvent exchange, some impurities remain inside the monolith, which is difficult to remove. DDA% was estimated from the ^{1}H NMR data by the following formula:[18,19]

$$DDA\% = \left(1 - \frac{2I_{CH_3}}{I_{H_{2-6}}}\right) \times 100 \qquad (2\text{-}2)$$

where I_{CH_3} is the integral of methyl proton acetamide group and $I_{H_{2-6}}$ is the summation of integrals of H_2, H_3, H_4, H_5, and H_6. DDA% of the raw CS and CS monolith is calculated as 83 and 67%, respectively. Furthermore, the DDA% of CS monoliths treated with 10.0 mol L^{-1} and 12.0 mol L^{-1} NaOH solution was calculated as 68% and 75%, respectively. Because CS monolith with the treatment of 6.0 mol L^{-1} NaOH did not dissolve in a deuterium solvent, DDA% of the sample could not be determined. From this insolubility of the monolith, it can be understood that the percentage

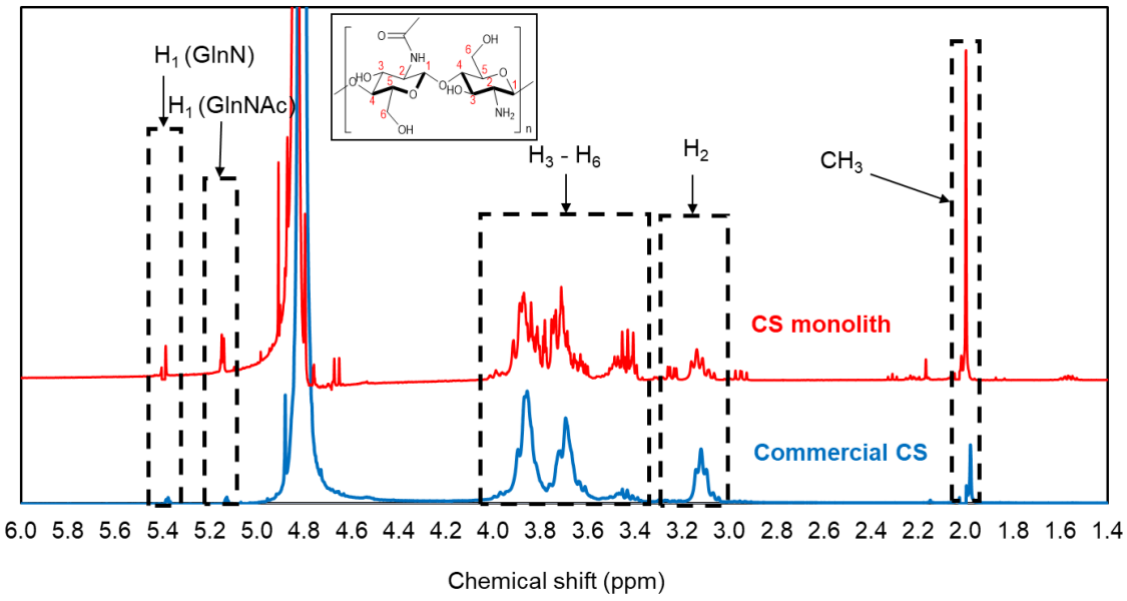

Figure 2-4. ^{1}H NMR spectra of commercial CS and CS monolith treated with 8.0 mol L^{-1} NaOH (samples were prepared by 1% DCl/D_2O solution).

of amino groups in the CS monolith with 6.0 mol L^{-1} NaOH treatment is low and closer to CT than CS. On the same grounds, none of the crosslinked CS monoliths were dissolved in deuterium solvent, it was challenging to calculate the DDA% of them.

After the deacetylation of CT monoliths to CS monoliths, the swelling test was carried out to see the behavior of monoliths in a solvent. In the swelling test, approximately 0.12-0.15 g CS monolith was immersed into 0.1 mol L^{-1} HCl solution for 24 h. Later, monoliths were taken from the solution; they were put onto the mesh for 10 min to remove excess solvent. The following formula was used to calculate the solvent uptake percentage of the monolith:[20]

$$SR\% = \frac{m_w - m_d}{m_d} \times 100\% \quad (2\text{-}3)$$

where, SR% is the percentage of swelling ratio, m_w and m_d are monolith's wet and dry weight, respectively. The swelling percentage of CS, CS_ECH_1, CS_ECH_2, and CS_ECH_5 monoliths were determined as 575%, 561%, 528%, and 526%, respectively. The result of SR% of monoliths reveals that the solvent uptake amount decreased when the ratio of crosslinking-agent increases. The non-crosslinked CS monolith showed the highest swelling ratio compared to crosslinked monoliths. Because primary amino groups of CS are protonated in an acidic environment, CS becomes polyelectrolyte and the monolith swells in an acid solution. Although CS monolith has low DDA%, the dissolution process might still occur due to the absence of crosslinking. On the other hand, in the crosslinked CS monoliths, as the crosslinking increases between the chains, the structure of the polymer becomes tighter, and the solvent cannot easily penetrate the polymer matrix. This results in less swelling and more durability in acidic solutions.

SEM images of CS monolith with different NaOH concentration treatments were shown in Figure 2-5(a-d). When the alkali concentration was increased from 6.0 mol L^{-1} to 12.0 mol L^{-1}, the average pore size of the CS_ECH_2 monolith decreased from 3.9 ± 0.2 to 2.7 ± 0.2 μm (Figure 2-5(e)). Other than this, unlike CT monoliths, the pore diameter of CS monoliths decreased as increasing the amount of ECH for crosslinking. For example, there is a slight difference in the average macropore size between non-crosslinking CS monolith and CS_ECH_5, treated with 8.0 mol L^{-1} NaOH, whose average pore diameter is 4.1 ± 0.2 μm and 3.9 ± 0.2 μm, respectively. The same decreasing trend can also be seen in other monoliths. In addition, when alkali concentration was higher than 8.0 mol L^{-1}, shrinkage was observed in both non-crosslinked and crosslinked monoliths. The diameter of the non-crosslinked CS monolith was shrunk from 5.9 ± 0.1 mm to 5.1

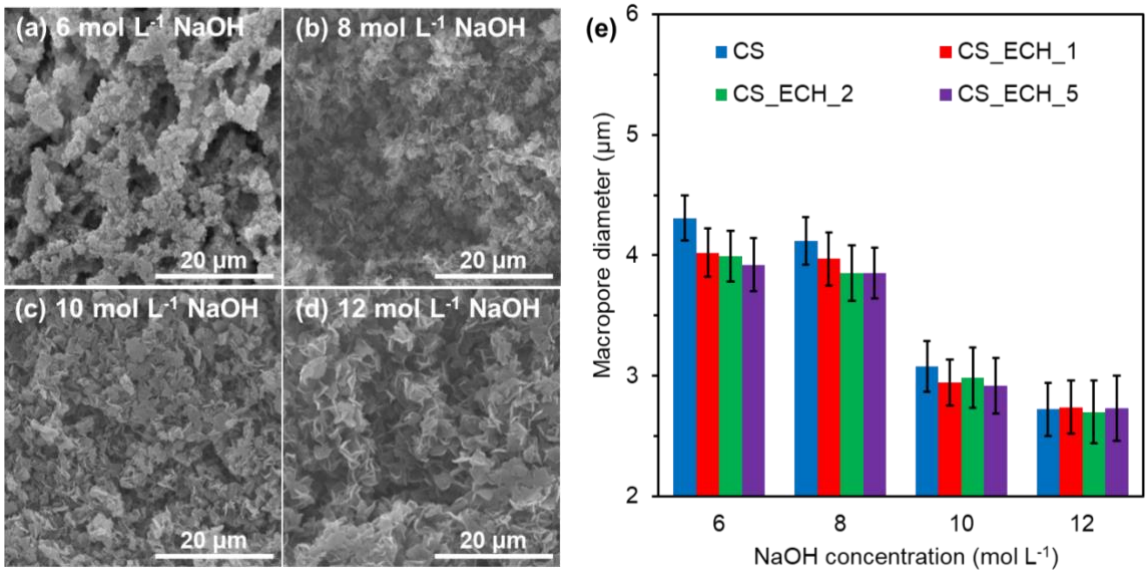

Figure 2-5. SEM images of CS_ECH_2 monoliths treated with (a) 6.0, (b) 8.0, (c) 10.0, and (d) 12.0 mol L^{-1} NaOH solution, and (e) average macropore size of all CS monoliths.

± 0.1 mm when the concentration of NaOH solution increased from 8.0 mol L^{-1} to 10.0 mol L^{-1}. With 12.0 mol L^{-1} NaOH solution treatment, the monolith was shrunk further to 4.6 ± 0.1 mm. A similar trend was also seen in crosslinked monoliths. The possible explanation for the reduction in both macropore size and diameter of monoliths could be related to change in the chemical structure. When CT lost the bulky amide group and converted into the amino group, the polymer structure become tighter due to hydrogen bonds and crosslinking. In addition to deacetylation, depolymerization might occur as well due to the highly concentrated alkali solution. However, since all monoliths retained their morphology after deacetylation, this effect appears negligible based on SEM images. From these results, CS monoliths treated with 8.0 mol L^{-1} NaOH solution were selected for the following analysis due to their porosity structure and DDA%.

Besides macroporous structure, the mesoporous features of CS monoliths were evaluated by nitrogen adsorption/desorption analysis. The isotherm and pore size distribution are shown in Figure 2-6. All the adsorption/desorption curves can be classified as Type IV with adsorption hysteresis loops H3 in terms of IUPAC classification, indicating the presence of mesopores. Furthermore, the average pore sizes of CS, CS_ECH_1, CS_ECH_2, and CS_ECH_5 monoliths were 3.6, 3.7, 3.6, and 3.5 nm, respectively, which are the range of mesopores (2-50 nm). In addition, the surface areas were determined to be 144 m^2 g^{-1} for the non-crosslinked CS, 142 m^2 g^{-1} for the CS_ECH_1, 148 m^2 g^{-1} for the CS_ECH_2, 141 m^2 $g^{-1,}$ for the CS_ECH_5 monoliths.

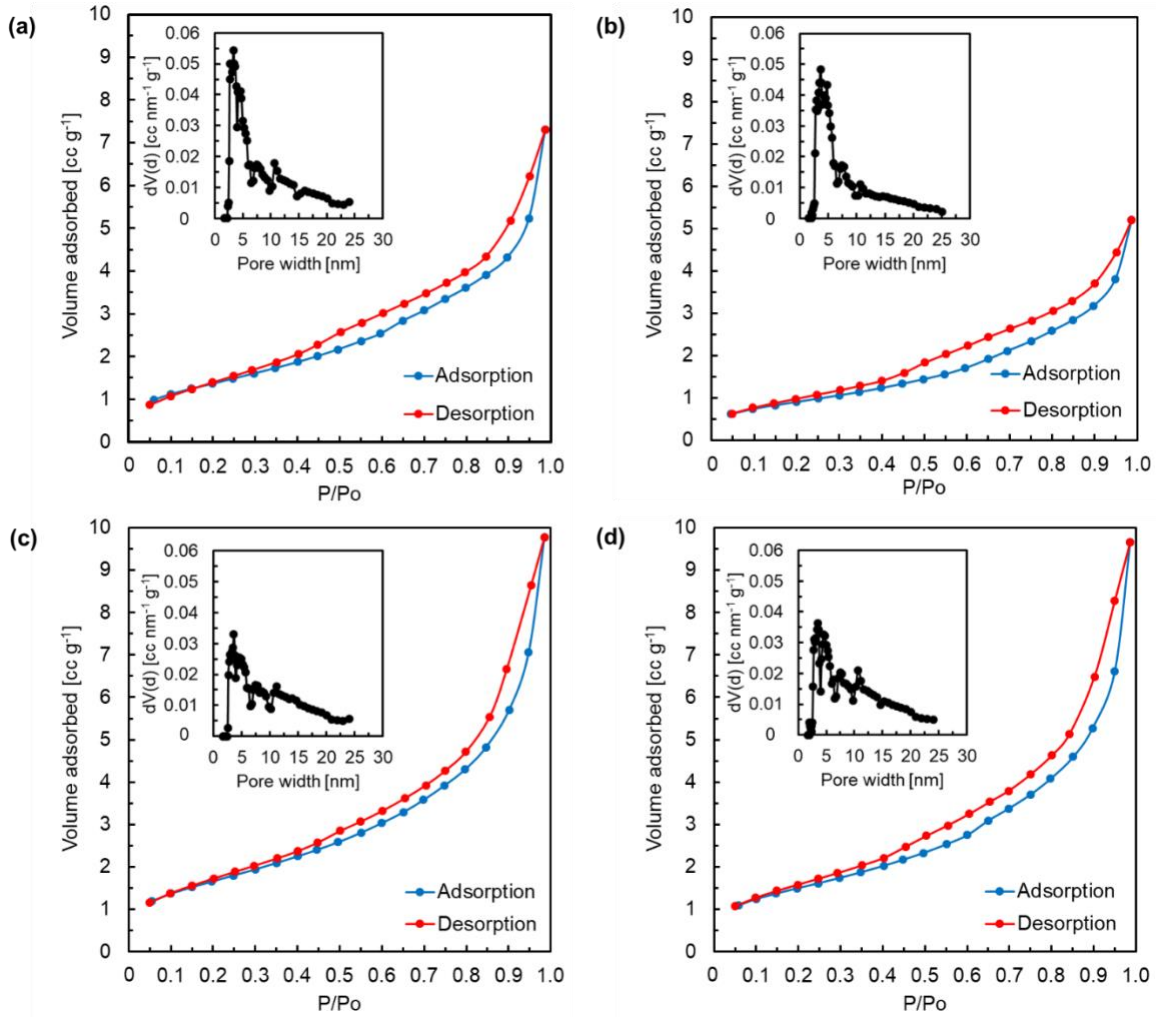

Figure 2-6. Nitrogen adsorption/desorption isotherms and pore size distribution curves of (a) CS, (b) CS_ECH_1, (c) CS_ECH_2, and (d) CS_ECH_5 monoliths.

This confirms that monoliths maintained their structure during deacetylation, and crosslinking reaction did not have any significant influence on surface area.

From these SEM images and N_2 adsorption-desorption isotherms, CS monoliths preserved their hierarchical porous structure after deacetylation. Figure 2-7(a) reveals the XRD pattern of non-crosslinked CS monolith. Similar to the CT monolith, the CS monolith also has four distinct peaks, which were 0 2 0 at 9.14º, 0 2 1 at 12.64º, 1 1 0 at 19.38º, and 0 1 3 at 26.40º. This concludes no obvious difference between CT monolith and CS monolith regarding crystallinity.

The thermal property of the CS monolith was also analyzed (Figure 2-7(b)) and compared with that of the CT monolith. The CS monolith also showed two main decomposition steps like the CT monolith. The first stage of decomposition started at 60 °C, and only a small weight percent

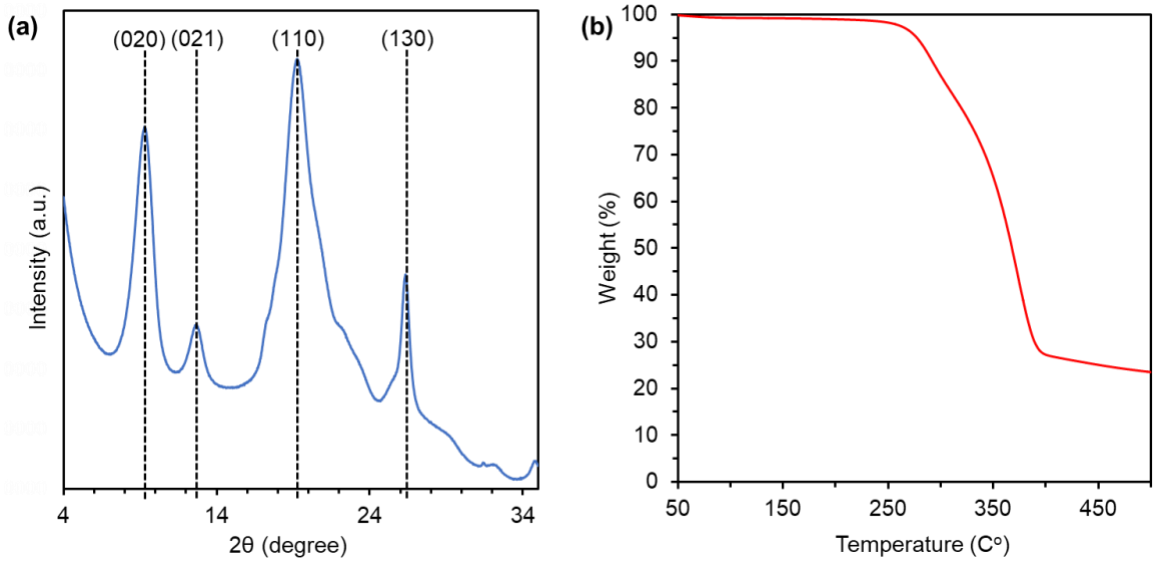

Figure 2-7. (a) XRD pattern and (b) TGA profile of non-crosslinked CS monolith.

of the samples was lost. This stage corresponds to water evaporation. The second stage occurred in the temperature range from 250 to 392 °C and was attributed to degradation of the polymer chain. As a result, there is a slight difference on thermal stability between CT and CS monoliths.

2.3.3 Adsorption studies

The fabricated CS monoliths were used to capture metal ions from the solution for the application point. The adsorption experiments were conducted with a peristaltic pump circulating 0.1-3.5 g L^{-1} of Cu(II) solution through the CS monoliths. Regarding optimization of the adsorption process, the effect of the pH on the adsorption process was analyzed. The evaluation of the pH effect was conducted by adjusting the initial pH of the solution using 0.1 mol L^{-1} HCl and 0.1 mol L^{-1} NaOH. To eliminate the temperature influence, the temperature was set to 25 °C. As shown in Figure 2-8(a), at pH 5.5, CS monolith achieved the highest adsorption capacity, which indicates the optimum value for adsorption studies. Regarding pH of the solution, two main factors play important role here. One of them is the abundance of H^+ in the low pH solution, which competed with the metal ions for the limited amino groups of the CS. When primary amino group of CS get protonated, it resulted in electrostatic repulsion with positive charged metal ions and decreased adsorption capacity.[21] On the other hand, at the high pH, solubility of the Cu(II) ions decreased and precipitation occurred, which limits amount of Cu(II) to be captured.[22] In Figure 2-8(b),

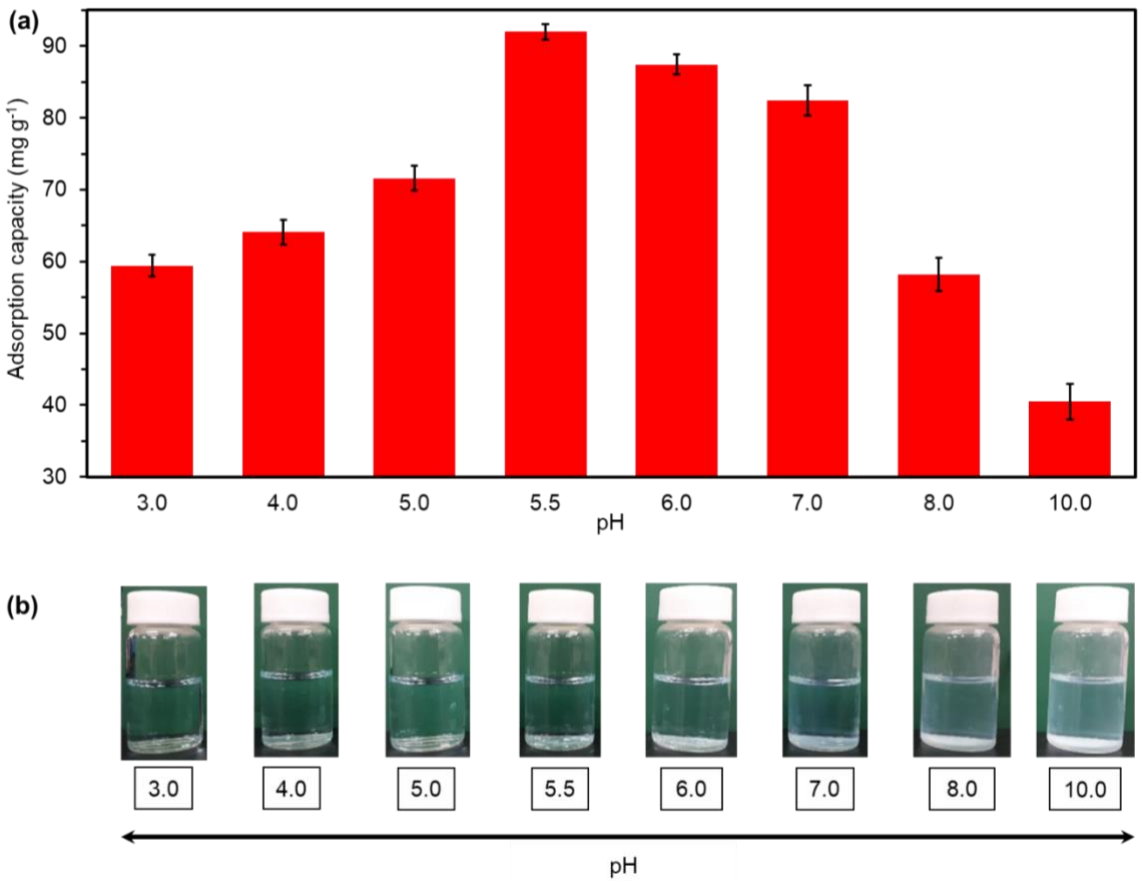

Figure 2-8. Effect of pH on (a) adsorption capacity and (b) solubility of Cu(II).

precipitation of Cu(II) solution on high pH can be seen. Thus, based on these two factors, pH 5.5 was optimum value to obtain the maximum adsorption capacity.

After determining the optimum pH condition, CS monoliths were analyzed for the dynamic adsorption studies to investigate the metal adsorption behaviors with multiple repetitions. In addition, under working conditions of pH 5.5 and 25 °C, a series of experiments were carried out to verify the connection between the adsorption capacity and Cu(II) concentration, as shown in Figure 2-9(a). The collected data was analyzed using the Freundlich and Langmuir isotherm models (Table 2-2). The equations for Freundlich (Eq. 2-4) and Langmuir (Eq. 2-5) isotherm models are shown below:[23]

$$\log Q_e = \log K_f + \frac{1}{n}\log C \tag{2-4}$$

$$\frac{C_e}{Q_e} = \frac{1}{Q_m}C_e + \frac{1}{K_a Q_m} \tag{2-5}$$

where Q_e (mg g^{-1}) is the adsorption capacity at equilibrium, C_e (mg L^{-1}) is the Cu(II) concentration at equilibrium, K_f (L mg^{-1}) is the Freundlich constant, n is the heterogeneity factor, and K_a (L mg^{-1}) and Q_m (mg g^{-1}) are the Langmuir coefficients, indicating an adsorption equilibrium constant and a monolayer capacity, respectively. Freundlich model explains that the sites on the adsorbent surface are not equal and result in multilayer adsorption, while the Langmuir model represents monolayer adsorption on an energetically uniform surface. Both Freundlich and Langmuir parameters and fitting curves showed in Table 2-2 and Figure 2-9(b,c), respectively. The Langmuir

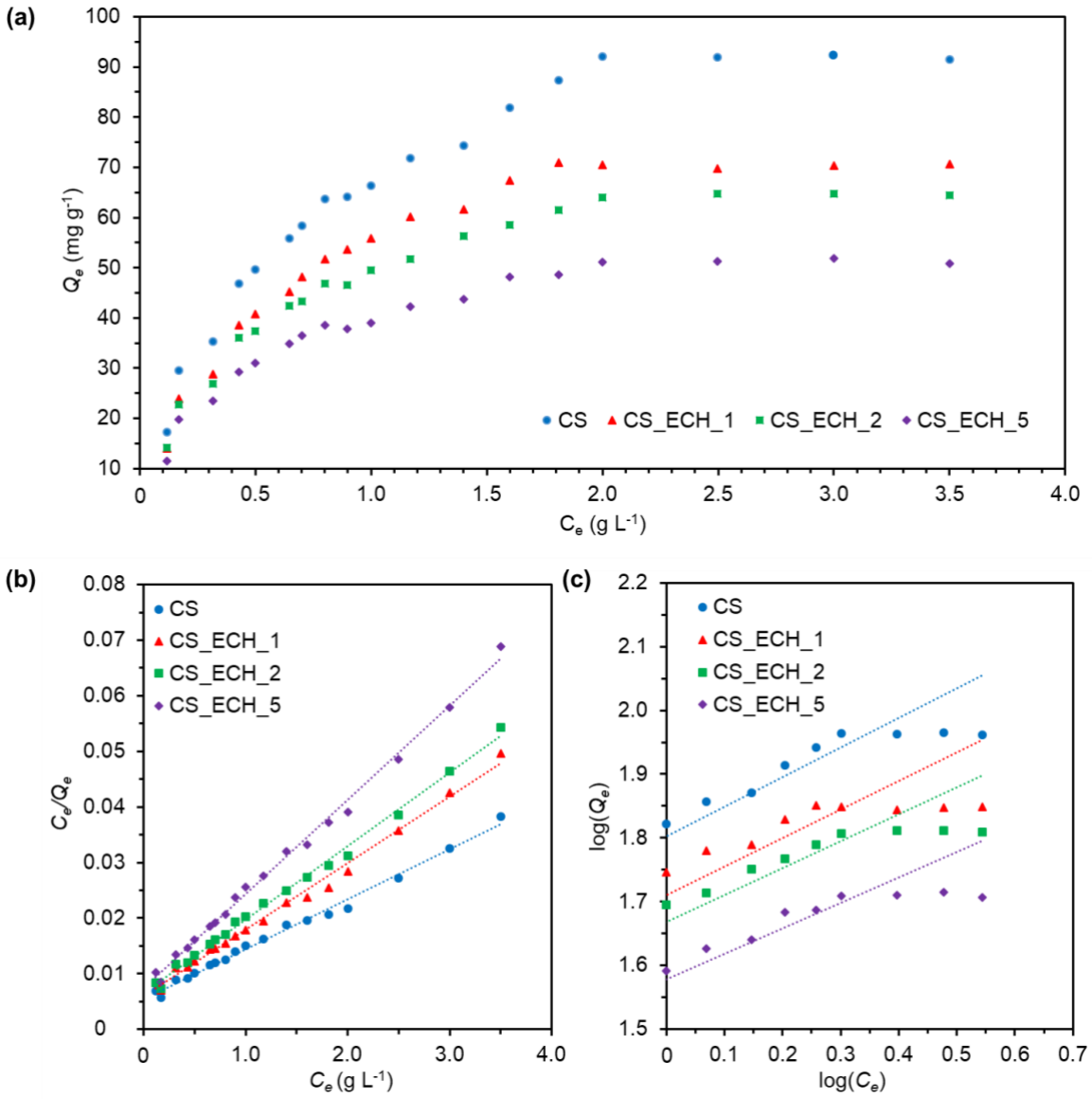

Figure 2-9. (a) Adsorption isotherms of a Cu(II) by CS monoliths and (b) the Langmuir and (c) the Freundlich isotherm plots.

model matches with the Cu(II) adsorption data better than the Freundlich model for all CS monoliths. The square error for Langmuir is identified as $R^2 > 0.99$ for all CS monoliths, while for Freundlich, it is between 0.91 and 0.94. This concludes that monolayer adsorption is more dominant compared to multilayer adsorption.[23] From the slope, the maximum adsorption capacity of monoliths was determined as 96 mg g^{-1}, 73 mg g^{-1}, 65 mg g^{-1}, and 51 mg g^{-1} for CS, CS_ECH_1, CS_ECH_2, and CS_ECH_5 monoliths, respectively, implying its universal practicability for heavy metal ion removal.

Table 2-2. Adsorption isotherm parameters.

	CS	CS_ECH_1	CS_ECH_2	CS_ECH_5
Freundlich				
R^2	0.936	0.912	0.930	0.913
1/n	0.492	0.477	0.447	0.438
K_f	1.82	1.75	1.69	1.59
Langmuir				
R^2	0.992	0.993	0.996	0.995
Q_m	95.5	72.9	65.3	51.2
K_a	0.190	0.225	0.216	0.244

In the same manner as adsorption isotherms, the adsorption kinetics were also investigated with multiple filtration repetitions. Adsorption kinetic studies were conducted with 2.5 g L^{-1} Cu(II) solution under optimized working conditions of pH 5.5 and 25 °C. Figure 2-10(a) revealed that the adsorption capacity of all the CS monoliths increased with the reaction time, and the adsorption rate slowed down at the time after 60 min and became stable. This is due to the fixed amount of amino group, and fewer adsorption sites became available with time. Finally, the adsorption capacity of the adsorbent reaches saturation. To understand the mechanism of the kinetics, the pseudo-first-order (PFO, Eq. 2-6), the pseudo-second-order (PSO, Eq. 2-7) were analyzed:[13]

$$\ln(Q_e - Q_t) = \ln Q_e - k_1 t \quad (2\text{-}6)$$

$$\frac{t}{Q_t} = \frac{1}{k_2 Q_e^{\ 2}} + \frac{t}{Q_e} \tag{2-7}$$

where Q_e and Q_t are the adsorption capacities at equilibrium and at time t (min), respectively, and k_1 and k_2 are the rate constants. The PFO model states that if one of the two reactants is in more significant excess, its relative concentration will remain constant. In other words, adsorbate can be captured by an adsorbent at a constant rate.[24] PSO-governed systems, however, exhibit complex rate constants that depend on initial solute concentration.[25] During adsorption, the PFO only applies during the initial stages, while the PSO applies over an extended period of time.[26] Based on the values of R^2 , although the monoliths showed a good fit to both PFO and PSO kinetic models

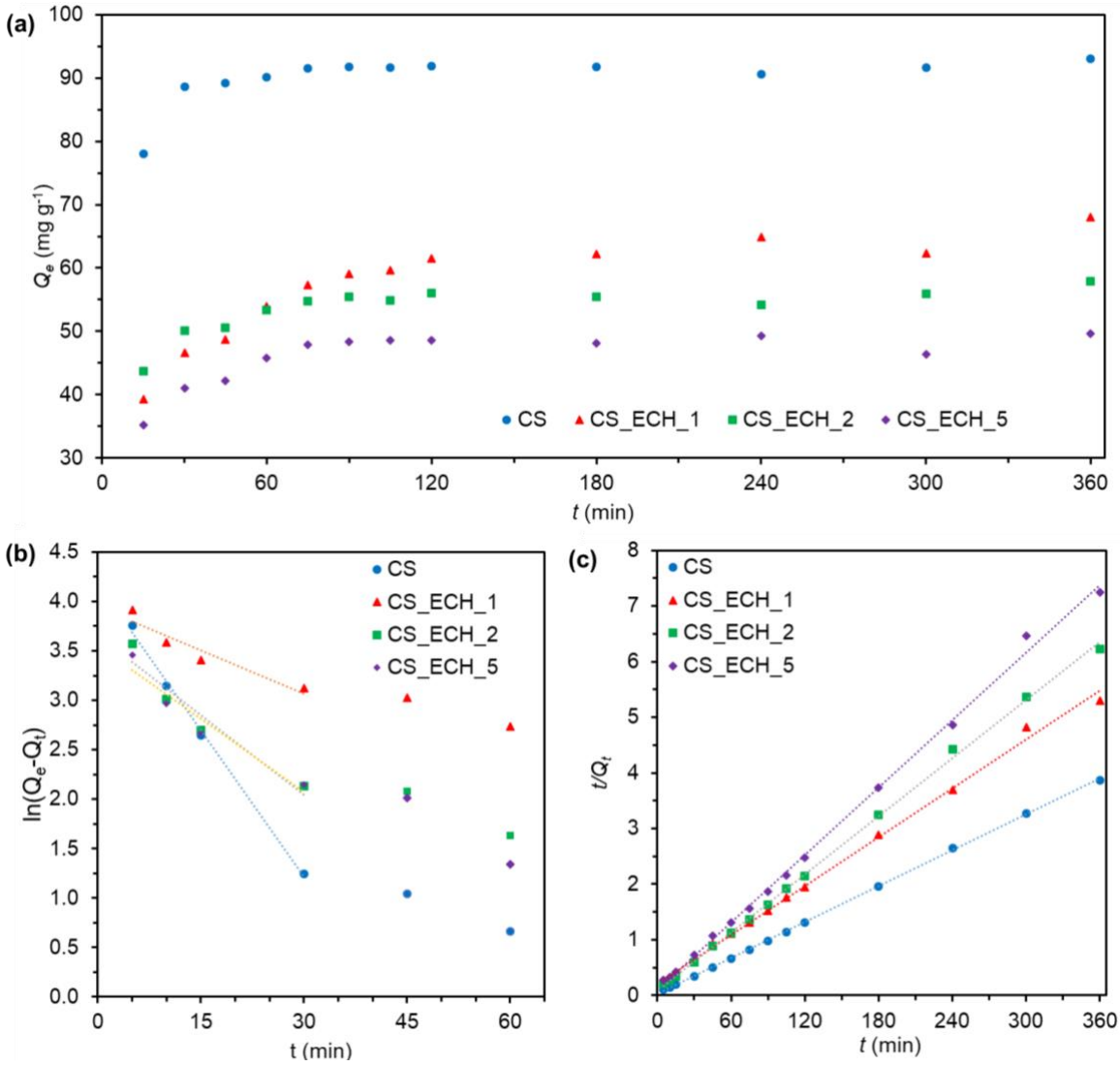

Figure 2-10. (a) Adsorption kinetic of a Cu(II) by CS monoliths, and linear fit curves for (b) PFO and (c) PSO models.

Table 2-3. Kinetic models and parameters.

	CS	CS_ECH_1	CS_ECH_2	CS_ECH_5
PFO				
R^2	0.932	0.954	0.884	0.952
Q_e	27.1	40.5	22.2	25.8
k_1	0.0158	0.00667	0.00890	0.00774
PSO				
R^2	0.999	0.997	0.999	0.998
Q_e	93.0	64.8	57.3	47.7
k_2	0.00385	0.00379	0.00380	0.00399

(Figure 2-10(b,c)), the PSO gave a better fit for adsorption data than PFO with respect to linearity coefficients obtained with 0.999, 0.997, 0.999, 0.998 for CS, CS_ECH_1, CS_ECH_2, and CS_ECH_5 monoliths, respectively (Table 2-3). Furthermore, the theoretical Q_e obtained by PSO (93, 65, 57, and 48 mg g^{-1}) kinetics is closer to the actual measurement results (92, 71, 64, and 51 mg g^{-1}). As a result, the PSO model better describes the process of heavy metal ions adsorbing on CS monoliths.

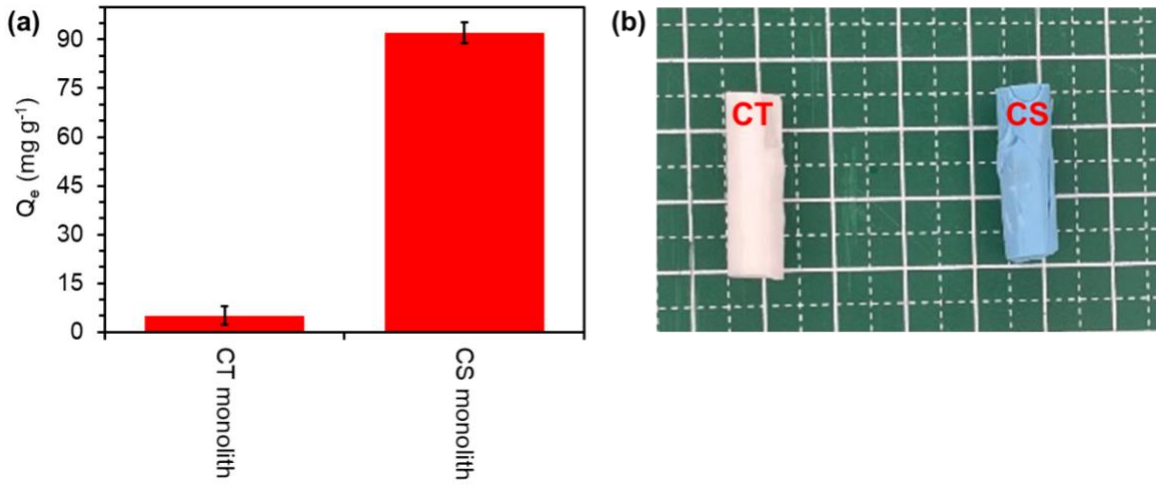

Figure 2-11. (a) the adsorption capacity of CT and CS monoliths and (b) the photograph of CT and CS monoliths after adsorption experiment.

After determining the CS monolith's adsorption capacity, that of CT monolith was also tested with 2.5 g L^{-1} Cu(II) solution under optimized working conditions of pH 5.5 and 25 °C (Figure 2-11(a)). It can be seen that the CT monolith could not capture Cu(II) ions from an aqueous solution due to the insufficient amount of amino groups to interact with Cu(II) ions. In addition, after adsorption, the CS monolith changed color to blue, confirming the adsorption of Cu(II) ions; while the CT monolith did not change color significantly (Figure 2-11(b)).

Having good stability and reusability are the necessary objective for ideal absorbent. Therefore, the adsorption-desorption cycles were performed to investigate the reusability of CS monoliths for practical applications. For the desorption process, 0.02 mol L^{-1} EDTA at pH 8.0 was

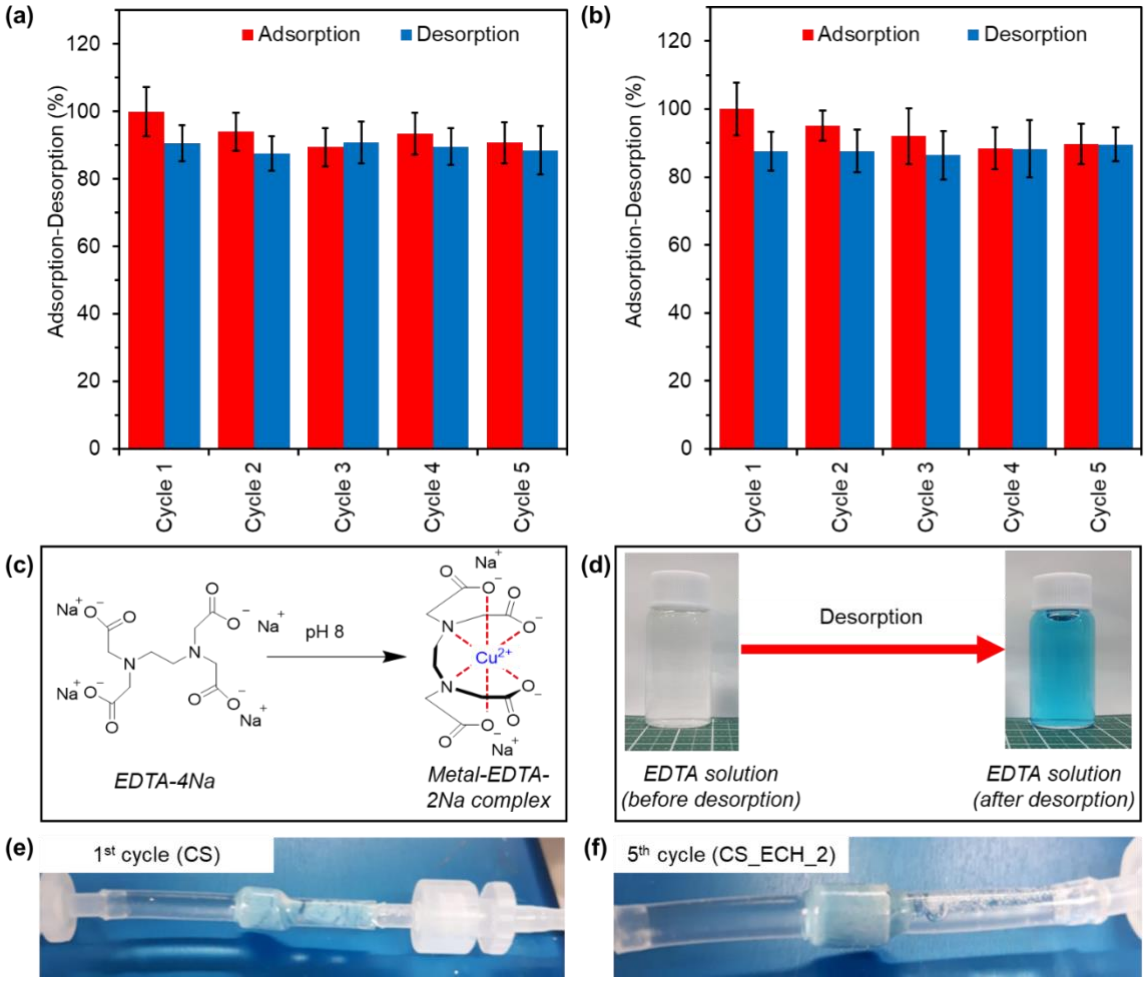

Figure 2-12. Adsorption-desorption cycles of (a) CS_ECH_2 and (b) CS_ECH_5 monoliths. (c) Scheme and (d) photograph of EDTA solution before and after desorption. Photograph of desorption process of (e) CS (1st cycle) and (f) CS_ECH_2 (5th cycle) monoliths.

used to remove metal ions from the CS monolith. Only performance of CS_ECH_2 and CS_ECH_5 monolith was measured for the reusability studies. After five cycles, for CS_ECH_2 monolith, the adsorption and desorption efficiencies were 91 ± 6% and 89 ± 7%; and, CS_ECH_5 monolith's efficiency was 90 ± 6% for adsorption and 90 ± 5% for desorption (Figure 2-12(a-b)). During the adsorption process, all monoliths, including the non-crosslinked CS monolith, maintained their structure and did not dissolve when the Cu(II) solution passed through them in the adsorption process.

Figure 2-12(c) shows the scheme for the removal of metal ions with the EDTA. As shown in Figure 2-12(d), the EDTA solution became blue after desorption, indicating that it can remove metal ions from the CS monoliths. During the desorption process, the non-crosslinked CS and CS_ECH_1 monoliths collapsed during the first cycle of the desorption process (Figure 2-11e). This indicates that both monoliths are not durable in basic conditions (pH 8.0). On the other hand,

Table 2-4. Comparison of adsorption performances of CS materials for the removal of Cu(II) from aqueous solutions.

Materials	Adsorption system	Q_e (mg/g)	Adsorption time	References
Carboxymethylated chitosan-bound Fe_3O_4 nanoparticles	Batch	21.5	~ 60 min	[27]
Chitosan-coated magnetic particles	Batch	35.5	~ 8 h	[28]
ZnO@Chitosan core-shell nanocomposite	Batch	117.6	60 min	[29]
Chitosan beads	Batch	80.7	60-90 min	[30]
Polyaniline graft chitosan beads	Batch	83.3	90 min	[31]
Chitosan monoliths doped with graphene oxide	Batch	53.7	1-8 h	[12]
3D printed chitosan filter	Flow	13.7	75 min	[10]
CS monolith	Flow	92.1	60 min	This study

CS_ECH_2 and CS_ECH_5 monoliths preserved their shape and did not show any dissolution within five cycles (Figure 2-12(f)). These results demonstrated that both monoliths could be used multiple times without losing significant efficiency. From the adsorption-desorption, it was concluded that the ECH crosslinking needs to be at least a 1:2 molar ratio for the CS monolith to be used multiple times.

Table 2-4 provides a comparison of the CS monolith with previously reported studies. The CS monoliths in this research showed better performance than most of other researches with 92 and 64 mg/g adsorption capacities for non-crosslinked CS and crosslinked CS_ECH_2 monoliths, respectively, with 60 min adsorption time. Furthermore, in most of these studies, CS was either dissolved in acidic solutions and performed to react with metal ions in which CS was considered for single use or designed to be used in batch systems which are not an ideal method to remove metal ions from wastewater in industry since it requires more time and energy. Meanwhile, the prepared CS monolith with stability against acidic and basic media and reusability has demonstrated its effectiveness in a flow system with high adsorption capacity, indicating that it could be used in practical wastewater treatment processes.

2.4 Conclusions

This study achieved a hierarchically porous CS monolith, exhibiting effective heavy metal ion removal properties. Before deacetylation reaction from CT to CS, CT monoliths were crosslinked by ECH with varied ratios and characterized by compression tests, XRD, and TGA analysis. It is revealed that the crosslinking by ECH increases the durability of CS monoliths against an acidic environment. In the adsorption experiments, CS monoliths was able to be used in a continuous flow system with high performance due to its hierarchically porous morphology. The macroporous structure of the monolith allows water to flow rapidly; on the other hand, the mesoporous structure, which has a large surface area, achieved a high adsorption capacity for capturing Cu(II) ions from the aqueous solution. Remarkably, the CS_ECH_2 monolith showed a good adsorption capacity and preserved its stability within five adsorption-desorption cycles without losing significant efficiency. These findings state that CS monoliths are a promising candidate for large-scale application in metal removal from wastewater as a chelating agent.

References

[1] Y. Liu, P. Wang, B. Gojenko, J. Yu, L. Wei, D. Luo, T. Xiao, *Environ. Pollut.* **2021**, *291*, 118209.

[2] C. Zamora-Ledezma, D. Negrete-Bolagay, F. Figueroa, E. Zamora-Ledezma, M. Ni, F. Alexis, V. H. Guerrero, *Environ. Technol. Innov.* **2021**, *22*, 101504.

[3] Y. Zhang, M. Zhao, Q. Cheng, C. Wang, H. Li, X. Han, Z. Fan, G. Su, D. Pan, Z. Li, *Chemosphere* **2021**, *279*, 130927.

[4] H. Hamedi, S. Moradi, S. M. Hudson, A. E. Tonelli, M. W. King, *Carbohydr. Polym.* **2022**, *282*, 119100.

[5] J. Lizardi-Mendoza, W. M. Argüelles Monal, F. M. Goycoolea Valencia, *Chitosan in the Preservation of Agricultural Commodities* **2016**, 3-31.

[6] T. Chandy, C. P. Sharma, *Biomater. Artif. Cells Artif. Organs* **1990**, *18*, 1.

[7] J. Wang, C. Chen, *Bioresour. Technol.* **2014**, *160*, 129.

[8] T. Y. Chen, H. P. Cho, C. S. Jwo, L. Y. Jeng, *Adv. Mater. Sci. Eng.* **2013**, *2013*, 686409.

[9] J. Wang, S. Zhuang, *J. Clean Prod.* **2022**, *355*, 131825.

[10] D. Zhang, J. Xiao, Q. Guo, J. Yang, *J. Mater. Sci.* **2019**, *54*, 6728.

[11] Y. Zhang, W. Yan, Z. Sun, C. Pan, X. Mi, G. Zhao, J. Gao, *Carbohydr. Polym.* **2015**, *117*, 657.

[12] Y. Wang, X. Liu, H. Wang, G. Xia, W. Huang, R. Song, *J. Colloid. Interface Sci.* **2014**, *416*, 243.

[13] G. W. Kajjumba, S. Emik, A. Öngen, H. K. Ö. and S. Aydın, In *Advanced Sorption Process Applications* (Ed.: Edebali, S.), IntechOpen, Rijeka, **2018**, p. 1-19.

[14] H. Zheng, Y. M. Du, J. H. Yu, L. Xiao, *Chem. J. Chinese U.* **2000**, *21*, 809.

[15] G. Cárdenas, G. Cabrera, E. Taboada, S. P. Miranda, *J. Appl. Polym. Sci.* **2004**, *93*, 1876.

[16] R. S. Dassanayake, S. Acharya, N. Abidi, In *Advanced Sorption Process Applications* (Ed.: Edebali, S.), IntechOpen, Rijeka, **2018**, p. 1-24.

[17] S. M. Taghizadeh, G. Davari, *Carbohydr. Polym.* **2006**, *64*, 9.

[18] R. Czechowska-Biskup, D. Jarosińska, B. Rokita, P. Ulański, M. J. Rosiak, *Prog. Chem. Appl. Chitin Deriv.* **2012**, *17*, 5-20.

[19] Y. Jiang, C. Fu, S. Wu, G. Liu, J. Guo, Z. Su, *Mar. Drugs* **2017**, *15*, 332.

[20] X. Sun, T. Fujimoto, H. Uyama, *Polym. J.* **2013**, *45*, 1101.

[21] B. Abbar, A. Alem, S. Marcotte, A. Pantet, N. D. Ahfir, L. Bizet, D. Duriatti, *Process Saf. Environ. Prot.* **2017**, *109*, 639.

[22] J. D. Cuppett, S. E. Duncan, A. M. Dietrich, *Chem. Senses.* **2006**, *31*, 689.

[23] T. S. Khayyun, A. H. Mseer, *Appl. Water Sci.* **2019**, *9*, 170.

[24] R. L. Tseng, F. C. Wu, R. S. Juang, *J. Taiwan Inst. Chem. Eng.* **2010**, *41*, 661.

[25] S. Azizian, *J. Colloid. Interface Sci.* **2004**, *276*, 47.

[26] Y. S. Ho, G. McKay, *Process Saf. Environ. Prot.* **1998**, *76*, 332.

[27] Y. C. Chang, D. H. Chen, *J. Colloid. Interface Sci.* **2005**, *283*, 446.

[28] C. Yuwei, W. Jianlong, *Chem. Eng. J.* **2011**, *168*, 286.

[29] A. H. A. Saad, A. M. Azzam, S. T. El-Wakeel, B. B. Mostafa, M. B. Abd El-latif, *Environ. Nanotechnol. Monit. Manag.* **2018**, *9*, 67.

[30] V. Patrulea, A. Negrulescu, M. M. Mincea, L. Pitulice, O. B. Spiridon, V. Ostafe, *Bioresources* **2013**, *8*.

[31] E. Igberase, P. Osifo, A. Ofomaja, *J. Environ. Chem. Eng.* **2014**, *2*, 362.

Chapter 3

Enzyme Immobilization Utilizing Hierarchically Porous Chitosan Monolith

3.1 Introduction

Enzymes are highly efficient and environmentally friendly, and they are widely used as catalysts for biochemical reactions, providing an alternative lower-activation-energy reaction pathway. Owing to their low toxicity, favorable selectivity, and inertness against secondary reactions, they are preferred over traditional chemical processes.[1–3] α-Amylase (1,4-D-glucan glucanohydrolase) is a commercial enzyme used in food processing and drug and pharmaceutical applications and catalyzes the breakdown of the α-D-(1,4) glycosidic linkages of glycogen, starch, and other oligosaccharides.[4–6] However, traditional batch reactions have limitations, as the enzymes cannot be recovered and reused, and they have low storage stability and high production costs.[2,7] Therefore, the immobilization of amylases through different physicochemical treatments is necessary for their large-scale industrial use.[8] To address these challenges, enzyme immobilization has emerged as a promising solution. This approach involves attaching enzymes to a support material, reducing their mobility while maintaining catalytic activity.[9–11] Numerous immobilization methods have been investigated over the past few decades, including covalent binding, physical adsorption, entrapment, and crosslinking.[3,12] The most common and simplest immobilization method is physical adsorption, which involves various noncovalent interactions, such as van der Waals forces and hydrogen bonds.[13] Although enzymes immobilized via physical adsorption exhibit high activity, they exhibit low stability because of weak bonds between the enzyme and carrier.[14] Covalent bonds are widely used for immobilizing enzymes, and creates strong interactions between enzymes and supports, increases enzyme stability and reusability, and prevents enzyme release into the reaction mixtures by reducing the mobility and conformational changes of the enzymes.[15] However, covalent bonding causes a considerable loss of enzymatic activity upon immobilization, posing a significant disadvantage.[16] Therefore, a method combining both physical adsorption and covalent binding is necessary to increase enzyme stability and maintain enzyme activity.

The stability and efficiency of enzyme immobilization can be affected by the support materials. Support materials can be categorized as organic and inorganic materials, based on their

chemical composition. An ideal support material should facilitate easy substrate access to the active sites of the enzymes. Additionally, it should be inert to the supported enzymes, inexpensive, resilient against physical degradation due to microbial attack, and hydrophilic. Porous materials, especially, hierarchically structures, are highly efficient functional materials for realizing enzyme applications in flow systems. Several porous materials such as reactive polymers,[17] graphene oxide,[18] metal-organic framework materials,[19] and mesoporous silica[20] have been utilized for enzyme immobilization. Nevertheless, these materials often have drawbacks such as high cost, complexity, and partial harm to environment. In addition, most of these are designed for batch systems, restricting their scalability in industrial applications. The use of natural polymers as carrier materials has been gaining growing interest owing to their desirable characteristics such as biocompatibility, non-toxicity, and bioactivity.[21] CS is derived from CT, offers several advantages including cost-effectiveness and wide availability.[22] CS effectively binds to enzymes owing to its structural composition, which incorporates both amino and hydroxy groups.[23,24] This unique feature makes CS a well-suited support material for enzymes, facilitating enzyme immobilization and enhancing enzyme stability.

This study introduces a novel and practical method for immobilizing α-amylase on a hierarchically porous CS monolith. Expanding upon chapter 2, the morphology of the monolith was optimized to achieve optimum α-amylase activity. The immobilization technique integrates physical adsorption and covalent bonding to enhance the stability of α-amylase at different pH levels and temperatures when compared to its soluble form. The presence of amino and hydroxy groups in CS allows effective physical binding with the enzyme, while the epoxy group in the monolith provides additional stability via covalent bonding between the stationary phase and the enzyme (Figure 3-1). Additionally, high porosity and permeability of CS monolith preserve the high reaction rate of the immobilized enzymes and maintain their substrate affinity. The preparation conditions were optimized based on immobilization efficiency, enzymatic activity, storage stability, and reusability. Additionally, the versatility of this method was demonstrated by fabricating CS monoliths with other enzymes, such as lipase and catalase. Overall, this study contributes to the field of enzyme immobilization by providing valuable insights into harnessing the hierarchical porous structure of CS monoliths. It addresses the limitations in current techniques by offering an optimized immobilization method that enhances enzyme stability, activity, and

substrate affinity. The findings have implications for efficient enzyme utilization in flow systems and hold promise for cost-effective enzyme applications in various industrial systems.

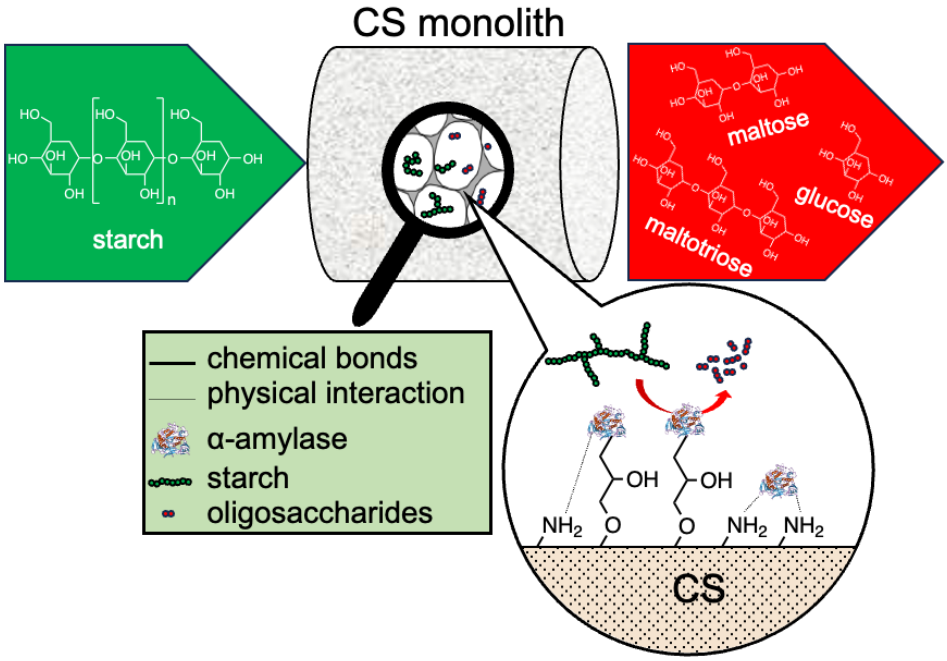

Figure 3-1. General mechanism of catalytic reaction enzyme which immobilized with combination of adsorption and covalent bonding on CS monolith.

3.2 Experimental section

3.2.1 Materials

CT from shrimps, α-amylase from *Bacillus sp.*, lipase from *Aspergillus Niger*, and catalase from bovine liver were purchased from Sigma-Aldrich. NaOH and epichlorohydrin (ECH) were purchased from FUJIFILM Wako Pure Chemical Corporation. Other reagents were of analytical grade and used without further purification.

3.2.2 Fabrication of CS monoliths

CS monoliths were fabricated using a thermally induced phase-separation method, as described in Chapter 2. The monoliths were fabricated as follows. 5 g CT powder was mixed with a solution of 95 mL butyric anhydride and 2.2 mL 70% perchloric acid and stirred for 3 h at 20 °C. The mixture was then poured into deionized water having a pH of 7. The resulting solid product was collected, dried, and dissolved in acetone while stirring. The acetone–polymer solution was

filtered to remove insoluble materials and then poured into deionized water for precipitation. The precipitate was composed of white flocculent pure dibutyrylchitin (DBC), which was collected and dried.

To prepare the monoliths, a calculated amount of DBC was completely dissolved in DMSO at 85 °C, and deionized water was added to the solution at different ratios. The solution was stirred at 85 °C for 3 h and left overnight at 25 °C. CT monoliths were obtained by hydrolyzing the DBC monolith using an aqueous NaOH solution (1.0 mol L^{-1}). For crosslinking the CT monoliths, another NaOH solution (0.1 mol L^{-1}) was prepared, and a specific amount of ECH was added to the solution and stirred for 5 min. The amount of ECH was calculated according to the molecular weight of the repeated monosaccharide units in CT. The CT monoliths were then immersed and degassed in the ECH–NaOH solution at 60 °C for 3 d. To obtain the CS monoliths, the CT monoliths were immersed in concentrated NaOH solution (8.0 mol L^{-1}) and left undisturbed for 3 d at 60 °C. After washing with water, ethanol, and hexane, the CS monoliths were dried under vacuum at 25 °C. The list of prepared CS monoliths was shown in Table 3-1.

Table 3-1. List of fabricated CS monoliths.

Sample name	DBC concentration ($g\ L^{-1}$)	CS:ECH (mol:mol)
CS60	60	1:0
CS80	80	1:0
CS100	100	1:0
CS120	120	1:0
CS_ECH_3	100	1:3
CS_ECH_5	100	1:5
CS_ECH_10	100	1:10
CS_ECH_20	100	1:20

3.2.3 Characterization

The molecular structure of CS monoliths was analyzed by proton nuclear magnetic resonance (^{1}H NMR) spectroscopy using 1% deuterium chloride/deuterium oxide mixture as a solvent with JNM-ECS400 (400 MHz, JEOL). The amount of the epoxy group functionalized on the surface of the CS_ECH monolith was determined based on the reaction with sodium thiosulfate and titration of the released OH- by 0.01 M HCl.[25,26] The microscopic structures of the monoliths were observed using a scanning electron microscope (SEM, Hitachi S-3000N) operated at 15 kV. During sample preparation, a thin section of the monoliths was pasted onto a stub and coated with

a thin layer of gold using an ion-sputtering apparatus (E-1010, Hitachi). ImageJ software was used to calculate the average macropore diameter of the monoliths using the SEM images of three different monoliths from each sample. Before the analysis, the pixel distance ratio was set based on a known scale bar. Subsequently, the images were binarized, with black representing the pores and background and white indicating the polymer structure. The particle function was used to estimate particle size and circularity. The average macropore diameter was calculated assuming that the pores were circular. The porosity of the monoliths was analyzed using nitrogen adsorption/desorption isotherms and a surface-area and pore-size analyzer (Quantachrome Instruments, NOVA 4200e 152) at 77 K. Before the analysis, the monoliths were freeze-dried overnight and degassed at 70 °C under vacuum for 6 h. The specific surface area and average pore size were then calculated using the Brunauer–Emmett–Teller (BET) (Eq. 3-1) and density functional theory (DFT) (Eq. 3-2) equations.[27]

$$1/W\left(\left(P/P_0\right)-1\right)=\frac{1}{W_mC}+\frac{C-1}{W_mC}\left(P/P_0\right) \tag{3-1}$$

$$N\left(P/P_0\right)=\int_{D_{min}}^{D_{max}} N(P/P_0,D)f(D)\,dD, \tag{3-2}$$

where W is the mass adsorbed at relative vapor pressure; P and P_0 are the actual and saturated vapor pressures of adsorbate; W_m is the required mass of adsorbate forming a complete monolayer adsorbed on a given sample; and C is BET constant; $N(P/P_0)$ experimental adsorption data; $f(D)$ is an unknown pore diameter distribution function; and D_{min} and D_{max} are the minimum and maximum pore sizes, respectively.

3.2.4 Immobilization of enzymes on monoliths

Monoliths with immobilized enzymes were prepared by circulating a solution (1 mg/mL) of the enzymes and a 0.05 M phosphate buffer at pH 6.5 through the monoliths by peristaltic pump for at least 2 h. After immobilization, the monoliths were washed with the 0.05 M phosphate buffer and deionized water to remove unbound enzymes. The monoliths with the immobilized enzymes were then stored at 4 °C for further testing. The bicinchoninic acid (BCA) method was used to determine the amount of immobilized α-amylase. This method was performed using a BCA protein assay kit (Thermo Scientific Pierce) according to the instructions of the manufacturer. Six buffer solutions with known enzyme solution concentrations (0, 0.2, 0.4, 0.6, 0.8, and 1.0 mg L^{-1}), along

with unknown concentrations acquired from adsorption, were prepared to construct a calibration curve. For each sample solution, 25 μL of the solutions was taken thrice and added to a well microplate. Subsequently, 200 μL of the working reagent was added to each well filled with the samples. The samples were then incubated for 2 h at 37 °C and their absorbance was measured at 562 nm by microplate reader (Corona SH-9000Lab). The amount of the immobilized enzyme was calculated using the following equation.[28]

$$Q = \frac{(C_0 - C_1) \times V}{m} \tag{3-3}$$

where Q is the amount of enzyme immobilized on the monolith (mg/g), C_0 and C_1 denote the initial and final concentrations of the enzyme in the solution (mg/mL), respectively, V is the volume of the immobilized enzyme solution (mL), and m is the dry monolith weight (g).

3.2.5 Determination of α-amylase activity

The activities of the immobilized and free enzymes were measured using the degradation of starch into oligosaccharides. Soluble starch (10 mL, 1%) was dissolved in the 0.02 M phosphate buffer solution (pH 6.5) phosphate buffer solution and circulated through the enzyme-immobilized CS monoliths at 40 °C for 10 min. For assessing the activities of the free enzyme, α-amylase (1 mg) was added to a starch solution (10 mL) and placed in a bioshaker for 10 min at 40 °C. After 10 min, 0.3 mL of the sample was taken from the starch solution and added to a 3,5-dinitrosalicylic acid (DNSA) reagent (0.3 mL) to terminate the reaction. The test tubes containing the samples were incubated in a boiling water bath for 10 min and then cooled to room temperature. Distilled water (3 mL) was poured into the tubes and thoroughly mixed. Subsequently, the amount of reduced sugar (maltose) produced in the tubes was spectrophotometrically determined at 540 nm. A calibration curve was prepared using maltose solutions with different concentrations in a 0.02-M phosphate buffer having a pH of 6.5. An activity unit was defined as the amount of enzyme required to produce 1 mol of maltose per minute.

For both immobilized and free α-amylases, 1% of starch solution with a phosphate buffer at different pH values ranged from 3.5 to 8.5 at 40 °C for 10 min were used to investigate the effect of pH on their activity. The temperature effect was investigated under 1% starch solution prepared with phosphate buffer (0.05 M, pH 6.5) for 10 minutes at different temperatures from 30 to 60 °C.

The kinetic behavior of the enzymatic reaction was determined by varying the starch concentration under standard conditions and comparing the results to those obtained using the free enzyme. The kinetic parameters, Michaelis–Menten constant (K_m) and maximum reaction velocity (V_m), for free and immobilized α-amylase were determined using the Lineweaver–Burk plot.[29] The initial reaction velocity was calculated using the following equation.

$$[v] = \frac{C_{maltose}}{t} \tag{3-4}$$

where $[v]$, $C_{maltose}$, and t denote the reaction velocity, concentration of maltose formed after 10 min of the reaction, and reaction time, respectively.

On the basis of the Lineweaver–Burk plot, the Michaelis–Menten equation can be expressed as follows.

$$\frac{1}{[v]} = \frac{K_m}{V_m} \times \frac{1}{[S]} + \frac{1}{V_m} \tag{3-5}$$

where K_m is the Michaelis constant, which characterizes the enzymatic affinities with substrates, V_m is the maximum velocity, which represents the activity of the enzyme, and $[S]$ is the concentration of starch solution.

The storage stability of the free and immobilized enzymes was evaluated by measuring their residual activity after 56 d of storage in a 4 °C, pH 6.5 phosphate buffer. The residual activity of the enzymes was determined by calculating the ratio of the remaining activity to the initial activity of each enzyme at the time of storage.

To evaluate the reusability of the monolith, 7 cycles of repeated usage were conducted. The initial activity of the monolith was considered as the 100%, serving as a reference to assess the percentage activity after each cycle of reuse. After each cycle, the monolith was washed with water and a buffer solution to remove any residual reaction mixture or products. Following the wash, the monolith was placed back into a fresh reaction mixture, and the enzymatic activity was measured again.

3.2.6 Determination of lipase activity

The enzymatic activities of free and immobilized lipases were assessed via the hydrolysis of 4-nitrophenyl palmitate (*p*-NPP).[30,31] First, a 15-mM solution of *p*-NPP and isopropanol was mixed with a 10-mM phosphate buffer (pH = 7.2) at a ratio of 3.5/96.5 (*p*-NPP/phosphate buffer).

Owing to the low solubility of *p*-NPP in the phosphate buffer, a higher concentration of *p*-NPP may result in precipitation. The *p*-NPP solution (10 mL) was then circulated through the lipase-immobilized CS monoliths at 40 °C. For determining the activity of the free lipases, lipase (1 mg) was added to the *p*-NPP solution (10 mL) and placed in a bioshaker for 10 min at 40 °C. After 10 min, 1 mL sample was taken and diluted with 1 mL phosphate buffer (pH = 7.2). The solution was analyzed through spectrophotometry at 410 nm. A calibration curve was prepared using 4-nitrophenol (*p*-NP) solutions with different concentrations.

3.2.7 Determination of catalase activity

A reaction mixture (10 mL) consisting of H_2O_2 (10 mM) and phosphate buffer (pH = 7.5) was first circulated through catalase-immobilized CS monoliths at room temperature. To terminate reaction, 1 mL sample was taken and diluted with 0.1 M HCl. Catalase activity was then determined spectrophotometrically by measuring the decrease in the absorbance of H_2O_2 at 250 nm in the reaction mixture containing.[32,33] For determining the activity of free catalase, catalase (1 mg) was added to the H_2O_2 solution (10 mL) and placed in a bioshaker for 10 min at 25 °C. A calibration curve was then constructed using different concentrations of H_2O_2.

3.3 Results and discussion

3.3.1 Effect of pore size of the monolith on α-amylase immobilization

In a previous chapter, it was observed that the CS monoliths exhibited a hierarchical porous structure characterized by high surface area and permeability. The pore sizes can be adjusted by modifying the porous structure and adopting optimal configurations, allowing the enzymes to fit well within the monoliths for efficient substrate transformation. In particular, the hierarchical pore structure enhances substrate accessibility to the active sites of the enzyme. Mesopores promote the diffusion of reactants into the material, whereas macropores facilitate a smooth fluid flow through the material. Therefore, to investigate the effect of pore size on enzyme immobilization, various CS monoliths were prepared by varying the initial polymer concentration.

Figure 3-2(a–d) show the nitrogen adsorption/desorption isotherms and pore size distribution curves of the CS monoliths for various polymer concentrations. As per IUPAC classification norms, all adsorption/desorption curves can be classified as Type IV, with adsorption hysteresis loops of H3, indicating the presence of mesopores. The average pore sizes of the CS60, CS80,

CS100, and CS120 monoliths were measured as 9.3 nm, 6.8 nm, 5.9 nm, and 3.9 nm, while the surface areas were determined as 144 $m^2 g^{-1}$, 147 $m^2 g^{-1}$, 155 $m^2 g^{-1}$, and 143 $m^2 g^{-1}$, respectively. The results confirm that the studied monoliths possess mesoporous structures with suitable pore sizes and large surface areas. These characteristics are desirable for enzyme immobilization. The presence of mesopores facilitates an efficient diffusion of molecules and provides a high surface area for interactions, making these materials promising candidates for enzyme immobilization.

SEM analysis revealed that the CS monoliths contained macroporous features, in addition to the mesoporous structure. As shown in Figure 3-3(a–d), the density and compactness of the structures increase and the pore size reduces with increasing polymer concentration. As the polymer concentration increases from 60 g L^{-1} to 120 g L^{-1}, the average diameter of the macropores decreases from 4.1 ± 0.6 μm to 2.7 ± 0.2 μm.

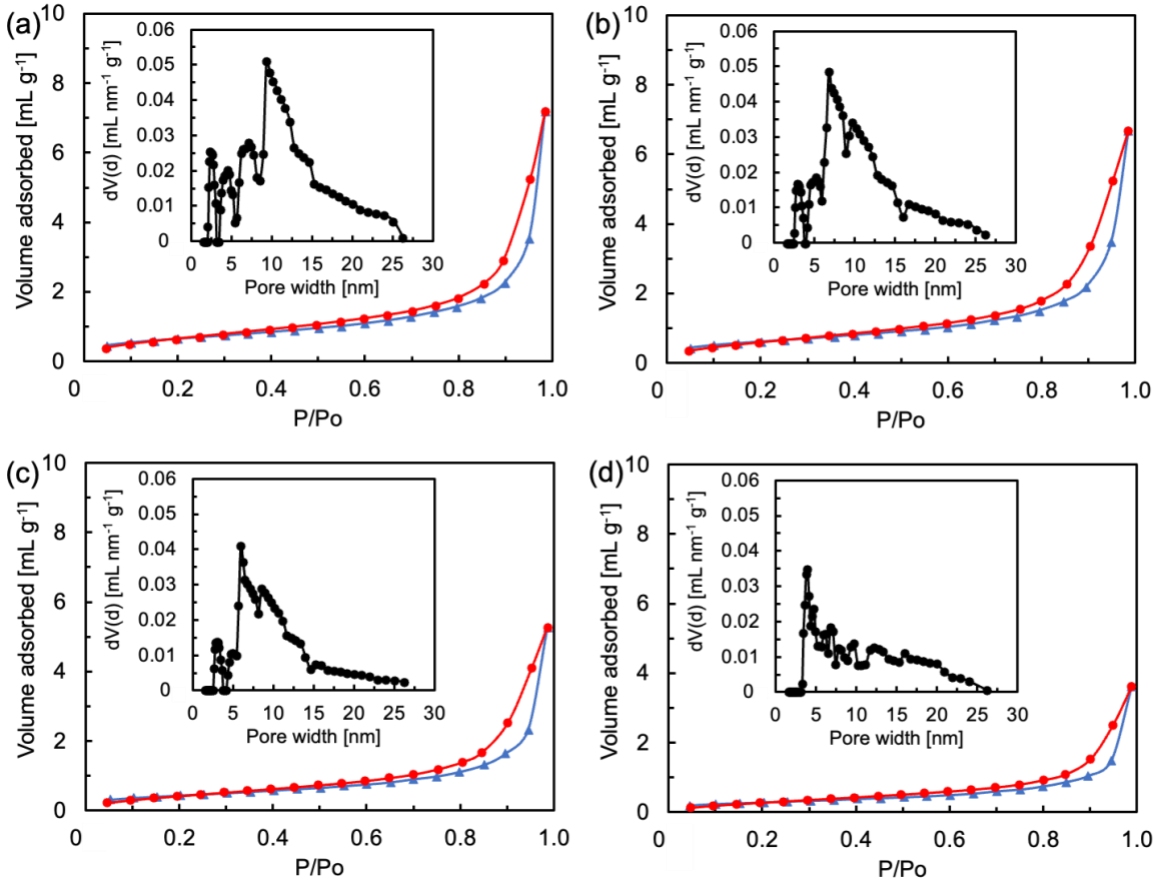

Figure 3-2. Nitrogen adsorption (▲) /desorption (●) isotherms and pore size distribution curves of (a) CS60, (b) CS80, (c) CS100, and (d) CS120 monoliths.

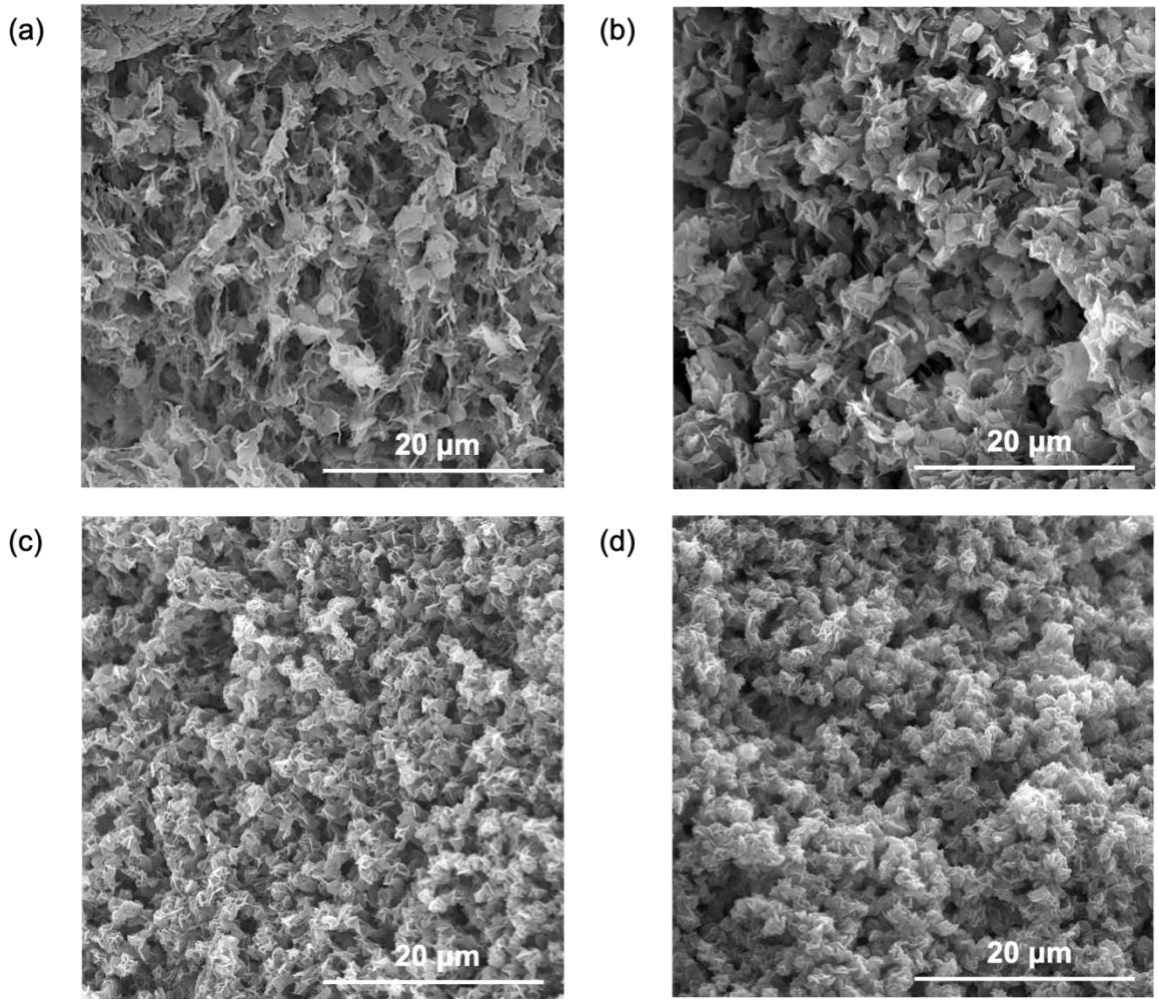

Figure 3-3. (a) SEM images of (a) CS60, (b) CS80, (c) CS100, and (d) CS120 monoliths.

The pore size of CS monoliths for enzyme immobilization was analyzed by using flow system adsorption. Figure 3-4 shows the relationship between pore size and the amount of immobilized enzyme for each CS monolith. Among the monoliths, CS100 immobilizes the highest amount of the enzyme. The lower immobilization efficiencies of the CS60 and CS80 monoliths can be attributed to their larger pore sizes, which induces higher enzyme leakage from the matrix. During immobilization, some enzymes are washed away from the monoliths, leading to reduced immobilization. However, the CS100 monolith, owing to its smaller pore size, can entrap the enzyme within its matrix, resulting in a higher extent of immobilization. By contrast, the CS120 monolith demonstrates a lower enzyme immobilization capacity, which can be attributed to its permeability. The lower permeability of the CS120 monolith limits the access of the α-amylase

enzyme to the available adsorption sites within the monolith, resulting in decreased immobilization efficiency.

As evident from the SEM images and N_2 adsorption–desorption isotherms, porous structure of CS100 monolith provides the optimal environment for enzyme immobilization. The macroporous structure of CS100 monolith allows enzyme solution to flow rapidly; meanwhile, the mesoporous structure, with a large surface area, is able to adsorb α-amylase efficiently. Additionally, using data from the BCA assay and N_2 adsorption/desorption, it was calculated that the CS monolith surface can accommodate approximately 1.3×10^{15}, 1.4×10^{15}, 1.6×10^{15}, and 9.6×10^{14} molecules/m^2 of enzymes for CS60, CS80, CS100, and CS120, respectively (more detailed calculations can be found in the supplementary information). These findings highlight that CS100 is more suitable for immobilization. For further experiments, CS monoliths with a polymer concentration of 100 g L^{-1} were used.

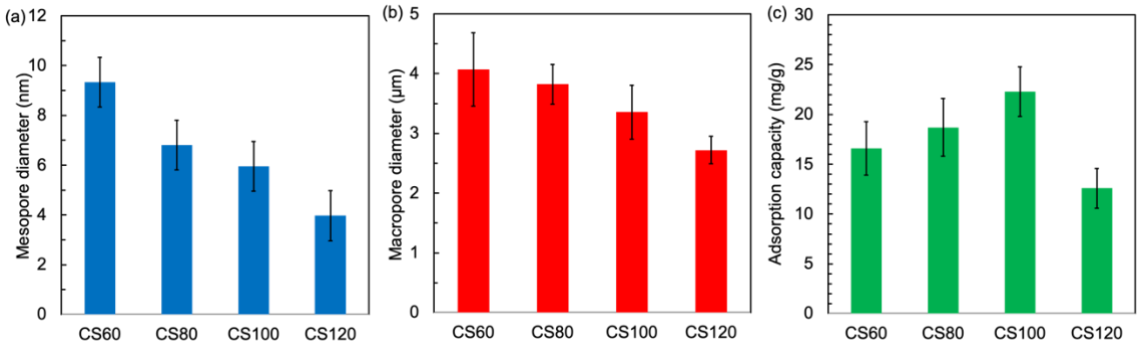

Figure 3-4. Average (a) mesopore and (b) macropore diameter of the CS monoliths, and (c) the immobilization α-amylase capacity for CS monoliths.

3.3.2 Effect of crosslinking ratio on α-amylase immobilization and activity

Physical adsorption is a simple method for enzyme immobilization. This method maintains enzyme activity but may not provide sufficient stability for long-term applications. To enhance the stability and activity of enzymes, additional methods, such as covalent bonding, must be used. Covalent binding involves the formation of stable covalent bonds between the enzyme and matrix, typically using crosslinking agents or functional groups on the support material. Most crosslinking agents react with amino groups owing to the high activity of the amino groups. The consumption of amino groups reduces the adsorption capacity of the monolith. However, the crosslinking of ECH with CS is temperature-dependent. Below 40 °C, ECH behaves similarly to other crosslinking

agents by primarily reacting with the amino groups present in CS. However, above 40 °C, the hydroxy groups in ECH also participate in crosslinking. This feature makes ECH unique compared to other crosslinking agents.[34,35] This opens up the possibility of utilizing hydroxy groups for crosslinking reactions, which can be advantageous for enzyme immobilization. In this study, the crosslinking reaction was initiated on the CT monolith rather than on the CS monolith. Compared to amino groups, amide groups in CT are less reactive. Hence, the crosslinking reaction proceeds towards the hydroxy groups, generating a significant number of available amino groups after deacetylation. The amount of reactive epoxy groups incorporated in the various CS_ECH monoliths was estimated by sodium thiosulfate/HCl titration. The epoxy content of the CS_ECH_3, CS_ECH_5, CS_ECH_10, and CS_ECH_20 monoliths was measured as 180 μmol/g, 199 μmol/g, 284 μmol/g, and 335 μmol/g, respectively. It was observed that the incorporation of epoxy groups can be increased by increasing the feed ratio of ECH in the crosslinking reaction. During the crosslinking process, a portion of the ECH effectively enhances the chemical and physical stability of the CS monolith, making it more robust and resistant to degradation. Simultaneously, the unreacted epoxy groups that remain after crosslinking play a crucial role in enzyme immobilization through covalent bonding. These unreacted epoxy groups can form stable covalent bonds with enzymes, creating a strong attachment and preventing enzyme leaching. The amount of enzyme immobilization can be controlled by adjusting the feed amount of ECH during the crosslinking reaction. To investigate the role of crosslinking reactions on enzyme immobilization, crosslinked CS100 monoliths put in continuous flow system to capture enzyme molecules from flow solution. The results revealed that the amount of immobilized α-amylase on the monoliths increased with increasing ECH concentration (Figure 3-5(a)). This indicated that both amino groups and ECH played a crucial role in immobilizing α-amylase on the monolith. The incorporation of ECH into the crosslinking reaction introduced additional covalent bonds within the CS monolith structure. These covalent bonds enhanced the stability and robustness of the CS matrix for enzyme immobilization. While non-covalent adsorption forces could contribute to enzyme immobilization, the formation of covalent bonds between the enzyme and CS matrix through crosslinking further enhanced the stability of the enzyme and reduced the risk of enzyme leaching. Among the fabricated monoliths, CS_ECH_20 exhibited the highest enzyme immobilization. This suggested that an increased ECH concentration in the crosslinking reaction increased the number of covalent bonds and consequently increased the number of immobilized

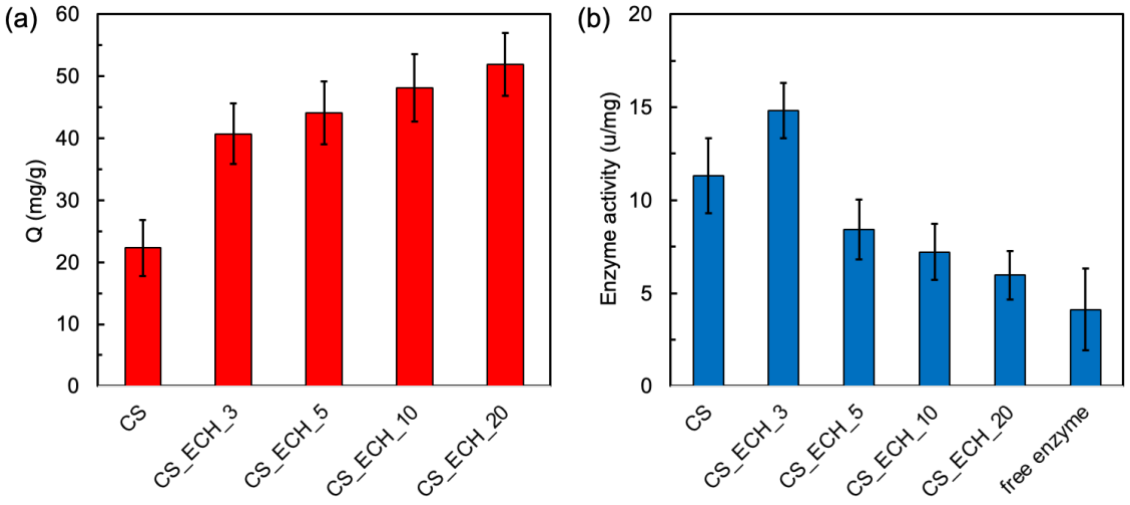

Figure 3-5. (a) Immobilization efficiency and (b) activity α-amylase on the CS monoliths.

enzymes via reaction probable to proceed between glycidyl group on the monolith and amino groups of the enzyme. Therefore, the CS_ECH_20 monolith exhibited a favorable immobilization efficiency; However, the CS_ECH_3 monolith was found to have the highest activity when immobilized enzymes on monoliths degraded starch into oligosaccharides in a flow system at 40 °C (Figure 3-5(b)). A possible explanation is that ECH is an active chemical, and its excessive use may cause enzyme denaturation or structural alterations, affecting the overall activity. Nevertheless, compared to free α-amylase, all immobilized samples exhibited improved activity. This indicated that, compared to the soluble form of α-amylase, immobilized α-amylase provided higher enzyme stability and activity, regardless of the specific ECH ratio. Especially in case of CS_ECH_3, by optimized combination of covalent bonds based on glycidyl groups with physical interaction via amino group on CS monolith, immobilization of enzyme, maintaining relatively high and stable activity was achieved. Furthermore, the integration of physical adsorption and covalent binding facilitated a balance between simplicity and stability of the immobilization process.

3.3.3 Effect of pH and temperature on enzyme activity

The influence of pH on free and immobilized α-amylase activities was investigated in the pH range of 3.5–8.5 at 40 °C (Figure 3-6(a)). The highest free and immobilized enzyme activities were detected at a pH of 6.5. At all pH levels, the activity of immobilized α-amylase on CS_ECH_3 was more than that of its free counterpart. At the pH levels of 4.5, 5.5, 7.5, and 8.5, the activities of the

immobilized enzyme were 65%, 87%, 71%, and 55%, whereas those of the free α-amylase were 57%, 81%, 60%, and 34%, respectively. This may be due to strong interactions between the enzyme and monolith. Various crosslinking interactions were used to fix the enzymes to the support material, thereby stabilizing the enzyme structure and protecting it from pH and temperature variations.[36,37] Upon immobilization, the properties of amylase were altered because of conformational changes due to the binding between the support material and enzyme. Consequently, the immobilization reduced the sensitivity of the enzyme to both acidic and alkaline conditions.[38] Notably, the crosslinking reactions prevented CS_ECH_3 from dissolving at low pH levels. CS_ECH_3 is a reliable support material for immobilizing and improving the stability of α-amylase across diverse pH environments.

Additionally, the free and immobilized α-amylase activities were investigated at various temperatures (30–60 °C) in a thermostatically controlled water bath at a pH of 6.5. As shown in Figure 3-6(b), the free enzyme and immobilized enzyme exhibit optimum activities at the temperatures of 40 °C and 50 °C, respectively. As temperature increases, the free-enzyme activity significantly reduces to 34% at 60 °C. By contrast, the immobilized-enzyme activity reduces to only 80% at 60 °C. Enzyme stability may explain the decrease in activity at high temperatures. Compared with immobilized enzymes, soluble enzymes begin to denature at high temperatures.[39,40] Thermal denaturation reduces the relative activity of the unbound enzyme at high temperatures. However, the activity of the immobilized enzyme decreases more slowly above

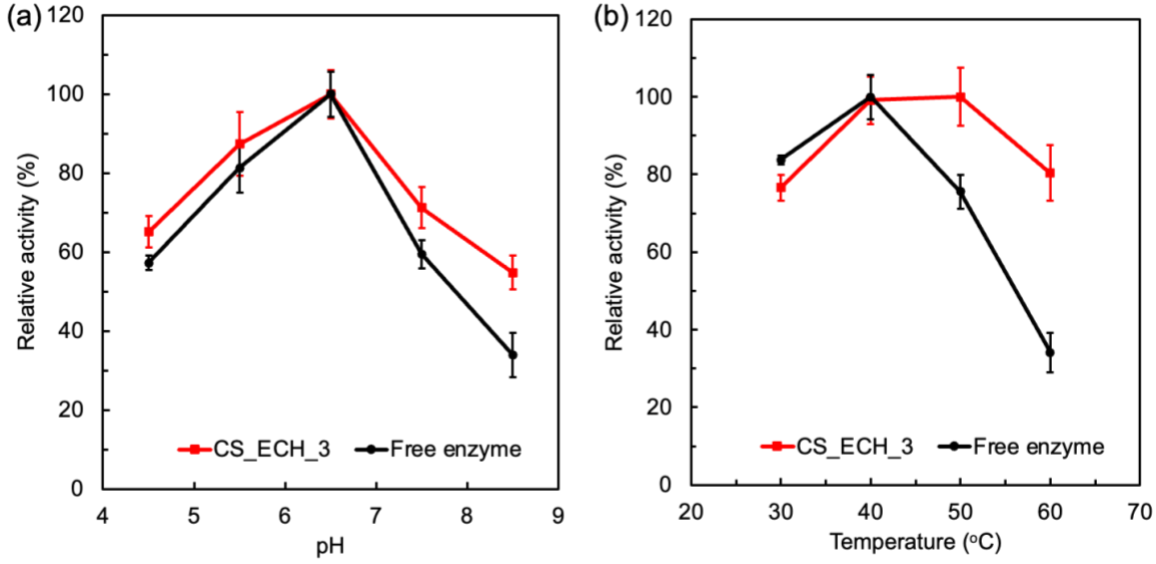

Figure 3-6. Effect of (a) pH and (b) temperature on activity of free and immobilized α-amylase.

50 °C. The formation of several covalent bonds between the enzyme and support reduces conformational flexibility, thermal vibration, and enzyme mobility. Additionally, it prevents the aggregation and unfolding of the enzyme protein.[28] Therefore, compared to the free enzyme, the immobilized enzyme exhibits superior stability over a broader temperature profile. Several studies have reported that enzyme immobilization leads to increased optimal temperatures.[41–43] As immobilized enzymes can withstand high temperatures, they are preferred for industrial applications over their soluble counterparts.[44]

3.3.4 Kinetic parameters

Using a Lineweaver–Burk plot, the rate of the enzymatic reaction can be evaluated with respect to the substrate concentration (Figure 3-7). The apparent K_m values of the immobilized and soluble α-amylase were 4.59 mg/mL and 3.08 mg/mL, respectively, and the V_m values were 1.31 μmol/mL·min and 1.53 μmol/mL·min, respectively. V_m, the maximum reaction velocity, is a measure of the intrinsic characteristics of the enzyme, and K_m is a measure of the affinity of the substrate for the enzyme. Compared to the free enzyme, the immobilized enzyme exhibited a higher K_m, suggesting that it had a lower affinity for the substrates. A possible explanation for this is that immobilization alters the structural characteristics of the enzyme and restricts substrate access to the active sites, leading to decreased affinity.[45,46] This explanation is consistent with the decreased V_m value of the immobilized enzyme. The reduced V_m value can be attributed to the mass-transfer restricting pores in the monolith, which limit starch diffusion towards immobilized α-amylase. Several studies have reported larger K_m and lower V_m for immobilized α-amylase compared to its free form.[47]

In the field of enzyme immobilization, it is imperative to assess the performance of the immobilized enzyme in comparison with its free form. The affinity of the enzyme for its substrate and the maximum reaction rate are key parameters to evaluate. Many studies have reported that upon immobilization, enzymes tend to exhibit reduced substrate affinity (high K_m values) and decreased reaction rates (low V_m values) (Table 3-2). In the case of α-amylase immobilization on the CS monolith, the results indicate a decrease in substrate affinity, consistent with previous findings. However, the reduction in affinity is relatively small at only 1.5 times the decrease in K_m values. This suggests that the CS monolith provides a favorable microenvironment that helps to maintain a relatively high substrate affinity for the enzyme. Interestingly, when considering V_m,

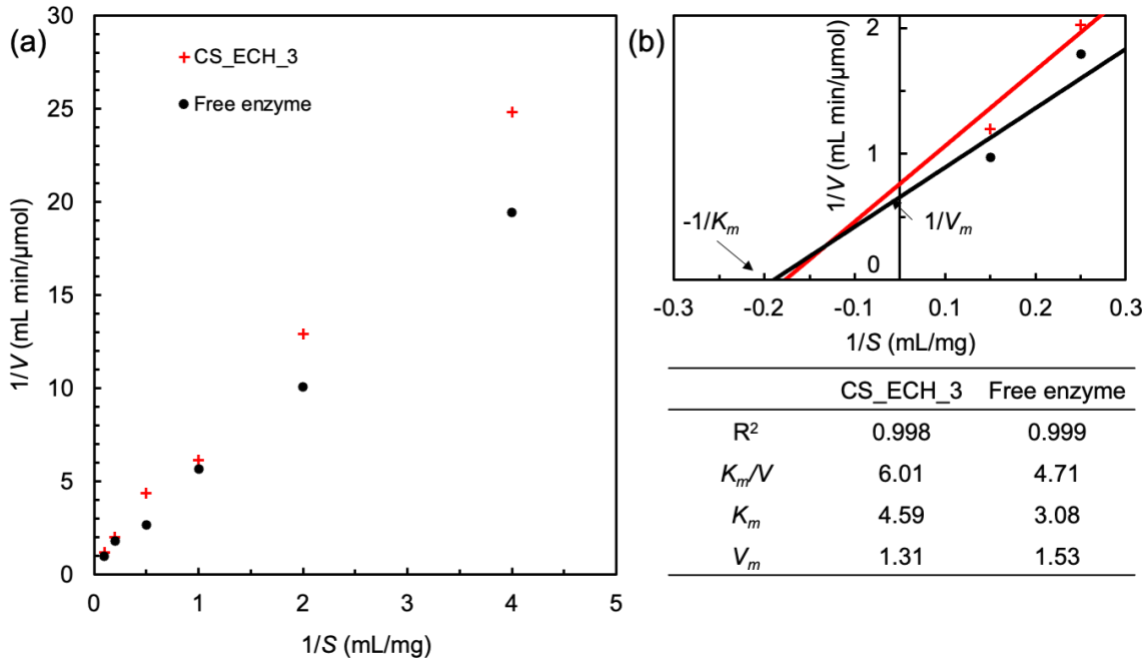

	CS_ECH_3	Free enzyme
R^2	0.998	0.999
K_m/V	6.01	4.71
K_m	4.59	3.08
V_m	1.31	1.53

Figure 3-7. (a) Lineweaver–Burk plot (b) K_m of immobilized and free α-amylase.

the immobilized α-amylase on the CS monolith shows one of the lowest reductions compared to its free form, with just 1.2 times the decrease. This suggests that the CS monolith effectively retains the catalytic activity of the enzyme, allowing it to maintain a high reaction rate even after immobilization. Another notable advantage of the CS monolith is its suitability for use in a flow system. The advantages of flow systems over batch systems in practical industrial processes include continuous operation, saving time and energy, and enabling continuous operation. CS monoliths with immobilized enzymes have demonstrated high activity in flow systems indicating their potential for practical applications in various biotechnological processes.

3.3.5 Storage stability

Storage stability is a crucial parameter that affects enzyme immobilization. Generally, enzymes in solution are unstable during storage, and their activity gradually decreases. To achieve a long shelf life, the effects of storage conditions on immobilized enzymes must be considered. Therefore, the storage stabilities of the immobilized and free enzymes were evaluated over a storage period of 56 d at 4 °C, and their catalytic activities were measured every week. Their relative activity was calculated based on the initial activity. Figure 3-8 shows the storage stabilities of free and immobilized α-amylase. After one month, the free enzyme loses almost all its activity.

Table 3-2. Comparison of K_m and V_m values of immobilized α-amylases.

α-Amylase	Support material	K_m	V_m	Immob. type (system)	Ref.
-	hybrid gel	^{i}2.01 mg/mL ^{f}1.89 mg/mL increased 1.1 times	^{i}0.198 mg/mL·min ^{f}0.329 mg/mL·min decreased 1.7 times	adsorption (batch)	47
from malt	chitosan beads	^{i}1.49 mg/mL ^{f}0.5 mg/mL increased 3 times	^{i}3.44 mg/mL·min ^{f}7.4 mg/mL·min decreased 2.2 times	adsorption (batch)	48
Bacillus subtilis	amidoximated acrylic fabric	^{i}9.6 mg/mL ^{f}3.8 mg/mL increased 2.5 times	^{i}0.281 mg/mL·min ^{f}0.311 mg/mL·min decreased 1.1 times	covalent attachment (batch)	41
Aspergills oryzae	nanocomposite beads	^{i}9.12 mg/mL ^{f}6.8 mg/mL increased 1.3 times	^{i}1.3 mg/mL·min ^{f}0.629 mg/mL·min increased 2.1 times	covalent attachment (batch)	23
Porcine Pancreas	$CaCO_3$	^{i}0.55 mg/mL ^{f}0.45 mg/mL increased 1.2 times	^{i}0.35 mg/mL·min ^{f}10 mg/mL·min decreased 29 times	covalent attachment (batch)	49
Aspergillus oryzae	poly(ethylene terephthalate) fiber	^{i}11.94 mg/mL ^{f}6.61 mg/mL increased 1.8 times	^{i}0.335 U ^{f}0.628 U decreased 1.9 times	covalent attachment (flow)	50
Aspergillus oryzae	alginate matrix	^{i}0.18 mM ^{f}0.15 mM increased 1.2 times	^{i}81.3 mg/mL·min ^{f}357.1 mg/mL·min decreased 4.4 times	enzyme entrapment (flow)	51
Bacillus sp.	CS monolith	^{i}4.59 mg/mL ^{f}3.08 mg/mL increased 1.5 times	^{i}1.31 μmol/mL·min ^{f}1.53 μmol/mL·min decreased 1.2 times	adsorption and covalent attachment (flow)	This study

i: immobilized enzyme

f: free enzyme

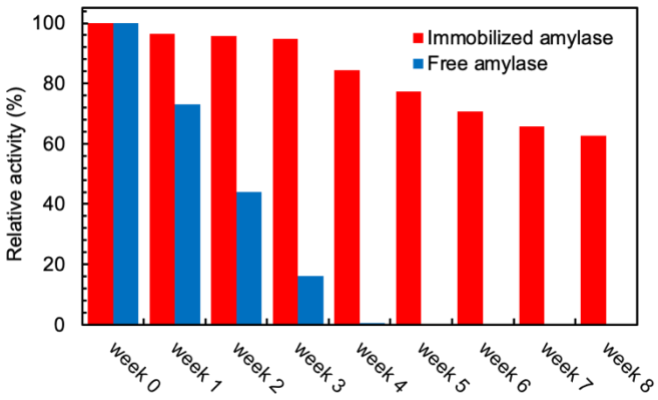

Figure 3-8. Storage stability of immobilized α-amylase on CS_ECH_3 monolith.

By contrast, α-amylase immobilized on the CS_ECH_3 monolith loses only 6% of its original activity after three weeks and retains more than 60% after eight weeks. Compared to the free α-amylase, the immobilized α-amylase appears to be more conformationally stable, owing to the interactions between the enzyme and carrier. Therefore, immobilization significantly prevents enzyme deactivation and enhances enzyme storage stability. Several polymeric supports have been reported to retain 75–90% of α-amylase activity 25 d after immobilization.[48] The experimental results also demonstrated that the CS_ECH_3 monolith could serve as a favorable support for α-amylase.

3.3.6 Reusability of immobilized α-amylase

Although enzymes are expensive, the existing immobilization techniques allow them to be recycled and reused multiple times. Immobilized enzymes must be frequently reused to ensure their cost-effectiveness in industrial applications. The reusability of α-amylase immobilized on CS, CSE_ECH_3, CSE_ECH_5, CSE_ECH_10, and CSE_ECH_20 monoliths was examined across several cycles (Figure 3-9). The average enzyme activity was determined at a pH of 6.5 and temperature of 40 °C. The relative activity of each sample was calculated based on the first cycle. After three cycles, the activities of the enzymes immobilized on the CSE_ECH_3, CSE_ECH_5, CSE_ECH_10, and CSE_ECH_20 monoliths were 61.8%, 70.9%, 72.3%, 87.4%, and 89.6%, respectively. At the end of the seventh cycle, their activities gradually decreased to 11.2%, 32.9%, 32.8%, 47.1%, and 65.6%, respectively. The subsequent decrease in activity after each cycle can be attributed to enzyme desorption. Enzymes that attach to carriers solely through adsorption

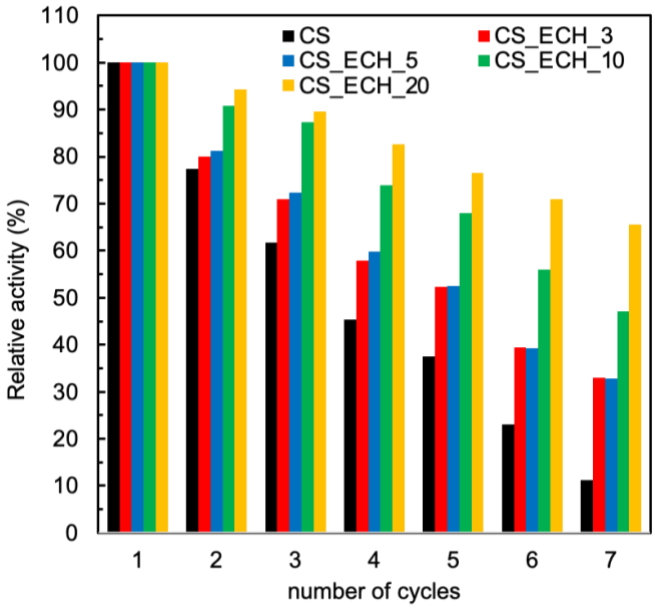

Figure 3-9. Reusability of immobilized α-amylase on CS, CS_ECH_3, CS_ECH_5, CS_ECH_10, and CS_ECH_20.

forces may be removed during a cycle, reducing the number of enzymes remaining on the monoliths. This phenomenon is validated by the behavior of the non-crosslinked and crosslinked monoliths with different ratios. The enzymes immobilized on the CSE_ECH_20 monolith were difficult to remove as most of them were covalently bonded to the monolith. Hence, compared to the other monoliths, CSE_ECH_20 retained higher amount of α-amylase after seven cycles. By contrast, the availability of enzymes on the non-crosslinked CS monolith decreased after each cycle.

The reduced activity with increasing number of cycles may also be due to the gradual inactivation of the immobilized α-amylase. Previous studies have reported a similar decrease in enzyme activity after the second cycle.[47,49,50] Nevertheless, the crosslinked CS monoliths demonstrated their efficiency as α-amylase supports, and they can be used multiple times in flow systems in various applications.

3.3.7 Immobilization of lipase and catalase

CS monolith was also used in preliminary analysis to assess the efficiency in immobilizing enzymes of different types, aiming to evaluate the affinity of the CS monolith with a broader range of enzymes. Figure 3-10(a) shows the amount of immobilized α-amylase, lipase and catalase. The

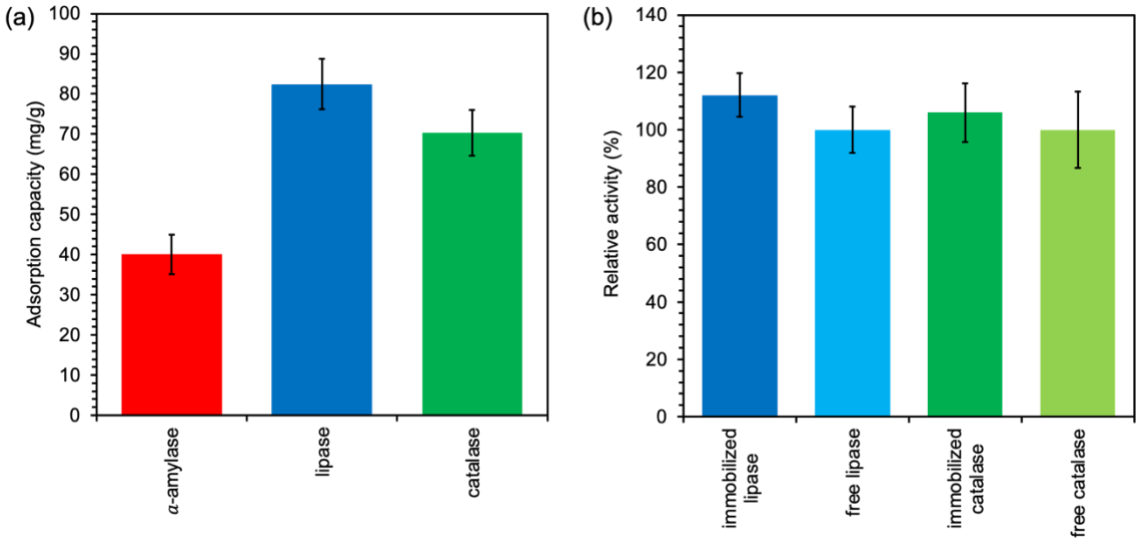

Figure 3-10. (a) Amount of α-amylase, lipase, and catalase immobilized on the CS_ECH_3 monolith and (b) relative activities of free and immobilized lipase and catalase.

loading capacities of the CS_ECH_3 monolith for lipase and catalase were 82.4 mg/g and 70.3 mg/g, respectively, which were higher than that observed for α-amylase (40.1 mg/g). Therefore, it can be concluded that the CS monolith can also immobilize other enzymes.

The activities of immobilized lipase and immobilized catalase were higher than those of their free counterparts (Figure 3-10(b)). The immobilized lipase exhibited an activity of 112%, suggesting that the CS monoliths effectively retained the catalytic activity of the immobilized lipase, leading to higher enzyme activity compared to the free enzymes. Considering the hydrophilic nature of the CS monoliths, there is a possibility that the hydrophobic nature of lipase's substrate might be incompatible with the hydrophilic environment. However, as the study concludes that lipase was successfully immobilized and its activity was higher than that of the free enzyme, it suggests that the CS monoliths were able to provide an environment conducive to the catalytic activity of lipase despite hydrophobic nature of lipase.

Similarly, immobilized catalase demonstrated an activity of 106%, which was higher than that of its free counterpart. This indicated that the immobilization of catalase also increased its activity. The immobilization may have facilitated a more favorable microenvironment for catalase, leading to improved catalytic properties.

Factors such as enzyme structure, substrate specificity, and the immobilization technique employed can influence the interaction between enzymes and the CS matrix. Hydrophilic enzymes

like α-amylase and catalase have shown successful immobilization on the CS monolith, while lipase, a hydrophobic enzyme, may present challenges. However, preliminary experiments have demonstrated that CS can still immobilize lipase effectively. By discussing the classification of enzymes and presenting the results of immobilized lipase and catalase on the CS monolith, it becomes evident that while some enzymes may pose challenges due to their properties, the CS monolith offers a promising platform for effective enzyme immobilization across a range of enzyme types.

3.4 Conclusions

This study presents a practical method for immobilizing α-amylase on a hierarchically porous CS monolith fabricated using chemically modified CT and thermally induced phase separation. The SEM images and N_2 adsorption-desorption isotherms revealed the specific pore sizes of the CS100 monolith, provided an optimal structure for enzyme immobilization. As part of this immobilization technique, two bindings are utilized, amino groups in CS assisting in physical adsorption, and epoxy groups in ECH enhancing covalent bonding. Compared to the soluble form, α-amylase immobilized on the CS monolith exhibited excellent stability across various pH levels and temperatures. Moreover, the CS monolith effectively retained a relatively high substrate affinity (1.5 times decrease in K_m values) and maintained a high reaction rate (1.2 times decrease in V_m values) compared to other reported immobilization techniques. The immobilized α-amylase on the CS_ECH_3 monolith demonstrated impressive storage stability, retaining over 60% of its activity after eight weeks of storage at 4 °C, and reusability, further emphasizing its practicality. Furthermore, the CS monolith showcased potential for immobilizing other enzymes, namely lipase and catalase. The immobilized lipase and catalase exhibited higher loading capacities and enhanced activity than their soluble counterparts. Overall, this study provides guidelines for leveraging the hierarchical porous structure of CS monoliths for immobilizing enzymes, which can lead to efficient enzyme utilization in flow systems and potentially enhance the cost-effectiveness of enzymes in industrial applications.

References

[1] S. Jemli, D. Ayadi-Zouari, H. Ben Hlima, S. Bejar, *Crit. Rev. Biotechnol.* **2016**, *36*, 246.

[2] R. DiCosimo, J. McAuliffe, A. J. Poulose, G. Bohlmann, *Chem. Soc. Rev.* **2013**, *42*, 6437.

[3] J. Chapman, A. E. Ismail, C. Z. Dinu, *Catalysts* **2018**, *8*.

[4] V. K. Shinde, K. R. Vamkudoth, *J. Food. Sci. Technol.* **2022**, *59*, 3733.

[5] M. Bláhová, V. Štefuca, H. Hronská, M. Rosenberg, *Molecules* **2023**, *28*, 3281.

[6] B. Zhang, S. Dhital, M. J. Gidley, *Biomacromolecules* **2013**, *14*, 1945.

[7] M. A. Farooq, S. Ali, A. Hassan, H. M. Tahir, S. Mumtaz, S. Mumtaz, *Arch. Microbiol.* **2021**, *203*, 1281.

[8] A. Taheri-Kafrani, S. Kharazmi, M. Nasrollahzadeh, A. Soozanipour, F. Ejeian, P. Etedali, H. A. Mansouri-Tehrani, A. Razmjou, S. M. G. Yek, R. S. Varma, *Crit. Rev. Food Sci. Nutr.* **2021**, *61*, 3160.

[9] J. M. Choi, S. S. Han, H. S. Kim, *Biotechnol. Adv.* **2015**, *33*, 1443.

[10] A. Madhu, J. N. Chakraborty, *J. Clean Prod.* **2017**, *145*, 114.

[11] O. Barbosa, R. Torres, C. Ortiz, Á. Berenguer-Murcia, R. C. Rodrigues, R. Fernandez-Lafuente, *Biomacromolecules* **2013**, *14*, 2433.

[12] Y. Wan, J. Zhou, J. Ni, Y. Cai, M. Cohen Stuart, J. Wang, *Biomacromolecules* **2024**.

[13] M. P. Cabrera, T. F. da Fonseca, R. V. B. de Souza, C. R. D. de Assis, J. Quispe Marcatoma, J. da Costa Maciel, D. F. M. Neri, F. Soria, L. B. de Carvalho, *Appl. Surf. Sci.* **2018**, *457*, 21.

[14] T. Jesionowski, J. Zdarta, B. Krajewska, *Adsorption* **2014**, *20*, 801.

[15] P. Zucca, E. Sanjust, *Molecules* **2014**, *19*, 14139.

[16] S. Smith, K. Goodge, M. Delaney, A. Struzyk, N. Tansey, M. Frey, *Nanomaterials* **2020**, *10*, 1.

[17] K. Gawlitza, C. Wu, R. Georgieva, D. Wang, M. B. Ansorge-Schumacher, R. von Klitzing, *Phys. Chem. Chem. Phys.* **2012**, *14*, 9594.

[18] M. Mathesh, B. Luan, T. O. Akanbi, J. K. Weber, J. Liu, C. J. Barrow, R. Zhou, W. Yang, *ACS Catal.* **2016**, *6*, 4760.

[19] K. Cheng, F. Svec, Y. Lv, T. Tan, *Small* **2019**, *15*, 1902927.

[20] M. Bilal, Y. Zhao, T. Rasheed, H. M. N. Iqbal, *Int. J. Biol. Macromol.* **2018**, *120*, 2530.

[21] J. Zdarta, A. S. Meyer, T. Jesionowski, M. Pinelo, *Catalysts* **2018**, *8*, 92.

[22] S. (Gabriel) Kou, L. M. Peters, M. R. Mucalo, *Int. J. Biol. Macromol.* **2021**, *169*, 85.

[23] T. Mardani, M. S. Khiabani, R. R. Mokarram, H. Hamishehkar, *Int. J. Biol. Macromol.* **2018**, *120*, 354.

[24] A. Dinçer, S. Becerik, T. Aydemir, *Int. J. Biol. Macromol.* **2012**, *50*, 815.

[25] Y. Xin, Q. Xiong, Q. Bai, M. Miyamoto, C. Li, Y. Shen, H. Uyama, *Carbohydr. Polym.* **2017**, *157*, 429.

[26] L. Sundberg, J. Porath, *J. Chromatogr. A* **1974**, *90*, 87.

[27] R. Bardestani, G. S. Patience, S. Kaliaguine, *Can. J. Chem. Eng.* **2019**, *97*, 2781– 2791.

[28] F. Gashtasbi, G. Ahmadian, K. A. Noghabi, *Enzyme Microb. Technol.* **2014**, *64–65*, 17.

[29] Z. Sun, H. Su, Y. Zhong, H. Xu, B. Wang, L. Zhang, X. Sui, X. Feng, Z. Mao, *Polym. Adv. Technol.* **2022**, *33*, 546.

[30] Z. Chen, L. Liu, X. Wu, R. Yang, *RSC Adv.* **2016**, *6*, 108583.

[31] K. F. Schilke, C. Kelly, *Biotechnol. Bioeng.* **2008**, *101*, 9.

[32] J. Kaushal, Seema, G. Singh, S. K. Arya, *Biotechnol. Rep.* **2018**, *18*.

[33] M. Suzuki, Y. Matsumoto, T. Sekikawa, K. Iwahori, *Jpn. J. Wat. Treat. Biol.* **2008**, *44*, 161.

[34] H. Zheng, Y. M. Du, J. H. Yu, L. Xiao, *Chem. J. Chinese U.* **2000**, *21*, 809.

[35] W. S. Wan Ngah, M. A. K. M. Hanafiah, S. S. Yong, *Colloids Surf. B. Biointerfaces* **2008**, *65*, 18.

[36] A. I. Kallenberg, F. van Rantwijk, R. A. Sheldon, *Adv. Synth. Catal.* **2005**, *347*, 905.

[37] N. Gupta, E. Beliya, J. S. Paul, S. K. Jadhav, *Coord. Chem. Rev.* **2022**, *464*, 214557.

[38] S. P. O'Neill, P. Dunnill, M. D. Lilly, *Biotechnol. Bioeng.* **1971**, *13*, 337.

[39] E. Querol, J. A. Perez-Pons, A. Mozo-Villarias, *Protein Eng., Des. Sel.* **1996**, *9*, 265.

[40] I. Victorino da Silva Amatto, N. Gonsales da Rosa-Garzon, F. Antônio de Oliveira Simões, F. Santiago, N. Pereira da Silva Leite, J. Raspante Martins, H. Cabral, *Biotechnol. Appl. Biochem.* **2022**, *69*, 389.

[41] T. Noda, S. Furuta, I. Suda, *Carbohydr. Polym.* **2001**, *44*, 189.

[42] Y. Q. Almulaiky, F. M. Aqlan, M. Aldhahri, M. Baeshen, T. J. Khan, K. A. Khan, M. Afifi, A. Al-Farga, M. K. Warsi, M. Alkhaled, A. A. M. Alayafi, *R. Soc. Open Sci.* **2018**, *5*, 172164.

[43] A. R. Al-Najada, Y. Q. Almulaiky, M. Aldhahri, R. M. El-Shishtawy, S. A. Mohamed, M. Baeshen, A. Al-Farga, W. H. Abdulaal, S. A. Al-Harbi, *Sci. Rep.* **2019**, *9*, 12672.

[44] Y. R. Maghraby, R. M. El-Shabasy, A. H. Ibrahim, H. M. E.-S. Azzazy, *ACS Omega* **2023**, *8*, 5184.

[45] G. Bayramoğlu, A. Denizli, M. Y. Arıca, *Polym. Int.* **2002**, *51*, 966.

[46] B. Akkaya, A. F. Yenidunya, R. Akkaya, *Int. J. Biol. Macromol.* **2012**, *50*, 991.

[47] E. A. Nazarova, E. D. Yushkova, A. I. Ivanets, V. G. Prozorovich, P. V Krivoshapkin, E. F. Krivoshapkina, *Starch - Stärke* **2022**, *74*, 2100017.

[48] M. V. Kahraman, N. Kayaman-Apohan, A. Ogan, A. Güngör, *J. Appl. Polym. Sci.* **2006**, *100*, 4757.

[49] R. J. Shukla, S. P. Singh, *Int. J. Biol. Macromol.* **2016**, *85*, 208.

[50] M. V. Kahraman, G. Bayramoğlu, N. Kayaman-Apohan, A. Güngör, *Food Chem.* **2007**, *104*, 1385.

Concluding remarks

In conclusion, the successful fabrication of tunable hierarchically porous CT and CS monoliths using the TIPS method represents a significant advancement in the field of porous materials. The ability to control the pore morphology by adjusting the phase separation conditions is a crucial capability, as it allows the tailoring of the monoliths' properties to suit specific applications. The monoliths, as well as hydroxy groups, also contain acetylamide and amino bonds, which broadens their direct applications and provides many possibilities for modification with other functional groups.

In chapter 1, a continuous porous CT monolith was fabricated for the first time using the TIPS method. Initially, DBC, a CT derivative, was synthesized and used as the starting polymer to fabricate the monolith. By manipulating parameters such as the DBC concentration and the DMSO/H_2O ratio, the pore morphology of the monoliths could be controlled. The DBC monolith was then converted to a CT monolith through an alkaline hydrolysis of the butyryl ester. Along with the hierarchical porous structure, the DBC and CT monoliths exhibited excellent mechanical properties and thermal stability, and water flow tests demonstrated sufficient permeability for use as a filter or microreactor.

In chapter 2, a new, practical, and template-free approach was developed to prepare highly effective, stable, and reusable hierarchically porous CS monoliths by deacetylation of CT monoliths. Prior to the deacetylation process, CT monoliths were crosslinked by ECH with varied ratios, and the deacetylation of the CT monoliths to CS monoliths was achieved through a high-concentration alkali treatment at high temperature. The crosslinking by ECH was found to increase the durability of the CS monoliths against acidic and basic environments. The acquired CS monoliths exhibited a high surface area, and in adsorption experiments, they demonstrated excellent performance in a continuous flow system due to their hierarchical porous morphology. The monoliths were able to efficiently remove metal ions from aqueous solutions, and the crosslinked CS monoliths exhibited good reusability in multiple adsorption-desorption cycles.

Chapter 3 introduced a novel and practical method for immobilizing the enzyme α-amylase on a hierarchically porous CS monolith. By controlling the morphology of the CS monolith, the specific pore sizes were optimized to provide an ideal structure for effective enzyme immobilization. The immobilization technique utilized two types of binding mechanisms. Firstly, the amino groups present in the CS assisted in the physical adsorption of the enzyme. Secondly,

the epoxy groups introduced through the use of ECH facilitated enhanced covalent bonding between the CS and the enzyme. The α-amylase immobilized on the CS monolith demonstrated excellent stability, reusability, and increased activity compared to the soluble enzyme, across a range of pH levels and temperatures. The high porosity and permeability of the CS monolith enabled the preservation of a high reaction rate and good affinity with substrate for the immobilized enzymes. The optimal preparation conditions for the immobilization process were determined based on parameters such as immobilization efficiency, enzymatic activity, storage stability, and reusability. To further validate the versatility of this method, CS monoliths were also tested with other enzymes, such as lipase and catalase, and their performance was evaluated.

Overall, the findings from this research have far-reaching implications. The ability to fabricate tunable porous monoliths with desirable properties, along with the development of efficient enzyme immobilization techniques, can contribute to the advancement of various industries, including water treatment, biomedicine, and biotechnology. The practical guidelines provided can aid in the design and development of cost-effective, high-performance systems for real-world applications.

List of publications

1. Fabrication of Chitin Monoliths with Controllable Morphology by Thermally Induced Phase Separation of Chemically Modified Chitin

   Emil Hajili, Zhicheng Suo, Akihide Sugawara, Taka-Aki Asoh, Hiroshi Uyama

   Carbohydrate Polymers, **2022**, *275*, 118680.

   DOI: 10.1016/j.carbpol.2021.118680

2. Fabrication of 3D Hierarchically Porous Chitosan Monoliths by Thermally Induced Phase Separation of Chemically Modified Chitin

   Emil Hajili, Akihide Sugawara, Taka-Aki Asoh, Hiroshi Uyama

   ACS Sustainable Chemistry & Engineering, **2023**, *11 (14)*, 5473−5484.

   DOI: 10.1021/acssuschemeng.2c06953

3. Application of Hierarchically Porous Chitosan Monolith for Enzyme Immobilization

   Emil Hajili, Akihide Sugawara, Hiroshi Uyama

   Biomacromolecules, **2024**, *25 (6)*, 3486–3498.

   DOI: 10.1021/acs.biomac.4c00109

Acknowledgement

The completion of this doctoral thesis would not have been possible without the support and guidance of numerous individuals. I would like to express my deepest gratitude to all those who have contributed to this journey.

First and foremost, I would like to sincerely thank my supervisor, Professor Hiroshi Uyama, for their unwavering mentorship, valuable insights, and steadfast support throughout my doctoral studies. Your expertise, encouragement, and belief in my abilities have been instrumental in shaping this research. I am truly grateful for the opportunity to work under your supervision.

I would like to convey my gratefulness to Professor Taka-Aki Asoh of Osaka University, who appointed as my advisor during my first early research projects and gave me the skills. I would also like to extend my appreciation to Professor Akihide Sugawara for their insightful comments, constructive feedback, and collaborative efforts during the various stages of this project. Your involvement and willingness to share your knowledge have been invaluable. Particularly, I would like to thank Professor Yu-I Hsu for her encouragement and suggestions whenever encountering impediments.

I am grateful to Professor Hidehiro Sakurai and Professor Shinya Furukawa who have taken the time to review this thesis and provide their valuable assessments. Your thoughtful evaluations have helped to strengthen the quality and rigor of this work.

I would like to extend my gratitude to everyone who has worked at Uyama Laboratory, both former and current: Ms.Yoko Uenishi, and Ms.Tomoko Shimizu, Ms. Kyoko Tanimura, Ms. Erina Katsuragawa, Ms. Chikako Abe, Ms. Rieko Yagi, Ms. Yasuko Matsuda, and Ms Kyoko Fuma

I would like to express my utmost gratitude to Dr. Naharullah Bin Jamaluddin, Dr. Yankun Jia, Dr. Raghav Soni, Dr. Hanyu Wen, Dr. Yanting Lyu, Dr. Yan Wang, Dr. Luwei Zhang, Dr. Meng Wei, Dr. Mark Adam Malaluan Ferry, Dr. Yuxiang Jia, Dr. Nontarin Roopsung, Mr. Toshiki Honda, Mr. Yuya Fujiwara, Mr. Ginga Hoshi, Mr. Tatsuya Yamamoto, Ms. Anna Shigaki, Ms. Madhurangika Panchabashini Horathal Pedige, Ms. Manjie He, Mr. Yu Cao, Mr. Peng Du, Ms. Juan Wang, Mr. Kazuki Shibasaki, Mr. Atsuki Takagi, Ms. May Myat Noe, Ms. Hasinah Binti Mohamed Rafiq, Ms. Judit Rebeka Molnár, Ms. Guan Wang, Ms. Ying Yao, Mr. Ruiqi Zhang, Mr. Yihan Gao, Mr. Kohei Kikkawa, Ms. Airi Ozaki, Ms. Jiaxin Alice Chen, Ms. Zeying Cao, Ms.

Linxuan Li, Ms. Yuka Kashihara, Ms. Shiho Takai, Mr. Yuji Kiba, Mr. Takeshi Hiraoka, Mr. Yuki Shioji, Mr. Atsushi Koizumi, Mr. Motoi Oda, Mr. Kaita Kikuchi, Mr. Koki Tsujita, Mr. Hajime Fujimori, Ms. Suzune Miki, Ms. Thuy Le Huynh An, Ms. Izzah Durrati Binti Haji Abdul, Ms. Sooyeon Noh, Mr. Xinyu Lou, Mr. Hiroshi Hasegawa, Mr. Shotaro Yano, Mr. Kippei Yamamura, Ms. Rika Onishi, Ms. Hajah Wafiqah Binti Haji Daim, Ms. Ziyu Meng Ms. Shafinee Yarnina Hj Md Shafri, Mr. Alejandro Adrian Ayala Escamilla, Ms. Daniela Yacine Sebastião Bravo Da Costa, Mr. Jiahui Dong, Ms. Yuka Asai, Mr. Yinxiang Shen, Ms. Moe Kominami, Ms. Akane Odagaki, Ms. Rina Kugimiya, Mr. Shunya Kubo, Mr. Sota Nakagawa, Ms. Maoko Hayashi, Mr. Shunsuke Kondo, Mr. Yudai Ioku, Mr. Naoaki Ishihara, Mr. Yuta Okuda, Ms. Kanoko Sakai, Mr. Takehiro Masuda, and all members who worked in the Uyama laboratory between 2019 and 2024 for hearty supports and kind assistances in research and daily life.

This research would not have been possible without the financial support of the Ministry of Education, Culture, Sports, Science and Technology (MEXT) of Japan. I am deeply appreciative of the scholarship and the opportunities it has provided me.

Most importantly, I would like to dedicate this research to my family, Elshad Hajiyev, Antiga Hajiyeva, Elmar Hajiyev, and Farah Hajiyeva, as well as my partner Fariza Vahabova. Your belief in me and your willingness to understand the demands of doctoral research have been a constant source of strength. I am truly grateful to all those who have contributed to the successful completion of this doctoral thesis. This accomplishment would not have been possible without the collective efforts and support of this remarkable network of individuals.